University of Nevada, Reno

Mesoscale Adjustments within the Planetary Boundary Layer in Tropical and Extratropical Environments

A dissertation submitted in partial fulfillment of the requirements for the degree of Doctor of Philosophy in Atmospheric Science

by

Matthew G. Fearon

Dr. Timothy J. Brown/Dissertation Advisor

December, 2015

THE GRADUATE SCHOOL

We recommend that the dissertation
prepared under our supervision by

MATTHEW G. FEARON

Entitled

Mesoscale Adjustments Within The Planetary Boundary Layer In Tropical And Extratropical Environments

be accepted in partial fulfillment of the
requirements for the degree of

DOCTOR OF PHILOSOPHY

Dr. Timothy J. Brown, Advisor

Dr. Michael L. Kaplan, Committee Member

Dr. John M. Lewis, Committee Member

Dr. John F. Mejia, Committee Member

Dr. Thomas J. Nickles, Graduate School Representative

David W. Zeh, Ph. D., Dean, Graduate School

December, 2015

Abstract

A series of three papers comprised the research completed for this dissertation study. Each contribution examined mesoscale processes that occurred within the planetary boundary layer in the context of the chosen avenue of research. The premise of paper one centered on the daytime growth of the convective mixed layer over the continental mid-latitudes for the application of smoke management from wildland fire. An evaluation of the most robust practical technique for mixed-layer height estimation was performed using numerical model simulations and space-based lidar retrievals. Results revealed that daytime mixed-layer growth corresponded with the excitation of the turbulent kinetic energy (TKE) and layer height was best determined where the dissipation of TKE occurred in the vertical. Papers two and three were completed as a two-part series where emphasis was placed on the boundary layer dynamics associated with the precursor environment wherein Hurricane Sandy (October 2012) developed. And although greater attention was paid to the localized mesoscale dynamics, evaluation of the larger-scale influence was also examined across the entire northern hemisphere weeks in advance. Results from two mesoscale model simulations, a control run and no-terrain experiment, show that the precursor environment is highly influential to its developmental fate. In the case of Sandy, the surrounding orography imposed constraints on the environmental mass field such that a low-level curved momentum channel was produced upstream of the incipient disturbance (on its southwestern side) wherein vorticity generation was maximized and wrapped into the vortex inflow region. The latter westerly momentum also converged with a secondary low-level southerly jet feature that emanated into the vortex inflow region. Model results were evaluated against a suite of satellite data including composite brightness imagery, scatterometer surface wind data, space-

based lidar retrievals, and Best Track data (on storm track, mean sea level pressure, and maximum tangential wind speed) from the National Hurricane Center database.

Acknowledgements

I would like to extend my sincere thanks and appreciation to my research committee inclusive of Drs. Timothy J. Brown, Michael L. Kaplan, John M. Lewis, John F. Mejia, and Thomas J. Nickles. Each member supported, pushed, and encouraged me in a unique way that allowed me to succeed. I am especially grateful to Dr. Michael L. Kaplan for his assistance with this research. Without his guidance, this research endeavor would not have been possible for me. I will never forget his tireless support. In my opinion, Mike's commitment and dedication to teaching meteorology is unmatched by his peers. I am also forever grateful to my wife, Erin, whom put her dreams and career on hold while I pursued mine. She put forth the ultimate sacrifice for which I will forever be indebted. I dedicate this monumental effort to her and our pup, Roscoe (aka, The Brindle), whom is our mutual savior and best friend.

Introduction

This body of work is comprised of three research papers to be submitted for peer-review publication. The underlying emphasis of each contribution centers on the atmospheric dynamics associated with the planetary boundary layer (PBL). PBL dynamics are evaluated in both tropical and extratropical environments.

The convective planetary boundary over land across the continental United States is the primary focus in paper one. Different techniques for the determination of maximum afternoon PBL height are compared and contrasted using model-derived soundings. Model computed height values from each technique are also compared against space-based lidar height estimates. Static and dynamic stability concepts associated with parcel theory along with the vertical variation of turbulent kinetic energy represent the underlying diagnostic principles associated with each technique. Strengths and weaknesses associated with each PBL height method are discussed. The most robust approach for PBL height estimation constitutes the take away result.

The tropical boundary layer becomes the primary focus in papers two and three. These two contributions represent a two-part study on the precursor environment associated with Hurricane Sandy (October 2012). Paper two evaluates the hemispheric mass field variability (via 500 hPa geopotential height anomalies) and the influential large-scale height perturbations imposed on the precursor environment wherein the incipient pre-Sandy wave develops. The daily periodicity of the Arctic, North-Atlantic, and Madden-Julian Oscillations is examined in relation to the vigorous meridional exchange observed over the entire Northern Hemisphere before and after the formation of the incipient wave. The role of a predecessor hurricane in relation to the

deformation and wind shear environment where through the pre-Sandy wave travels is also evaluated.

Paper three examines the downscale consequences of the large-scale mass adjustments discussed in paper two. The evolution of the mesoscale precursor environment over the southwestern Caribbean zone where into the incipient wave migrates and undergoes rapid intensification is the primary focus of the study. Results from two mesoscale model simulations, a control run and no-terrain experiment, are evaluated to assess potential role and sensitivity of the surrounding orography on storm development. As part of the analysis, certain mesoscale features are examined that include a nocturnal jet structure, mountain-plains solenoid circulation patterns, and mesoscale jet structures initiated on the west and south side of the developing disturbance. These features, along with the unique (concentric) geometry of the surrounding landmass/terrain, are studied in detail in the context of storm development. Model results are also evaluated against a suite of satellite data including composite brightness imagery, scatterometer surface wind data, space-based lidar retrievals, and Best Track data (on storm track, mean sea level pressure, and maximum tangential wind speed) from the National Hurricane Center database.

The three papers described above are presented sequentially below (in journal submission format). A concise summary and concluding remarks section follows paper three.

Paper one

Establishing a National Standard Methodology for Operational Mixing Height Determination

MATTHEW G. FEARON
Desert Research Institute, 2215 Raggio Parkway, Reno, NV, 89512

TIMOTHY J. BROWN
Desert Research Institute, 2215 Raggio Parkway, Reno, NV, 89512

GARY M. CURCIO
IPA Fire Environment Specialist, LLC, La Grange, NC, 28551

(Manuscript received 9 April 2015; review completed Day Month Year)

ABSTRACT

Since the 1960s, the Holzworth method has remained a primary tool for operational mixed layer height determination. The air volume through which ground-based pollutants disperse vertically defines mixed layer. The appeal of the method rests on the simple mechanics of making a forecast where knowledge of the surface air temperature in concert with the background vertical structure is sufficient. The National Weather Service routinely issues forecasts using this method for air quality and wildland fire activities.

Methods of this type that are principally based on the static stability structure of the atmosphere and exclude vapor content or dynamical processes (e.g., advection and wind shear) can misrepresent the mixing height calculation. Systematic error such as the height being too low or high can complicate wildland fire activities such as go/no-go burn decisions. Motivation for the present study emerges from this premise and examines mixing height computed from four methodologies.

Mixing height methods employed in this study include Holzworth, Stull, bulk Richardson number, and turbulent kinetic energy, where the latter two include dynamical processes. Mixing height was also derived from satellite-based lidar to provide an observed proxy and validation. Results from a method intercomparison show that turbulent kinetic energy is the most robust and well suited as a national standard methodology for operational use, with both thermodynamic and dynamic processes incorporated. Bulk Richardson number and the Stull method are other possibilities, as calculations are not model dependent and heights were consistent with those from turbulent kinetic energy.

1. Introduction

Smoke from wildfire and prescribed burning in the United States is important in terms of human health as well as environmental and transportation safety (Moeltner et al. 2013). Local

dispersion is a major concern for many wildland fire and air quality agencies that participate in wildfire and prescribed fire activities (e.g., U.S. and State Forest Services, Bureau of Land Management (BLM), and National Weather Service Forecast Offices (NWSFOs), and state and local air quality agencies). Prediction of smoke dispersion indices including mixing height[1], transport wind speed, and ventilation index is a part of operational fire weather forecasts issued by NWSFOs. For the past several years, the user community (e.g., local and state land managers, foresters, and personnel from the aforementioned agencies) has expressed concern over the accuracy of methodologies used to compute mixing height across NWSFOs (personal communication, National Wildfire Coordinating Group discussions 2012-2015), in particular the widely used Holzworth method (Holzworth 1964; 1967). Local or regional discrepancies in the mixing height calculation also arise when the Holzworth method is used in a nonstandard fashion across NWSFOs. Inconsistency in the method complicates wildland fire go/no-go burn decisions and jeopardizes wildfire impact assessments. The current study revisits the Holzworth technique and three documented alternatives for mixing height determination, namely the Stull method; Richardson number; and Turbulent Kinetic Energy, in order to determine which method is the most robust and appropriate as a national standard.

Seibert et al. (2000) define the mixing height as an upper boundary or lid in the atmosphere to which ground-level pollutants vertically disperse. The development of the mixed layer is a function of turbulence that can arise from solar-induced thermal gradients (the convection process), and or mechanical stirring from wind shear or advection. NWSFOs issue routine fire

[1] Mixing height and mixed layer height are synonymous terms in this paper. Mixing depth and mixed layer depth are also synonymous and define the air volume between the ground and the mixing height.

weather forecasts that include mixing height based primarily on the Holzworth method (see Table 1). This procedure follows the adiabatic principle of parcel theory and static stability where mixed layer height is traced to the altitude and intersection of the hypothetical surface parcel with its environment, as shown in Fig. 1 with the potential temperature[2] (θ) profile.

The Holzworth technique provides a quick and reasonable estimate of mixing height from temperature profile data (soundings and or model-derived soundings). However, the use of potential temperature (a dry atmosphere assumption) leads to consistent height underestimation (as shown later in section 4). The neglect of moisture, regardless of the environment (e.g., high desert, moist continental, or coastal), misrepresents the density of the surface parcel and yields a lower mixing height estimate (Fearon 2000). Figure 2 is a graphical depiction of a dry versus moist (unsaturated) atmosphere and includes the use of the virtual potential temperature[3] (θ_v). Examining the static stability of the atmosphere with the virtual potential temperature follows the mixing height methodology described by Stull (1991).

For this study, mixing height values were computed from the two most commonly used operational methods, namely Holzworth and Stull[4]. Heights from bulk Richardson number (RI) and the vertical decline of Turbulent Kinetic Energy (TKE) were also computed and compared. RI is the ratio of the buoyancy to wind shear and TKE is a combined representation of buoyancy, wind shear, advection, and other gradients and perturbation terms that quantify the kinetic energy

[2] The potential temperature is inclusive of dry air only. Synonymous with the term dry potential temperature.
[3] The virtual potential temperature is calculated same as the dry potential temperature except *T* is replaced by virtual temperature (T_v), the temperature that dry air would have if its pressure and density were equal to those of a given sample of moist (unsaturated) air (American Meteorological Society 2015).

[4] Operational use of Stull over Holzworth by some agencies in moist environments is not uncommon (personal communication, National Wildfire Coordinating Group discussions 2012-2015).

through the atmospheric column. RI and TKE each provide a combined measure of the static and dynamic stability whereas Holzworth and Stull provide an estimate of the static stability only. RI and TKE are well documented in the literature (e.g., Vogelezang and Holtslag 1996; Seibert et al. 1997; Zilitinkevich and Baklanov 2002; Jeričević and Grisogono 2006; Lee et al. 2008; Kiefer et al. 2015). Use of TKE for mixing height determination is less common since computation requires finely resolved, evenly spaced data (vertically and horizontally), such as from a numerical model. Mixing height values from these four methods (Holzworth, Stull, RI, and TKE) were also compared to those derived from satellite-based lidar where the latter were chosen to represent observed data and provide an independent measure. The spatial and temporal resolution of the lidar data provided a large coincident sample size against model grid points (discussed in section 3).

The following section of this paper begins with a brief background into the origin of air pollution control in the U.S. and related research, including mention of the classic mixed layer model and boundary layer concepts used in this study. The next section describes the relevant data, the four mixing height methodologies of interest: Holzworth, Stull, RI, and TKE, and the data analysis methods used. Section four provides a discussion of results from a mixing height method intercomparison. Examples of the vertical structure and spatial extent associated with height value discrepancies are also presented. Section five is reserved for a summary of results and recommendations from the authors on the most robust approach for mixing height determination.

2. Background

The origin of comprehensive air pollution control in the United States can be traced back to the mid 20th century. The National Air Pollution Act of 1955 and the Clean Air Act of 1963 (and its subsequent amendments in 1970; U.S. EPA 2015) represent two such pieces of regulatory legislation. Both were enacted in response to human health concerns and the widespread increase of airborne contaminants from industrialization and mobile sources. Air pollution research was one of the primary objectives outlined in this legislation, in particular, investigation of urban emissions, dispersion, and transport in the context of human health impacts. One of the central research themes to emerge during the 1960s was the concept of monitoring (and predicting) the rate of atmospheric dispersion and transport of airborne contaminants.

During the mid-late 20th century numerous studies were performed on atmospheric dispersion in the low-level atmosphere, or the volume of air designated as the mixed layer, (e.g., Pasquill 1961; Holzworth 1964; Turner 1964; Tennekes 1973; Yamada and Berman 1979; Stull 1991). Ball (1960) was arguably the first to tackle the subject in the context of Archimedes Principle, where the density differential between the hypothetical surface parcel and its surrounding environment increases when solar heating is introduced at the air/ground interface. In such circumstances, the static stability stratification of the air column changes with unstable air developing at the lower boundary and facilitating upward acceleration. As the heated air mixes upward, eventually the density differential in the air column becomes zero and the upward acceleration vanishes. Yet, the momentum gained on the upward journey carries air into the adjoining layer and simultaneously promotes downward motion (or entrainment) of upper-level

air. The turbulent motion associated with the buoyancy and entrainment leads to a stratified state where the temperature decrease with height follows the adiabatic rate. Other atmospheric constituents (e.g., wind, water vapor, and pollution) that take part in the turbulent motion become uniform in this mixed layer. This process becomes increasingly complex in the presence of overlying clouds such as non-precipitating cumuliform (as discussed in Lilly 1968 and Betts 1973).

Prognostic models of mixed layer development serve as another common method of height estimation. Figure 3 illustrates the main sub layers of the mixed layer model at the time of maximum heating. These include the shallow surface layer near the ground, the deep turbulent (free convection) layer, and the entrainment zone atop demarking the separation between the boundary layer and the free atmosphere. This depiction is representative of the mixed layer (or jump) model described by Tennekes (1973); Tennekes and Driedonks (1981); Lewis (2007); and others, where the important changes in the potential temperature are a function of the variation in the buoyancy flux ($\overline{w'\theta'}$) at the top and bottom boundaries via the sharp increase and decrease, respectively. The fundamental equation for this model is given by

$$\frac{\partial \overline{\theta}}{\partial t} = \left[\left(\overline{w'\theta'}\right)_S - \left(\overline{w'\theta'}\right)_H\right]\left[\frac{1}{H}\right], \qquad (2.1),$$

where H represents the top height of the mixed layer and the surface is identified by S. Models of this type that examine turbulent behavior over the entire depth of the boundary layer are identified as nonlocal schemes. Alternatively, attempts to quantify turbulent behavior and static stability via localized gradients are identified as local schemes. The latter methods are often inconsistent with observations, as most of the turbulent energy is associated with the largest

eddies, which typically have influence over the full depth of the boundary layer (Stensrud 2007). Figure 4 illustrates nonlocal versus local static stability classification for an example sounding. Parcel displacements follow the nonlocal definition where static stability and flow type are evaluated over the entire atmospheric column. Assessment of the environmental profile and its vertical variation over discrete segments follows the local definition.

As described by Stensrud (2007), equation 2.1 and the concept of local versus nonlocal introduces the fundamental problem associated with boundary layer predictive schemes, namely turbulence closure. As in the previous mixed layer model, instantaneous variables like potential temperature and vertical velocity (w) are expressed in terms of their mean and turbulent (perturbation) components (e.g., $\overline{\theta}$ and θ' or $\overline{w}$ and w', respectively). And although the mean quantity $\left(\frac{\partial\overline{\square}}{\partial t}\right)$ is the desired parameter, it remains a function of turbulent multiples or correlation terms like the buoyancy flux ($\overline{w'\theta'}$). The appearance of the latter in the governing equation set introduces unknown variables that require parameterization (or approximation) where the principles of turbulence closure are utilized. A double correlation term like buoyancy flux would follow first-order turbulence closure. A triple correlation term (three turbulent multiples) would follow second-order closure and so on where the order follows the increase of turbulent multiples. As with static stability assessment, turbulence closure can be performed locally or nonlocally. Nonlocal closure relates unknown variables to known variables at any number of other vertical grid points within the column. Local closure relates known variables to unknowns at nearby vertical grid points. The principles of closure gain in complexity with the addition of

terms and order of moments sought. The reader is referred to Stull (1988) for more in depth description of turbulence closure.

Numerical schemes that characterize the planetary boundary layer (PBL) utilize the principles of turbulence closure to obtain a closed set of prognostic equations for temperature, moisture, and momentum. These equations are then used to quantify TKE, a measure of the intensity of turbulence. Descriptively, the tendency for TKE to increase or decrease is given by

$$\frac{\Delta TKE}{\Delta t} = A + Sh + B + Tr - \varepsilon \qquad (2.2),$$

where A is the advection of TKE by the mean wind, Sh is the shear generation, B is the buoyant production or consumption, Tr is transport by turbulence motions and pressure gradients, and ε is the viscous dissipation rate. Each of the former terms contributes to the generation or consumption of TKE where the intensity declines from the ground upward and dissipation typically identifies the top of the boundary layer. Threshold values of TKE are also commonly used to determine mixed layer height (described below).

The ratio of buoyancy to shear, the two most dominant terms in the TKE equation, defines the RI (Stull 2000). According to Richardson (1921), threshold values of RI can be used to categorize flow type. Values greater than or equal to one signify laminar flow, while those less than one suggest turbulent flow. Richardson (1921) identified a critical value of 0.25 to indicate when turbulent flow is certain. However, since Richardson's work, certain threshold values of RI between 0.25 and 1.0 have been found to be consistent with the TKE dissipation in the boundary layer and the mixed layer height. For example, the value of 0.505 is a threshold used in the operational North American Mesoscale (NAM) Forecast System (Janjić 2001; Lee 2008).

3. Methods and Data

For this study, afternoon mixing height values were computed using the Holzworth, Stull, RI, and TKE for a two-year period (2009-2010) over the contiguous U.S. Source data for height calculations included hourly numerical model soundings and post-processed profiles of aerosol extinction, as measured by satellite-based lidar. Mixing height methods, their source data, and the analysis methods used are described in the following subsections.

a. Holzworth and Stull mixing height methods

Both the Holzworth and Stull methods rely on the principles of static stability and parcel theory. The primary difference between the methods is the source variable, dry versus virtual potential temperature, where the inclusion of moisture in the latter can yield a value greater than the former by as much as 3 °C (Fearon 2000). This difference in the environmental profile with height, particularly near the surface, impacts the buoyancy assessment of the surface parcel and the mixing height calculation (see Fig. 2). The mixing height value from both methods is found at the altitude at which the upward vertical displacement or the positive buoyancy of the surface parcel terminates (also the parcel's intersection with the environmental profile). Parcel displacement(s) for the Holzworth and Stull methods are depicted in Fig. 1 and 4, respectively. Parcel displacements beyond that of the surface parcel for the Stull method (Fig. 4) provide further detail on the static stability, particularly the depth of instability and the associated flow

type. As depicted, the depth of instability is not necessarily consistent with the positive buoyancy of the surface parcel. In such cases, low-level stable air may become well mixed in response to daytime heating or dynamical forcing (see Figs. 4 and 5). Following either outcome, the surface buoyancy would become consistent amongst the methods with differences again tied exclusively to the source variable (see Fig. 2).

b. TKE and RI mixing height methods

Profiles of TKE and its decline with height were examined from model output (data described below) where a threshold value of 0.1 J kg^{-1} is used to identify the mixed layer height (see Fig. 6, left panel). As discussed in Holtslag and Moeng (1991), eddy diffusivity calculations of heat and transport reveal that the value of 0.1 corresponds consistently with boundary layer inversion height. Lee et al. (2008) also describes the use of this threshold for TKE in relation to bulk RI for planetary boundary layer height determination within the operational NAM.

RI represents the ratio of the buoyancy flux and wind shear terms of the TKE equation. In bulk form, the equation takes the following form

$$RI = \frac{(g/\overline{\theta_v})\ \Delta\overline{\theta_v}\ \ \Delta Z}{[(\Delta\bar{U})^2 + (\Delta\bar{V})^2]}, \qquad (3.1),$$

where the numerator represents the buoyancy (also the Brunt-Väisälä frequency) as the vertical change in the mean virtual potential temperature across the layer, and the denominator is the vertical variation of the horizontal wind. In this study, a height consistent with a threshold value of 0.505 (unitless) from RI identified the mixed layer height following a profile search from the

ground upward (Janjić 2001; Lee et al. 2008). An RI calculation that exceeds this value signifies a decline in turbulence (see Fig. 6, right panel). It should be noted that both TKE and RI include vapor content in their respective calculation.

c. Rapid Update Cycle Version 2 (RUC2) analysis data

RUC2 is a hydrostatic model with forty isentropic-sigma hybrid model surfaces defining the vertical structure. Turbulent mixing, including the boundary layer, is prescribed explicitly using the methods of Burk and Thompson (1989), a nonlocal scheme with level two closure (third order moments are parameterized). Additional details on model physics can be found in Benjamin et al. (2004). In this study, RUC2 model analysis grids for the period of 2009 through 2010 were used to generate mixing height values. The hourly frequency and horizontal resolution (13 km) provided collocation opportunities for the satellite-based lidar data (described next; see Fig. 7). Profiles of potential temperature, virtual potential temperature, geopotential height, and horizontal wind components (U and V) from RUC2 grid cells were extracted and used to compute mixed layer height for Holzworth and Stull methods along with bulk RI. TKE profiles were also available and used to determine a mixing height.

d. Lidar data

Aerosol retrievals from the National Aeronautics and Space Administration's (NASA)'s Cloud-Aerosol Lidar and Infared Pathfinder Satellite Observation (CALIPSO) system were used

as an independent measure of mixing height in this study. The CALIPSO satellite follows a sun-synchronous polar orbit with a 16-day repeat cycle (Vaughan et al. 2004). It is part of the Afternoon (A-Train) satellite constellation, which currently includes GCOM-W1, Aqua, CALIPSO, CloudSat, and OCO-2, where equatorial overpass time for CALIPSO is 13:30 local time (NASA 2015). The Vertical Feature Mask (VFM; version 3.01) product was chosen for its simplicity (see Fig. 8), as it is a post-processed version of the aerosol backscatter and provides aerosol depth classification for all or individual constituents. Referencing Fig. 8, the horizontal footprint of the lidar beam is 5 km within which are 15 individual profiles at a horizontal resolution of 333 m. The vertical resolution of each profile is 30 m within the first 8 km of the surface. The orange classification defines the total aerosol depth determined and was chosen to represent the mixed layer depth[5]. For this definition, the base of the aerosol layer had to be in contact or within 60 m of the ground. The top of this aerosol layer defined the mixing height location. If elevated aerosol existed above this layer, and its horizontal width was greater than 2.5 km (half or more of the 5 km swath), a 60 m separation was allowed before a layer discontinuity was assumed. If the horizontal width of the elevated aerosol was less than 2.5 km, a discontinuous layer was assumed. The value choice of 60 m for aerosol layer discontinuity detection represents twice the lidar vertical resolution and was found to be a representative filter to remove unrealistic gaps in the vertical caused by minor beam attenuation. When employed, the local variability of the aerosol profile remained consistent with collocated numerical sounding structure.

[5] The Vertical Feature Mask algorithm is able to discriminate cloud and aerosol when they coexist and therefore mixing height was determined when clouds were present or not.

The use of aerosol extinction, as found in the CALIPSO layer products, as a surrogate of the mixed layer depth has been employed in other studies, namely Leventidou et al. (2013) and Wu et al. (2010). The authors of the latter study found strong consistency with aerosol extinction and VFM classification in the context of mixing height determination. It should be noted that consistent post-processing algorithms for VFM aerosol products influenced the two-year period chosen for this study (2009-2010). Further, unusable retrievals are not uncommon due to beam attenuation, and therefore, a subset of those depicted in Fig. 7 were found to be worthy of mixing height determination. Additional details regarding the CALIPSO system and data can found in Vaughan et al. (2004).

e. Weather Research and Forecasting (WRF) data

In conjunction with mixing heights computed at collocated points from RUC2 and lidar, analysis was also conducted for three geographic regions using the mass core nonhydrostatic Weather Research and Forecasting (WRF; Advanced Research WRF core) model (Skamarock et al. 2008). Three modeling domains at 10 km grid spacing, each with a one-way 2 km nest, were used for three regional extents over the Southeast, the Northern Plains, and the Western United States (Fig. 9). These subregions were selected in order capture a variety of airmass and terrain complexities that affect mixed layer variability across the contiguous U.S. The inner nest choice of 2 km horizontal resolution followed the discussion presented in Moeng and Wyngaard (1988) in conjunction with the finest resolution options possible given local computing resources. The

model configuration remained consistent for all three domains with 47 levels in the vertical extending up to 15 km Above Ground Level (AGL), 18 vertical levels below 1.5 km AGL, with the lowest model level set at 10 m AGL. The model physics included: (1) momentum and heat fluxes at the surface that use an Eta surface layer scheme following Monin-Obukhov similarity theory (Janjić 2001), (2) turbulence parameterization following the Mellor-Yamada-Nakanishi-Niino (MYNN; Nakanishi and Niino 2004), (3) convective processes following the Kain-Fritsch cumulus scheme for 10 km horizontal grid size, (4) cloud microphysical processes following explicit bulk representation of microphysics (Thompson et al., 2004; 2006), (5) radiative processes are parameterized using the Rapid Radiative Transfer Model for long wave radiation (Mlawer et al. 1997) and Dudhia's short wave scheme (Dudhia 1989), and (6) the land-surface processes following the Noah land surface model (Noah LSM) which provides the surface sensible, latent heat fluxes, and upward longwave and shortwave fluxes to the atmospheric model (Chen and Dudhia 2001; Ek et al. 2003). It should be noted that the MYNN turbulence parameterization for planetary boundary layer (PBL) was a critical choice for this study because the buoyancy and shear contributions from TKE are partitioned as separate output variables in WRF.

f. Data analysis methods

Analysis of afternoon mixing height values determined from RUC2, lidar, and WRF is presented in section 4. Height values from the four methods were first examined in terms of their

overall distributions from RUC2 versus lidar. A mixing height difference value of 500 m was chosen to represent a significant discrepancy[6]. Such discrepancies were evaluated further using WRF model output for three geographic regions (Fig. 9). The goal of the latter was to address the two following questions. First, does finer resolution in the horizontal (and vertical) explain height discrepancies amongst the methods, as eddy motions and flux terms represented by the TKE equation would be better resolved? Second, what is the physical meaning of the mixing height value produced by each method, in terms of the vertical structure and across space?

Methods employed to evaluate vertical structure included profile analysis of buoyancy, shear, and virtual potential temperature. Colored maps of TKE contribution, partitioned by term for each 2 km domain, were developed to evaluate spatial variance. Mixing height differences in excess of 500 m at a particular grid point assumed the following color assignment: 1) if buoyancy was present alone, points are colored red; 2) if shear was present alone, points are colored green; 3) if both terms were operative, points were colored blue; and 4) if neither term was operative, points were colored black signifying advection and or topographic effects were active for an elevation in excess of 250 m. TKE contribution for buoyancy and shear was examined through perturbation values. Such values were computed for each model level using the value at each grid point minus the average over the entire domain. These deviations were then integrated through column for levels within the determined mixed layer volume.

[6] This value derives from Holzworth (1964) where the minimum mean annual mixing height value range over the contiguous U.S. was found to be 200-800 m. The 500 m value represents the midpoint.

4. Discussion of results

a. Mixing heights from RUC2 and Lidar

Figure 10 illustrates the distributions of mixing height values computed for all four methodologies using RUC2 data (light blue) versus those estimated from lidar (red). Overall, a low-value bias is prevalent across all method distributions with values from RI and Stull revealing a slightly larger variance. Examination of the median value differences (departure from lidar) reveals deviations (rounded to the nearest integer) of 100 m, 200 m, 200 m, and 650 m for RI, Stull, TKE, and Holzworth, respectively. In the case of Holzworth, 450 m of the median deviation (the departure from Stull) corresponds directly to the exclusion of vapor content. As described in section 3a, the fundamental difference between the Holzworth and Stull mixing height calculation rests on the source variable, dry versus virtual potential temperature, respectively. Therefore, if Holzworth heights were recomputed using θ_v instead of θ, values would become synonymous with those from Stull.

Figure 11a is similar to Fig. 10, except now scatter comparisons of height (each method versus lidar) are shown. One-to-one distribution trends are similar from TKE, Stull, and RI, and reaffirm the small median departures in Fig. 10, although variance and patterns of low-value bias are not consistent. Note the linear collection of points along the x-axis depicted in Stull (and Holzworth) versus lidar. For either method, a near zero height is indicative of a subtle low-level inversion prematurely capping surface parcel buoyancy. Since this pattern is missing from the TKE and RI distributions, mixed layer growth on these particular days was likely a result of

dynamical forcing (e.g., shear) and that static stability assessment alone was not sufficient. This situation can persist or be temporary depending on the meteorological environment (e.g., thermal capping or shear increasing, respectively). In persistent cases, inversion strength becomes important and is reflected by low-value mixing heights from all the methods. However, in the majority of cases, subtle near-surface inversions are properly resolved when vapor and or wind shear are accounted for in the mixing height calculation. Figure 11b (representative of yellows points in Fig. 11a) exemplifies such a scenario for a grid cell just west of Savannah, Georgia (May 1, 2009, 19:00 UTC, 3pm local time) where a subtle, near-surface inversion in potential temperature leads to underestimated mixing height value from the Holzworth method (blue line). The inclusion of moisture properly resolves the potential temperature profile via the Stull method (red line), although the true depth of the mixed layer is function of static and dynamic stability per the values of TKE and RI (purple and green lines, respectively). The inclusion of both static and dynamic stability in the RI and TKE methods is reflective in their distributions against lidar (Fig. 11a) where, in general, scatter is more symmetric about one-to-one line. For the RI distribution, variance is larger overall and more evenly spread. The one-to-one relationship of TKE versus lidar reveals less variance throughout, even though a low-value bias exists.

To quantify distribution similarities, height values from Stull, TKE, and RI (Holzworth excluded) were examined spatially. First, daily height values from these three methods are presented as a combined mean value, where the deviation from lidar (absolute value difference) at coincident locations is shown in Fig. 12. Red (black) dots represent difference values of 500 m or greater (less). The percentage of red and black dots is 35 and 65% of the total, respectively. Fig. 13 is a replicate of Fig. 12, except now red (black) dots represent height deviations across

the three methods only, lidar height removed. Now, the percentage of red and black dots is 15 and 85%, respectively. These two calculations reveal that large height differences (across methods) occur 15% of time, and when method results are combined, mean values differ from lidar 20% of the time (35 minus 15%). Height discrepancies per method are likely produced due to dynamical processes, where method inclusion or not and the level of representation (of the dynamics terms) impacts the mixing height value. The 20% departure from lidar height may also suggest mixing height overestimation from lidar where the vertical distribution of aerosol is not always fully representative, particularly the upper bound.

Lidar height being an overestimate is conjecture, but could have merit under the following circumstances. For instance, mixing height estimation from lidar is defined by the aerosol termination or the first sizeable discontinuity with height, per the vertical feature mask product described in section 3d. What if the aerosol top was not sharply delineated, but instead diffuse across the mixed layer boundary as a result of the entrainment process (see Fig. 3)? In the entrainment zone, internal fluid properties of heat, moisture, and momentum from the mixed layer air below are vigorously stirred with the air above (from the free atmosphere). Therefore, the delineation of aerosol particles may be a function of the entrainment intensity and the derived mixing height value may be accurate to within a few hundred meters. Of course, the quantity and type of aerosol present has implications on this theory. Aerosol type (e.g., dust, smoke, continental versus marine) was examined for several locations and type discrimination did not impact the altitude of the aerosol top. In addition, the confidence value provided for feature classification (e.g., aerosol versus cloud particle or other) was examined. Restriction of pixels associated with lower confidence did not impact results.

b. Mixing height differences – evaluation of vertical structure using WRF

For this exercise, each of the three yellow dots in Fig. 13 identified a significant mixing height difference or discrepancy amongst the TKE, Stull and RI methods. Regional classification names, i.e., Southeast, Northern Plains, and West, were used to reference each point. Table 2 shows the breakdown of mixing height values for each location for each method for both the RUC2 and WRF model output. Model estimates are delineated by a forward slash in the Table (e.g, RUC2 / WRF). Lidar height values are also given. Holzworth heights were excluded from this analysis simply because the method mechanics are identical to the surface parcel displacement used for Stull where the use/disuse of vapor content is the only outstanding difference in the calculation.

For RUC2 at the Southeast location there is a discrepancy in the TKE value relative to the Stull, RI, and lidar values, which are within 100 m of each other. Using WRF data, the discrepancy has been improved for TKE, although the RI value has now become a slight underestimate. Further evaluation follows in Fig. 14 where profiles of TKE-buoyancy (red), TKE-shear (green), and virtual potential temperature (blue) are illustrated at five-minute intervals over for the afternoon hours (1705 to 0000 UTC), left and right panels, respectively. The lidar sample time of 1900 UTC is shown by the yellow curves. In this case, dissipation of the TKE- buoyancy/shear and the extent of surface parcel buoyancy approximately coincide (i.e., the convergence with height of the yellow curve(s) on zero and with the vertical black line, left and right panels, respectively). Additional TKE- buoyancy/shear and surface parcel rise does

occur following the lidar sample time, as noted by the slightly elevated red/green and blue points, respectively, above the horizontal black line. Figure 15 confirms the view of the vertical structure where the mixing height through time is depicted for the three methods. Note the intersection of Stull and TKE height near the lidar sample time. Over the remaining afternoon hours, height from TKE eventually exceeds Stull height with RI values remaining lower. The latter emphasizes the importance of other dynamical forcing (e.g., advection) likely contributing to TKE height along with TKE- buoyancy/shear perturbation components missing in the bulk RI calculation.

A second example for a point locale in the Northern Plains is shown in Table 2 and Fig. 16. In this case, there is a large height discrepancy across all methods where TKE height is +2,000 m greater from RUC2. However, discrepancies are fairly well resolved for the TKE and Stull WRF-based heights. Results illustrated in Fig. 16 and 17 are consistent with the previous example and follow the same description.

A third example for a point in northern Nevada (West) is shown in Table 2 and Fig. 18. In this case, the TKE height discrepancy from RUC2 is improved but an ~400 m difference remains between TKE and Stull values. Unlike the two previous cases, there is a much deeper contribution from TKE-shear present (solid yellow curve Fig. 18, left panel). Greater TKE-shear likely corresponds to the presence of complex terrain, and with a heterogeneous mountain-valley landscape like central Nevada, daytime upslope flow accelerations in response to surface heating are common. Like the two previous examples, mixing height from the three methods follow a similar trend over the afternoon hours (Fig. 19).

Mixing height determination with higher resolution numerical soundings does better resolve method discrepancies. Height values from TKE and Stull appear to collapse on each other for a period of time before an elevated separation develops during the mid-late afternoon where TKE reveals a higher value. The question then becomes, is a consistently higher height value from TKE a result of perturbation terms; is it a function of additional terms in the TKE equation (e.g, advection); or, is TKE (and its chosen threshold) simply an overestimate? In the next subsection, a spatial analysis of TKE- buoyancy and shear perturbations, including terrain aspects, sheds more light on this discussion. RI is not included in the remaining analysis, as it is truly a proxy for TKE with a more conservative threshold.

c. Mixing height differences – evaluation of spatial variance using WRF

Figure 20 (left panel) illustrates the height value differences between the methods (TKE minus Stull) over the Southeast U.S. WRF 2 km domain. Differences appear subtle due to the fine resolution, but are present nonetheless. The center panel of Fig. 20 portrays the differences in terms of the perturbations using the grid cell coloring approach (section 3f). Higher TKE values due to buoyancy are present in isolated locations. Green (shear) and blue (buoyancy and shear) cells are noteworthy where the low-level flow field (largely anticyclonic, Fig. 20, right panel) has slight speed/directional changes imbedded. Contributions are also evident near terrain rises and coastlines where the upstream flow is orthogonal. The most interesting differences are located on the leeward slope of the southern Appalachians over western North Carolina, where Stull values exceed those from TKE. This pattern is consistent with leeward airmass descent and

warming in the surface layer at the lower elevation. This conjecture is supported by the northwesterly flow upstream, which is orthogonal to higher terrain on approach, where air rises (descends) and cools (warms) on the windward (leeward) slope. In this situation, a strong superadiabatic surface layer ensues at lower elevation southeast of the higher terrain and the low-level parcel buoyancy is maximized. This discrepancy between Stull and TKE height values was found to be temporary (~2 hours), as the air column mixed vertically, with TKE eventually portraying an elevated value similar to the profile examples. Overall, higher TKE values are well explained via perturbation components of buoyancy and shear suggesting that elevated values are a byproduct.

Figure 21 portrays a second example for a 2 km WRF domain over the Northern Plains. Here, larger TKE values dominate again with a few isolated Stull values over southern North Dakota (left panel). As before the larger Stull values were found to be temporary. In this situation, the low-level flow is confluent overall with cyclonic and anticyclonic regimes, northwest and southeast, respectively (right panel) amplifying the westerly advection (right panel). There are some impressive terrain rises in western South Dakota and eastern Wyoming, not excluding the moderate high points in west-central Minnesota. These locations reveal larger TKE values (left and center panel) orchestrated by terrain rises and orthogonal advection upstream. Elsewhere, perturbations in buoyancy and shear independently or together promote larger TKE values.

Figure 22 represents a third spatial example over the West highlighting central Nevada. Complex terrain dominates the landscape with predominately weak southerly flow (right panel). There are several north-south mountain ranges across Nevada, and mixing height differences are

found along these features (left panel). In this example, higher Stull height values are more evident, which were largely explainable due to superadiabatic surface layers. As before, such differences were found to be temporary and surpassed by TKE. Shear-based differences are scattered across central-eastern Nevada in the presence of light/variable flow (center and right panel). Elsewhere, differences are explained by buoyancy alone or together with shear.

Overall, larger mixing height differences (TKE versus Stull) are well explained by the spatial perturbation analysis. Grid cells of perturbation types were collocated with large height differences (greater 500 m). Buoyancy perturbations were also found in grid cells where height differences were less than 500 m, however, the magnitude of the perturbation was reduced. The same can be said for shear- and terrain-, including advective-based perturbations unless the flow was highly amplified, curved, or orthogonal to topographic irregularities. These findings in combination with TKE's robust account of all turbulent motion sources, particularly those associated with dynamical processes, explain why height differences exist between these two methods.

5. Conclusions

In this study, mixing height values from four methods: TKE, Stull, RI, and Holzworth, were examined. Results from each method were compared with one another and against lidar-derived mixing height estimates. A series of diagnostic analyses were also conducted over space and time for point locations and spatial extent where topographic features and airmass exposure are highly variable. Table 3 provides a breakdown of advantages and disadvantages for each method.

The TKE method stands out as the most robust in terms of inclusiveness of both thermodynamic and dynamic processes in the boundary layer. Lee et al. (2008) discussed how TKE may be an overestimate of the true mixed layer depth due to the entrainment of TKE by horizontal and vertical advection and diffusion processes near the PBL top using the 12 km NAM model. However, these processes facilitate mixing through the entire column and precise discrimination near the PBL top may require reexamination of a chosen TKE threshold (e.g., 0.1 J kg^{-1}). Case examples shown in this paper demonstrate that large mixing height differences occur when dynamical processes influence the overall calculation (e.g., 15% of the time, Fig. 13 section 4a). Mixing height sensitivity to shear and buoyancy perturbations, including advection, as shown in section 4d also demonstrates the importance of dynamical processes and that a numerical formulation of TKE is required to capture such processes.

The Stull method proves to be a reasonable approach to mixed layer height estimation. However, the method relies on parcel theory and displacement thermodynamics only. The bulk RI approach is an attempt to remedy dynamical exclusion, but advective processes and perturbation components are not included. The use of the RI flux number, inclusive of perturbation components, would be a more complete treatment. However, use of the latter, like TKE, would require a numerical model to calculate perturbation terms.

As mentioned earlier, the use of the Holzworth method is discouraged overall. Its use in arid locales when low humidities are present has merit; however, the viewpoint of the unsaturated atmosphere via virtual potential temperature accommodates both dry and or moist (unsaturated) situations. Therefore, use of the dry potential temperature for this application is unnecessary.

Based on the findings of this study, the authors recommend the TKE method for operational mixing height prediction. And although this methodology requires a fine-resolution numerical model, of at least 5 km horizontal resolution[7], this approach yields a derived mixing height value inclusive of both thermodynamic and dynamic processes where the mixing budget (in the vertical and horizontal) is quantified using a prognostic equation as part of a numerical PBL scheme. An alternative to TKE-based mixing height is the diagnostic variable "PBL height" which is available as part of operational NAM model output. The bulk RI and Stull methods are both sound diagnostic approaches with minor shortcomings (see Table 3), but represent viable alternatives when numerical model output with TKE is unavailable.

Acknowledgments. The authors wish to thank Joseph J. Charney, Scott L. Goodrick, Michael L. Kaplan, John M. Lewis, Brian E. Potter, and John Tomko for their constructive comments and editorial assistance. We are grateful to Erin C. Gleason for her assistance with graphics, and wish to acknowledge NWA JOM Editors Jon Zeitler and Michael C. Coniglio, and the three reviewers who provided comments that improved the manuscript. The authors also acknowledge the cooperation and collaboration of the U.S. Department of Energy as part of the Atmospheric Radiation Measurement Climate Research Facility who provided the RUC2 analysis grids used in this study. Partial support for this project was provided by the USDA Forest Service California and Nevada Smoke and Air Committee Agreement Number 09-CS-11052012-266 and the USDA Forest Service National Interagency Fire Center Agreement Number 11-CS-11130206-075.

REFERENCES

[7] The 5 km assertion (corresponding to fine resolution) comes based on the lidar swath resolution used in this study, the discussion in Moeng and Wyngaard (1988), and the current operational NAM horizontal resolution of 5 km over the U.S. Conus.

American Meteorological Society, cited 2015: Virtual Potential Temperature. Glossary of Meteorology. [Available online at http://glossary.ametsoc.org/wiki/climatology.]

Ball, F. K., 1960: Control of inversion height by surface heating. *Q. J. R. Meteorol. Soc.*, **86**, 483–494, doi:10.1002/qj.49708637005.

Benjamin, S. G., G. A. Grell, J. M. Brown, T. G. Smirnova, and R. Bleck, 2004: Mesoscale Weather Prediction with the RUC Hybrid Isentropic–Terrain-Following Coordinate Model. *Mon. Weather Rev.*, **132**, 473–494, doi:10.1175/1520-0493(2004)132<0473:MWPWTR>2.0.CO;2.

Betts, A. K., 1973: Non-precipitating cumulus convection and its parameterization. *Q. J. R. Meteorol. Soc.*, **99**, 178–196, doi:10.1002/qj.49709941915.

Burk, S. D., and W. T. Thompson, 1989: A Vertically Nested Regional Numerical Weather Prediction Model with Second-Order Closure Physics. *Mon. Weather Rev.*, **117**, 2305–2324, doi:10.1175/1520-0493(1989)117<2305:AVNRNW>2.0.CO;2.

Chen, F., and J. Dudhia, 2001: Coupling an Advanced Land Surface–Hydrology Model with the Penn State–NCAR MM5 Modeling System. Part I: Model Implementation and Sensitivity. *Mon. Weather Rev.*, **129**, 569–585, doi:10.1175/1520-0493(2001)129<0569:CAALSH>2.0.CO;2.

Dudhia, J., 1989: Numerical Study of Convection Observed during the Winter Monsoon Experiment Using a Mesoscale Two-Dimensional Model. *J. Atmos. Sci.*, **46**, 3077–3107, doi:10.1175/1520-0469(1989)046<3077:NSOCOD>2.0.CO;2.

Ek, M. B., 2003: Implementation of Noah land surface model advances in the National Centers for Environmental Prediction operational mesoscale Eta model. *J. Geophys. Res.*, **108**, 8851, doi:10.1029/2002JD003296.

Fearon, M. G., 2000: The Use of Nonlocal Static Stability to Determine Mixing Height from NCEP Eta Model Output over the Western U.S. University of Nevada Reno, 144 pp.

Holtslag, A. A. M., and C.-H. Moeng, 1991: Eddy Diffusivity and Countergradient Transport in the Convective Atmospheric Boundary Layer. *J. Atmos. Sci.*, **48**, 1690–1698, doi:10.1175/1520-0469(1991)048<1690:EDACTI>2.0.CO;2.

Holzworth, G. C., 1964: Estimates of Mean Maximum Mixing Depths in the Contiguous United States. *Mon. Weather Rev.*, **92**, 235–242, doi:10.1175/1520-0493(1964)092<0235:EOMMMD>2.3.CO;2.

——, 1967: Mixing Depths, Wind Speeds and Air Pollution Potential for Selected Locations in the United States. *J. Appl. Meteorol.*, **6**, 1039–1044, doi:10.1175/1520-0450(1967)006<1039:MDWSAA>2.0.CO;2.

Janjić, Z. I., 2001: *Nonsingular Implementation of the Mellor-Yamada Level 2.5 Scheme in the NCEP Meso model*. Camp Springs, MD, NCEP Office Note, No. 437, 61 pp.

Jeričević, A., and B. Grisogono, 2006: The critical bulk Richardson number in urban areas: Verification and application in a numerical weather prediction model. *Tellus, Ser. A Dyn. Meteorol. Oceanogr.*, **58**, 19–27, doi:10.1111/j.1600-0870.2006.00153.x.

Kiefer, M. T., W. E. Heilman, S. Zhong, J. J. Charney, and X. Bian, 2015: Mean and Turbulent Flow Downstream of a Low-Intensity Fire: Influence of Canopy and Background Atmospheric Conditions. *J. Appl. Meteorol. Climatol.*, **54**, 42–57, doi:10.1175/JAMC-D-14-0058.1.

Lee, P., and Coauthors, 2008: Impact of consistent boundary layer mixing approaches between NAM and CMAQ. *Environ. Fluid Mech.*, **9**, 23–42, doi:10.1007/s10652-008-9089-0.

Leventidou, E., P. Zanis, D. Balis, E. Giannakaki, I. Pytharoulis, and V. Amiridis, 2013: Factors affecting the comparisons of planetary boundary layer height retrievals from CALIPSO, ECMWF and radiosondes over Thessaloniki, Greece. *Atmos. Environ.*, **74**, 360–366, doi:10.1016/j.atmosenv.2013.04.007.

Lewis, J. M., 2007: Use of a Mixed-Layer Model to Investigate Problems in Operational Prediction of Return Flow. *Mon. Weather Rev.*, **135**, 2610–2628, doi:10.1175/MWR3430.1.

Lilly, D. K., 1968: Models of cloud-topped mixed layers under a strong inversion. *Q. J. R. Meteorol. Soc.*, **94**, 292–309, doi:10.1002/qj.49709440106.

Mlawer, E. J., S. J. Taubman, P. D. Brown, M. J. Iacono, and S. A. Clough, 1997: Radiative transfer for inhomogeneous atmospheres: RRTM, a validated correlated-k model for the longwave. *J. Geophys. Res.*, **102**, 16663, doi:10.1029/97JD00237.

Moeltner, K., M.-K. Kim, E. Zhu, and W. Yang, 2013: Wildfire smoke and health impacts: A closer look at fire attributes and their marginal effects. *J. Environ. Econ. Manage.*, **66**, 476–496, doi:10.1016/j.jeem.2013.09.004.

Moeng, C-H and J.C. Wyngaard, 1988: Spectral analysis of large-eddy simulations of the convective boundary layer. *J. Atmos. Sci.*, **45**, 3573–3587, doi: http://dx.doi.org/10.1175/1520-0469(1988)045<3573:SAOLES>2.0.CO;2

Nakanishi, M., and H. Niino, 2004: An Improved Mellor–Yamada Level-3 Model with Condensation Physics: Its Design and Verification. *Boundary-Layer Meteorol.*, **112**, 1–31, doi:10.1023/B:BOUN.0000020164.04146.98.

National Aeronautics and Space Administration (NASA), 2015: The Cloud-Aerosol Lidar and Infrared Pathfinder Satellite Observation (CALIPSO). http://www-calipso.larc.nasa.gov/ (Accessed July 10, 2015).

Pasquill, F., 1961: The Estimation of the Dispersion of Windborne Material. **90**, 33–49.

Richardson, L. F., 1921: Some Measurements of Atmospheric Turbulence. *Philos. Trans. R. Soc. A Math. Phys. Eng. Sci.*, **221**, 1–28, doi:10.1098/rsta.1921.0001.

Seibert, P., F. Beyrich, S.-E. Gryning, S. Joffre, A. Rasmussen, and P. Tercier, 1997: *Mixing height determination for dispersion modelling*. European Commission, Report of Working Group 2 of the COST Action 710, 120 pp.

——, ——, ——, ——, ——, and ——, 2000: Review and intercomparison of operational methods for the determination of the mixing height. *Atmos. Environ.*, **34**, 1001–1027, doi:10.1016/S1352-2310(99)00349-0.

Shamrock, W. C., and Coauthors, 2008: *A Description of the Advanced Research WRF Version 3*. Boulder, CO, NCAR/TN–475+STR, 113 pp.

Stensrud, D. J., 2007: *Parameterization Schemes: Keys to Understanding Numerical Weather Prediction Models*. Cambridge University Press, Cambridge, 480 pp.

Stull, R. B., 1988: *An Introduction to Boundary Layer Meteorology*. Kluwer Academic Publishers, Dordrecht, Netherlands, 666 pp.

——, 1991: Static Stability—An Update. *Bull. Am. Meteorol. Soc.*, **72**, 1521–1529, doi:10.1175/1520-0477(1991)072<1521:SSU>2.0.CO;2.

——, 2000: *Meteorology for Scientists and Engineers*. Brooks/Cole, Pacific Grove, California, 502 pp.

Tennekes, H., 1973: A Model for the Dynamics of the Inversion Above a Convective Boundary Layer. *J. Atmos. Sci.*, **30**, 558–567, doi:10.1175/1520-0469(1973)030<0558:AMFTDO>2.0.CO;2.

——, and A. G. M. Driedonks, 1981: Basic entrainment equations for the atmospheric boundary layer. *Boundary-Layer Meteorol.*, **20**, 515–531, doi:10.1007/BF00122299.

Thompson, G, R. M. Rasmussen, and K. Manning, 2004: Explicit forecasts of winter precipitation using an improved bulk microphysics scheme. I: Description of sensitivity analysis. *Mon. Wea. Rev.,* **132,** 519-542.

——, P. R. Field, W. D. Hall, R. M. Rasmussen, 2006: A new bulk microphysics parameterization for WRF and MM5. Seventh Weather and Research Forecasting Workshop, National Center for Atmospheric Research, Boulder, CO, NCAR.

Turner, D. B., 1964: A Diffusion Model for an Urban Area. *J. Appl. Meteorol.*, **3**, 83–91, doi:10.1175/1520-0450(1964)003<0083:ADMFAU>2.0.CO;2.

U.S. EPA, O. of A. and R., 2015: History | Clean Air Act | US EPA. http://www.epa.gov/air/caa/amendments.html (Accessed January 15, 2015).

Vaughan, M. A., S. A. Young, D. M. Winker, K. A. Powell, A. H. Omar, Z. Liu, Y. Hu, and C. A. Hostetler, 2004: Fully automated analysis of space-based lidar data: an overview of the

CALIPSO retrieval algorithms and data products. *Remote Sensing*, U.N. Singh, Ed., International Society for Optics and Photonics, 16–30.

Vogelezang, D. H. P., and A. A. M. Holtslag, 1996: Evaluation and model impacts of alternative boundary-layer height formulations. *Boundary-Layer Meteorol.*, **81**, 245–269, doi:10.1007/BF02430331.

Wu, Y., C.-M. Gan, L. Cordero, B. Gross, F. Moshary, and S. Ahmed, 2010: PBL-height derivation from the CALIOP/CALIPSO and comparing with the radiosonde and ground-based lidar measurements. *Remote Sensing*, U.N. Singh and G. Pappalardo, Eds., International Society for Optics and Photonics, 78320C – 78320C – 7.

Yamada, T., and S. Berman, 1979: A Critical Evaluation of a Simple Mixed-Layer Model with Penetrative Convection. *J. Appl. Meteorol.*, **18**, 781–786, doi:10.1175/1520-0450(1979)018<0781:ACEOAS>2.0.CO;2.

Zilitinkevich, S., and A. Baklanov, 2002: Calculation Of The Height Of The Stable Boundary Layer In Practical Applications. *Boundary-Layer Meteorol.*, **105**, 389–409, doi:10.1023/A:1020376832738.

TABLES AND FIGURES

Table 1. Survey of mixing height methodology used (as a first look) by two randomly chosen National Weather Service Forecast Offices within each of the six regions.

Region	Forecast Office	Identifier	Method Used	Office Telephone
Pacific	Guam	GUM	Not sure of method	671-472-0900
Pacific	Hawaii	HFO	Not sure of method*[1]	808-973-5286
Western	Missoula	MSO	Holzworth[2]	406-329-4840
Western	Sacramento	STO	Holzworth	916-979-3051
Eastern	Greenville	GSP	Holzworth	864-848-3859
Eastern	State College	CTP	Holzworth	814-231-2408
Central	Duluth	DLH	Holzworth	218-729-6697
Central	Jackson	JKL	Holzworth	606-666-8000
Southern	Birmingham	BMX	Holzworth[3]	205-664-3010
Southern	Little Rock	LZK	Holzworth*	501-834-0308
Alaska	Fairbanks	AFG	Holzworth	907-271-5088 / 907-458-3700
Alaska	Anchorage	AFC	Holzworth	907-271-5088 / 907-266-5105

*Not satisfied with grid data provided
[1] High moisture content & inversions, not reflected in grids
[2] Currently evaluating Stull versus Holzworth methodology
[3] Current methodology under discussion

Table 2. RUC2 / WRF mixing height values from each method and CALIPSO for the three case example locations (yellow dots in Figure 13).

	Mixing Height (m)		
Method	Southeast	Northern Plains	West
TKE	1444 / 2184	3026 / 2519	1415 / 3439
Stull	2022 / 2089	1102 / 2661	2652 / 2905
RI	1931 / 1659	837 / 1419	2194 / 2616
Lidar	1965	2995	1846

Table 3. Summary of mixing height method advantages and disadvantages

Method	Advantages	Disadvantages
TKE	◆ Incorporates all turbulent sources/sinks (buoyancy, shear, advection, terrain influence, and others)	◆ Fine resolution model dependency (e.g., 5 km or less)
Bulk RI	◆ Not model dependent ◆ Buoyancy and shear ◆ Surrogate for TKE dominant terms	◆ Mean profile state exclusively, turbulent perturbations excluded ◆ Excludes advection
Stull	◆ Not model dependent ◆ Diagnostic method for entire profile ◆ Quick interpretation	◆ Mean profile state exclusively, turbulent perturbations excluded ◆ Buoyancy only
Holzworth	◆ Not model dependent ◆ Quick interpretation	◆ Mean profile state exclusively, turbulent perturbations excluded ◆ Dry atmosphere ◆ Surface parcel buoyancy only

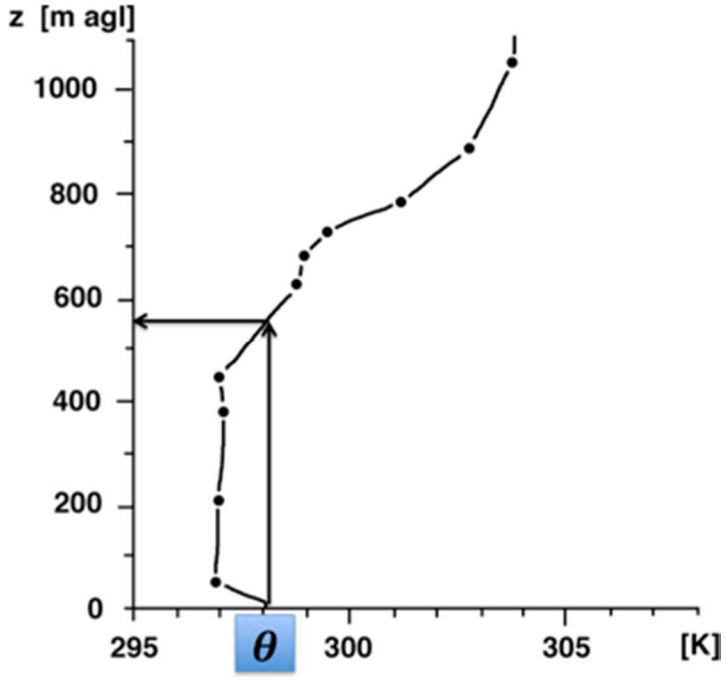

Figure 1. Illustration surface parcel displacement (vertical arrow line) with potential temperature (dry atmospheric assumption) associated with the Holzworth method. The horizontal arrow line denotes mixing height location.

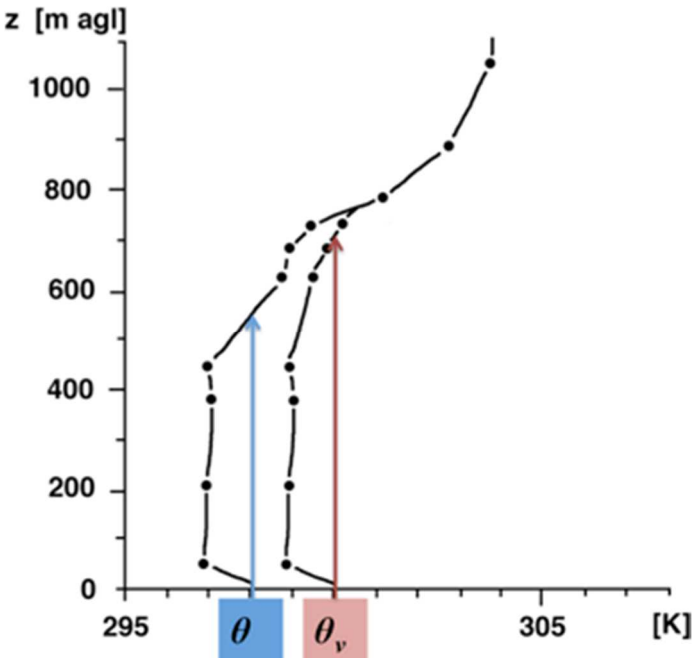

Figure 2. Dry versus moist (unsaturated) atmosphere via potential (blue) and virtual potential (red) temperature, respectively. Note the impact on the surface parcel displacement and the difference between dry and moist (unsaturated) values.

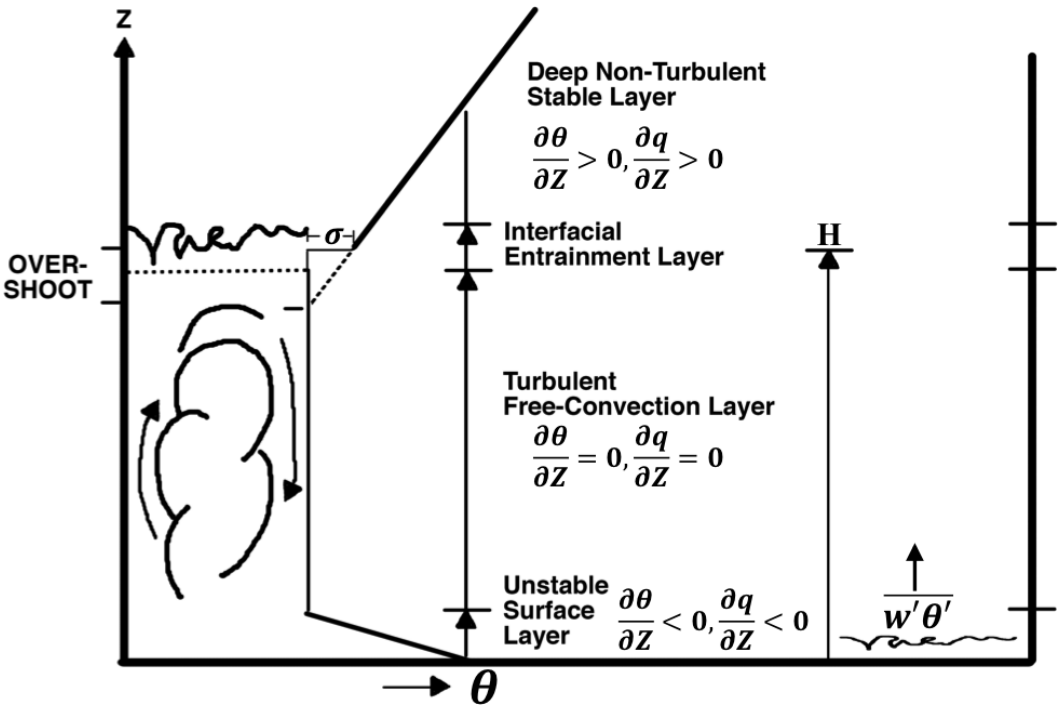

Figure 3. Illustration adapted from Lewis (2007) of the classic mixed layer model at the mature stage. Note the sharp decrease in potential temperature ($\boldsymbol{\theta}$) and the upward acceleration arrow associated with the buoyancy flux ($\overline{w'\theta'}$) in the surface layer, the uniform profile in the free-convection layer, and the increase or jump ($\boldsymbol{\sigma}$) near the mixed-layer top ($\boldsymbol{H}$) associated with the entrainment layer.

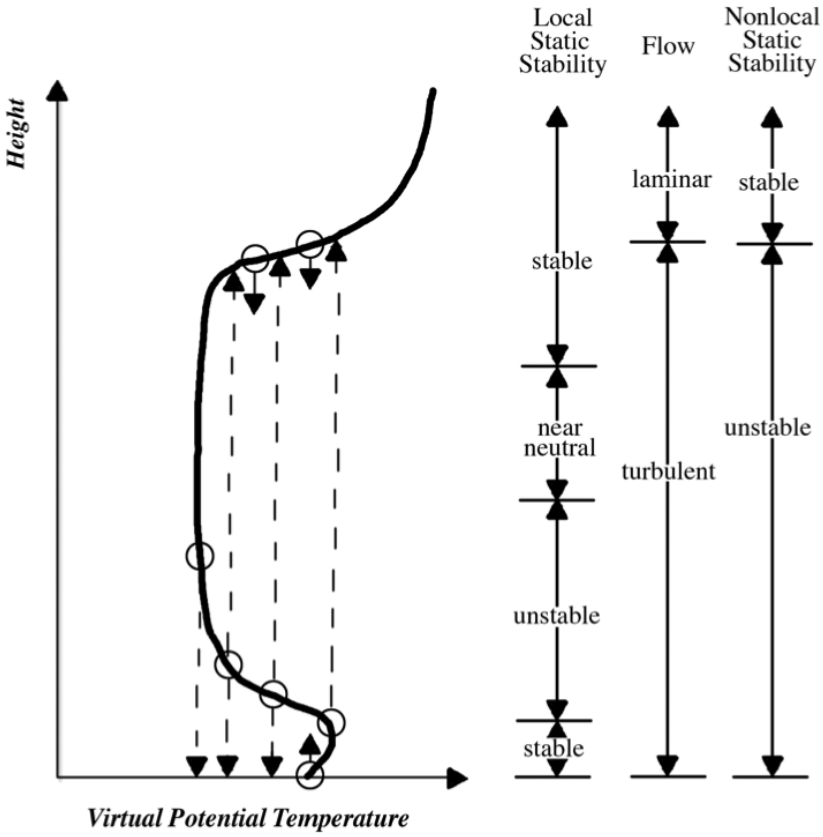

Figure 4. Adapted from Stull (1991). Depiction of parcel displacements associated with the Stull method via the virtual potential temperature, including local versus nonlocal static stability and flow type.

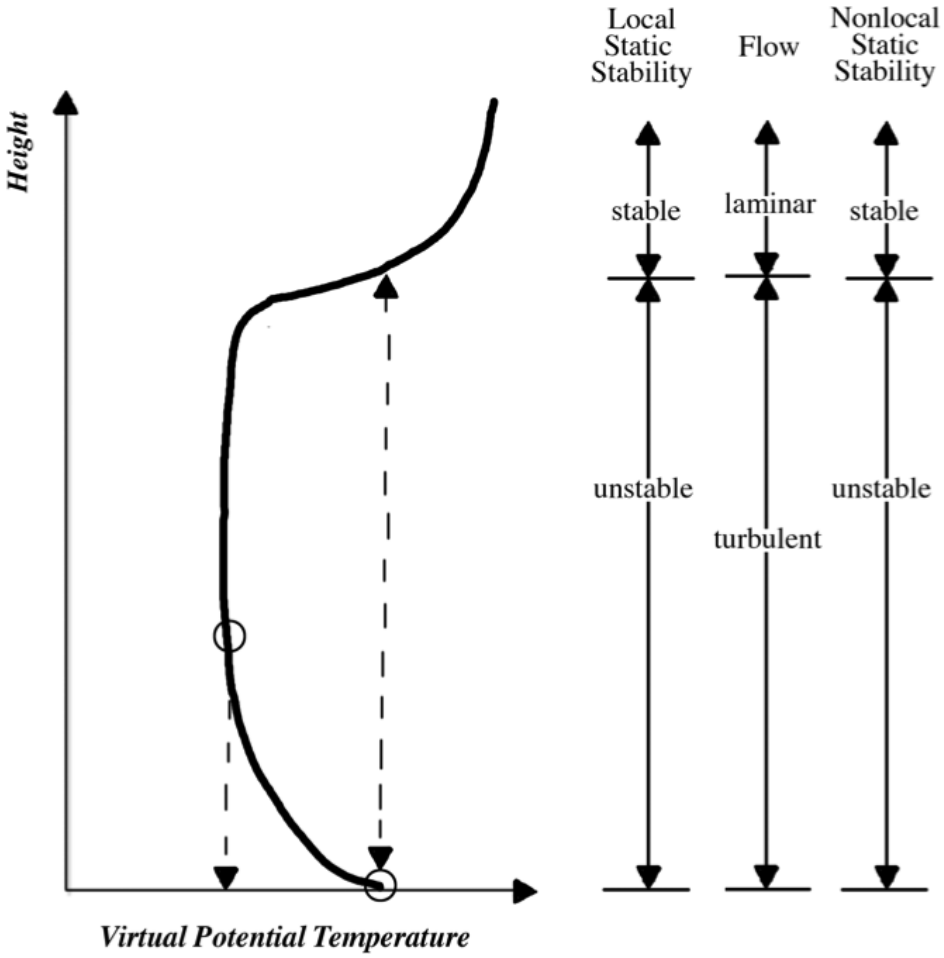

Figure 5. Same as Figure 4 except the low-level inversion has now mixed out. Local and nonlocal static stability are now equivalent.

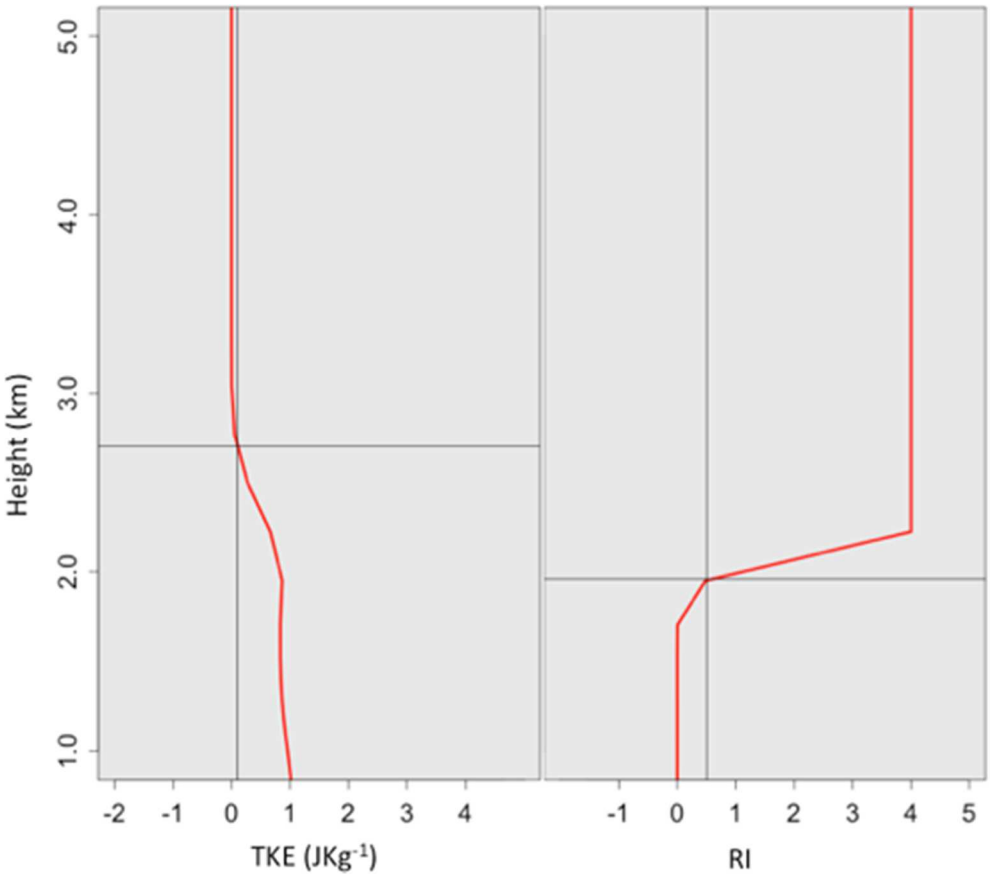

Figure 6. Illustration of the TKE (left) and RI (right) mixing height method mechanics. The thin black vertical lines profile the threshold limits of 0.1 J kg-1 and 0.505, respectively. The thin black horizontal lines depict mixing height location in relation to the threshold limits.

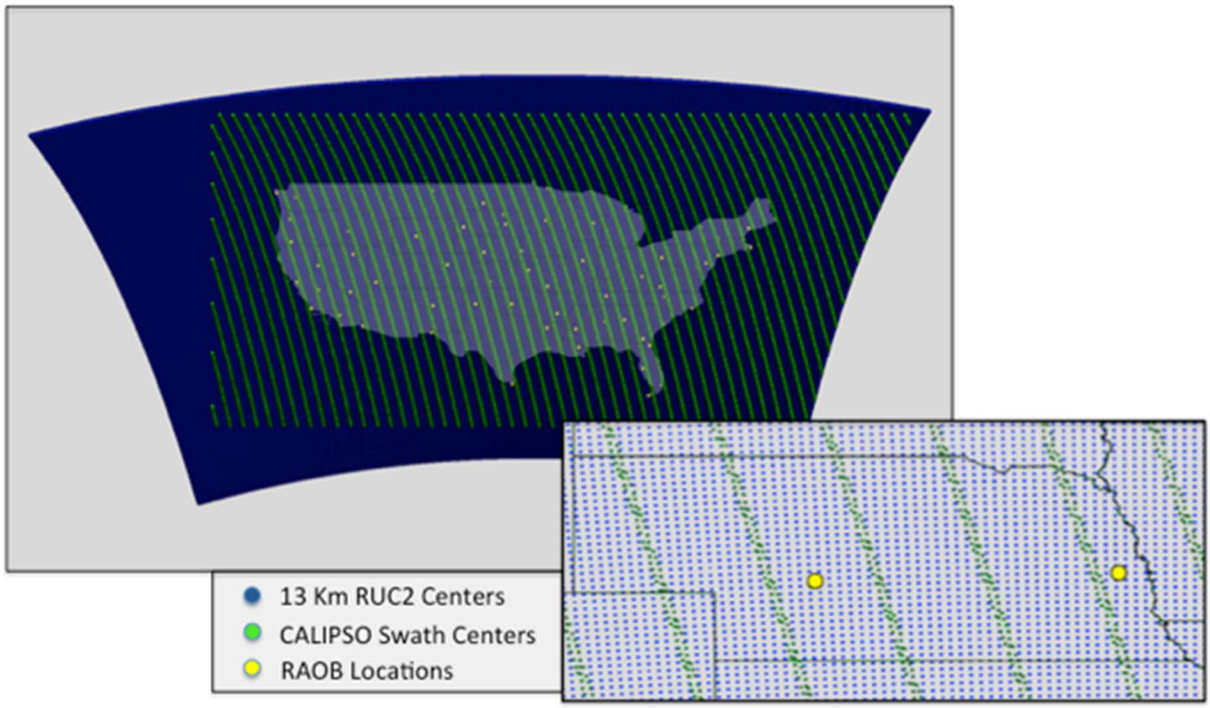

Figure 7. Illustration of the RUC2 (blue) centroids in relation to the CALIPSO lidar 5 km swath centers (green) over the contiguous US. Yellow dots depict radiosonde locations. Note how lidar footprints and radiosonde locations are often not collocated.

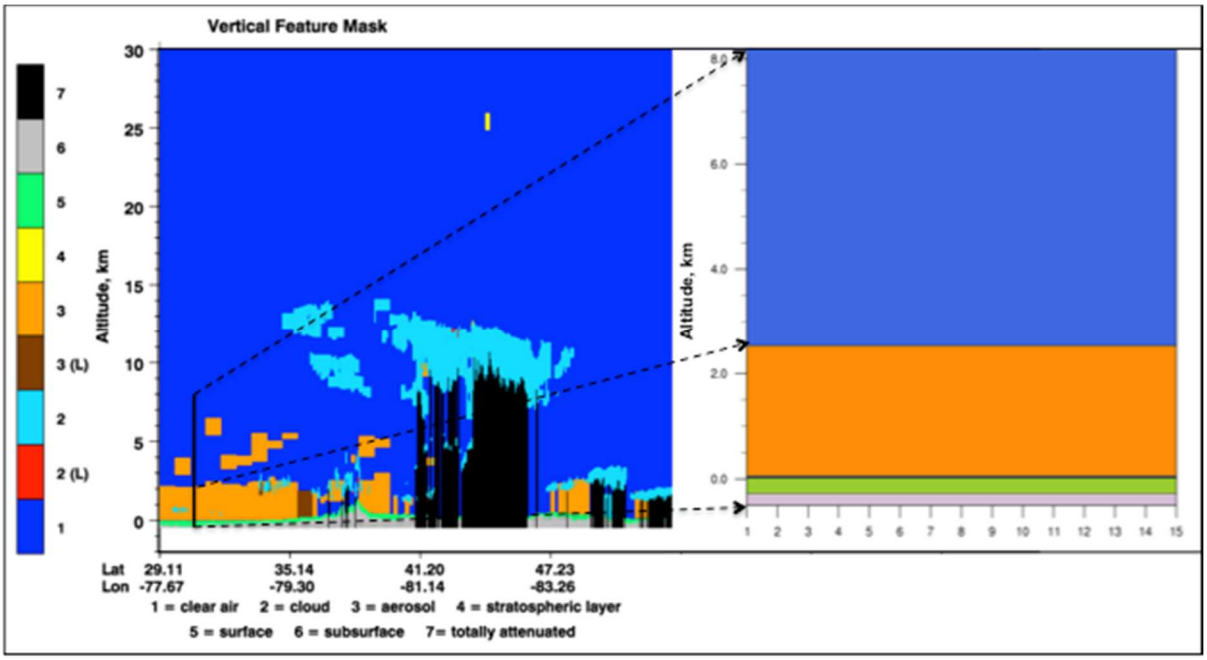

Figure 8. CALIPSO Vertical Feature Mask browse image for a 5 km wide lidar footprint (south to north trajectory) and the associated feature classifications, where orange illustrates total aerosol within the column (left image). Footprint data are stored as sub blocks comprised of 15 individual profiles where the vertical and horizontal resolution of each profile is 60 m x 333 m, respectively, within the first 8 km (right image). In this example, mixing height would be approximately 2.5 km aboveground.

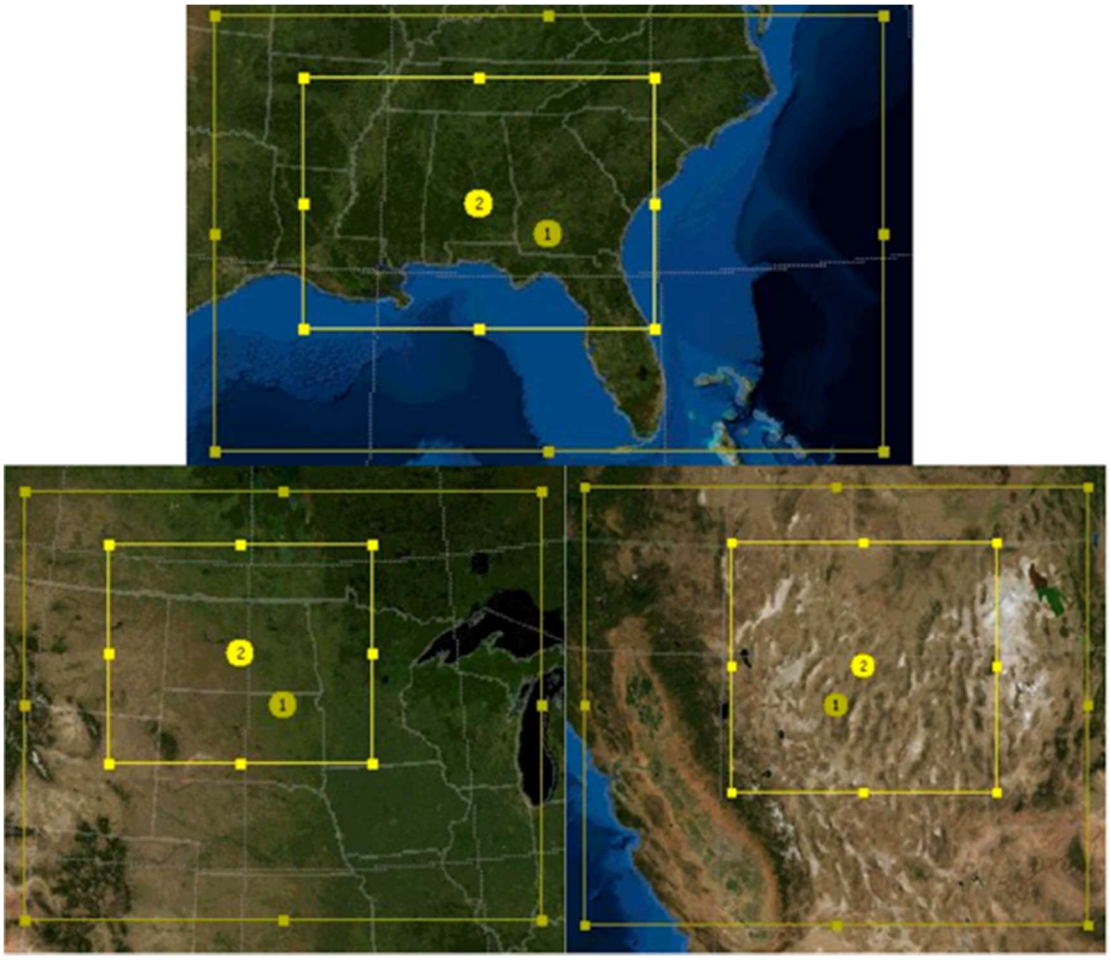

Figure 9. WRF nested domains for the Southeast (top), Northern Plains (bottom left), and West (bottom right). The outer (inner) domain for each location was 10 (2) km resolution with each domain center denoted in yellow as 1 (2), respectively.

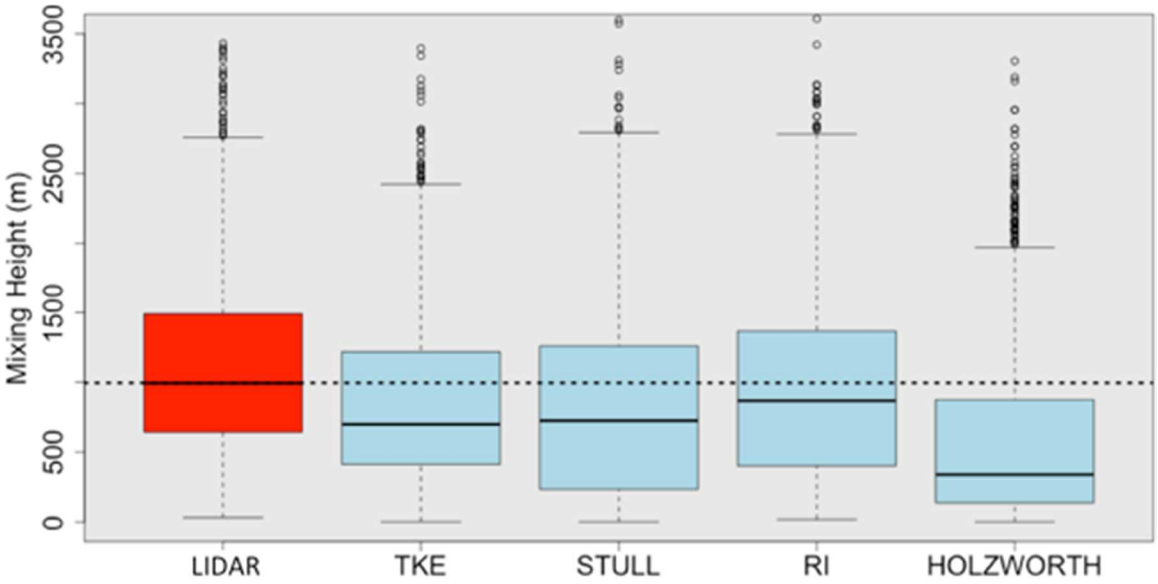

Figure 10. Boxplot diagrams of mixing height values derived from lidar (red) and RUC2 data for TKE, Stull, RI, and Holzworth (light blue, respectively). The black horizontal dashed line highlights the median height for lidar in relation to the four methods. Collocation sample size is 2,151.

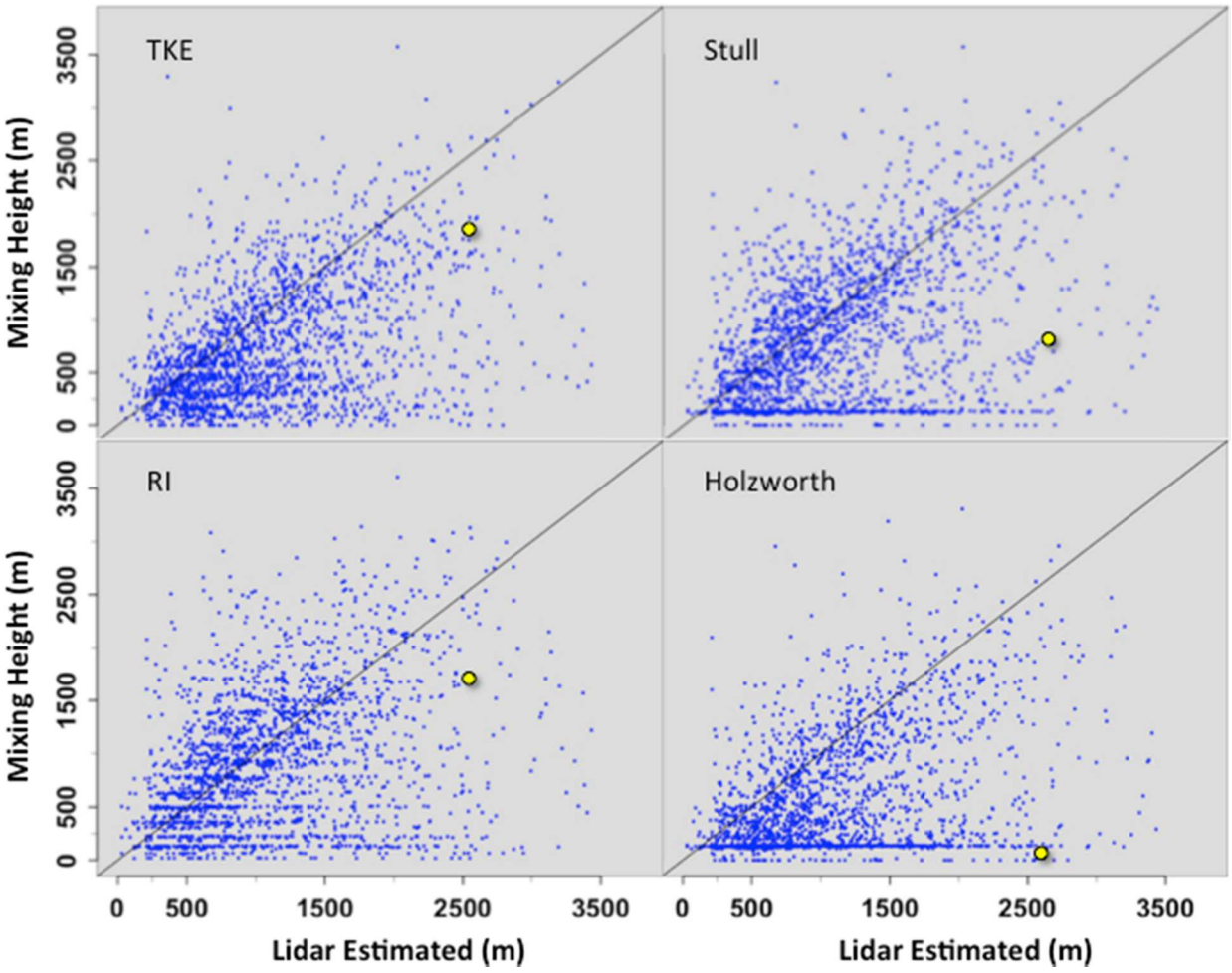

Figure 11a. Four panel scatter diagrams depicting mixing height values computed from RUC2 for each method versus lidar derived height. The yellow highlighted points are discussed in Fig 11b. Collocation sample size is 2,151.

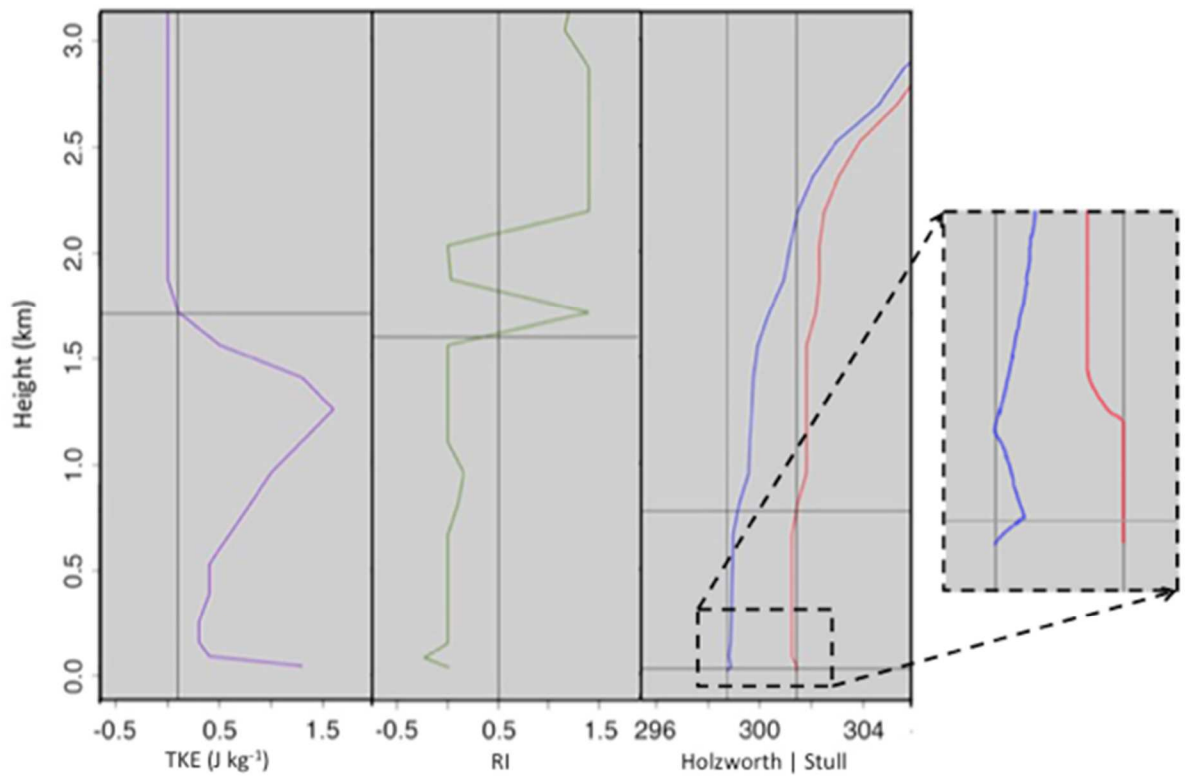

Figure 11b. The vertical profiles of the yellow highlighted points in Fig. 11a are shown over a 3 km depth for the TKE, RI, and combined Holzworth | Stull (blue | red lines; dry | virtual potential temperature) methods left to right, respectively. Thin vertical (horizontal) black lines designate method threshold values or the surface parcel temperature (define the mixing height levels). For the combined Holzworth | Stull panel, mixing height levels (horizontal lines) are the bottom | top, respectively. The subtle near-surface inversion for the Holzworth method is shown in the blow-up panel (right hand side) and marked by black dashed lines/arrows.

Figure 12. Map of absolute mixing height difference, combined mean height (for Stull, TKE, and RI) from RUC2 minus coincident lidar height. Red (black) dots indicate values of 500 m or greater (less), respectively.

Figure 13. Map of absolute mixing height difference across methods (for TKE, RI, and Stull) from RUC2 (lidar excluded). Red (black) dots indicate differences above (below) 500 m, respectively. The three yellow dots demark case example locations to be examined for the Southeast, Northern Plains, and Western US (east to west), respectively.

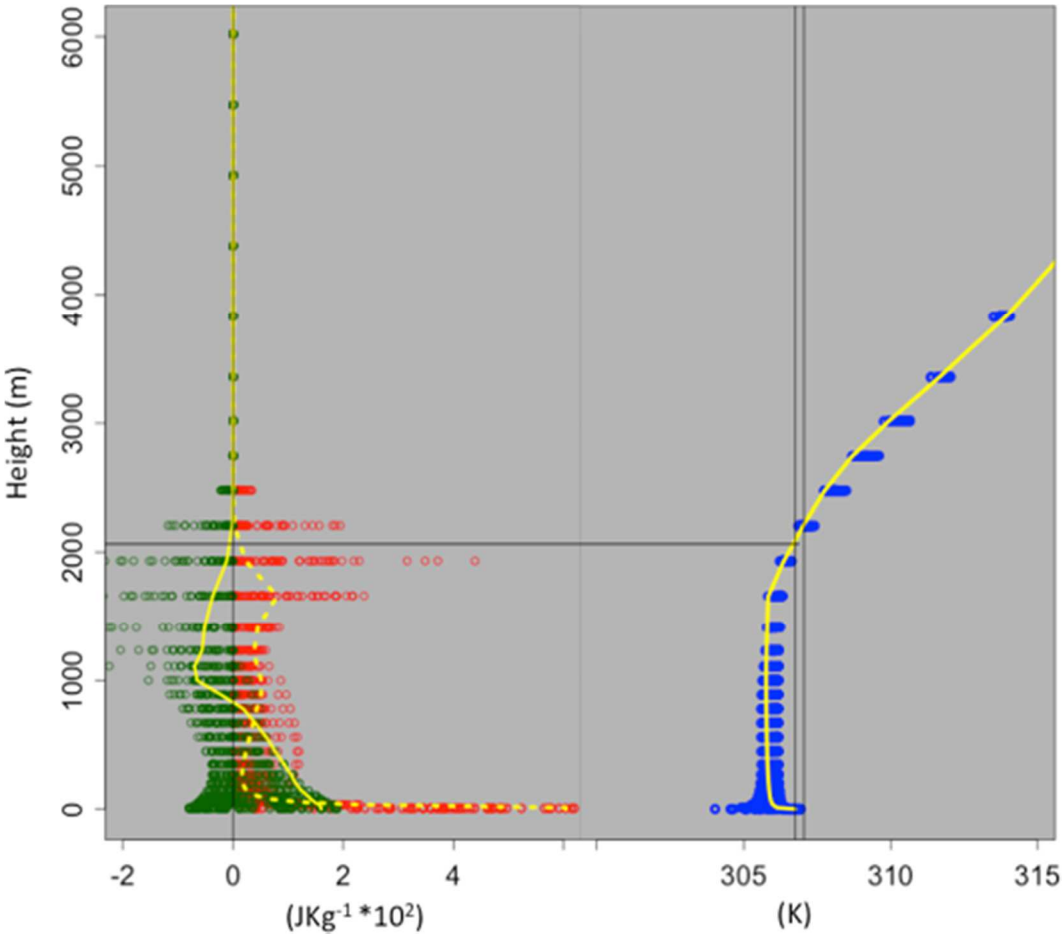

Figure 14. Illustration of TKE-buoyancy (red), TKE-shear (green), and virtual potential temperature (blue) profiles left and right panels, respectively, for 1705 - 0000 UTC at five minute intervals for the Southeast location. Yellow curves represent the 1900 UTC lidar sample time and corresponding profiles for TKE-buoyancy (dashed), TKE-shear (solid), and virtual potential temperature (solid) left and right panels, respectively. The black vertical lines in the right panel highlight the surface parcel upward displacement for the maximum and 1900 UTC.

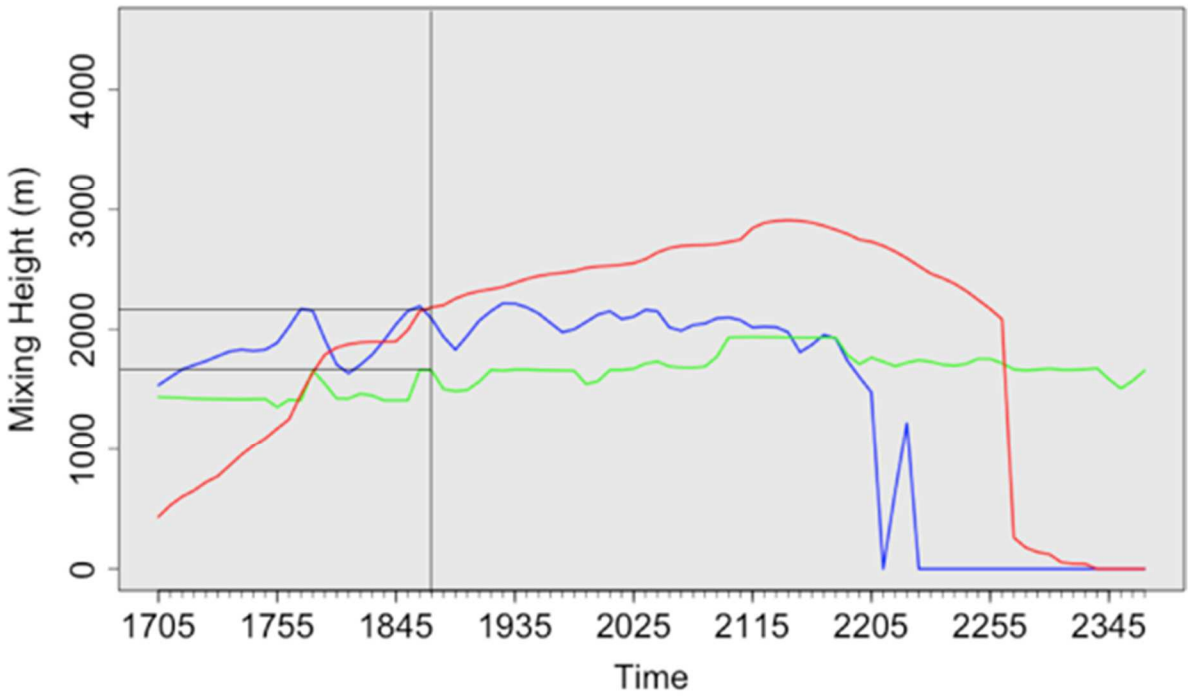

Figure 15. Mixing height values through time for TKE (red), Stull (blue) and RI (green) from WRF 2 km for the Southeast US location. Temporal resolution is every five minutes 1705 – 0000 UTC. Vertical and horizontal black lines highlight the 1900 UTC lidar sample time (consistent with the yellow curves in Figure 14) and mixing height location, respectively.

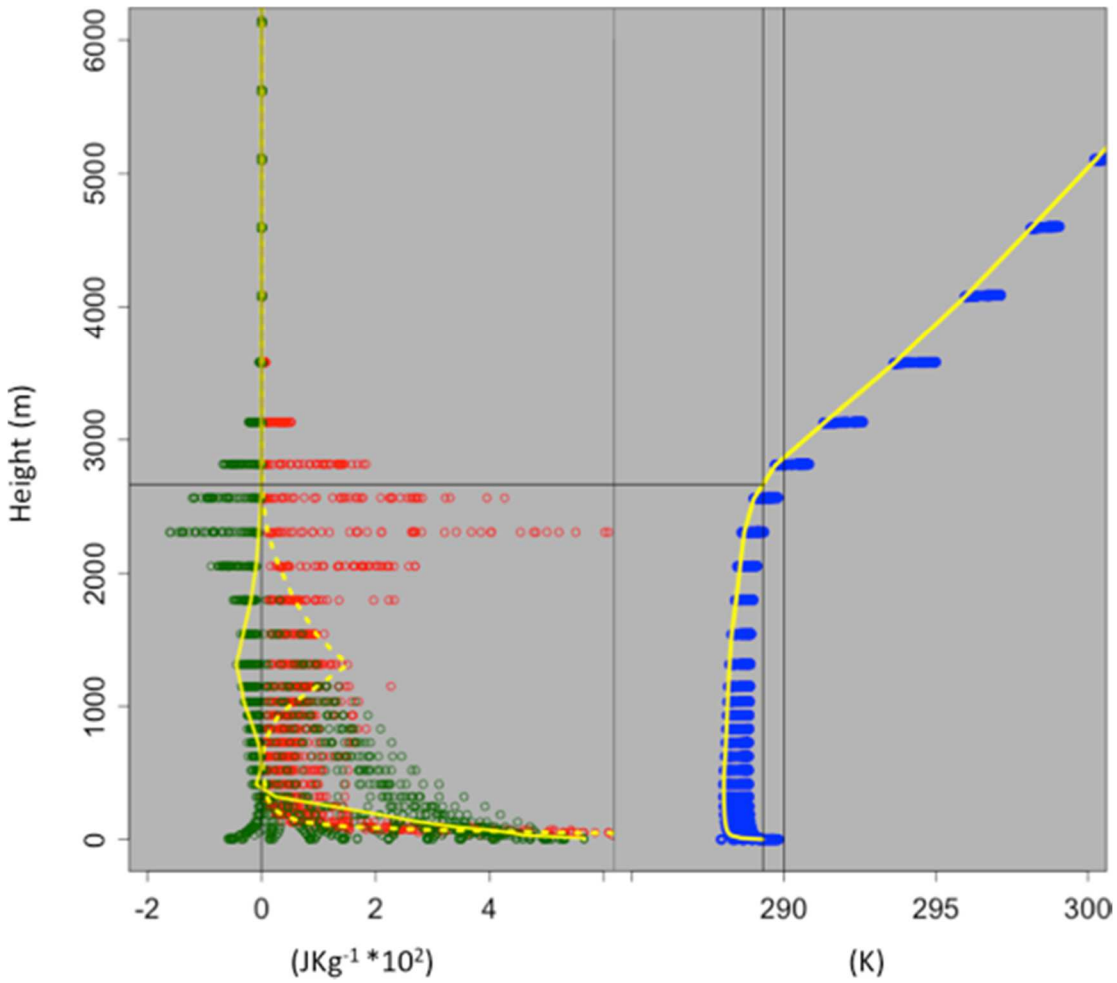

Figure 16. Same as Figure 14 except for the Northern Plains location where the yellow curves identify the 2000 UTC lidar sample time.

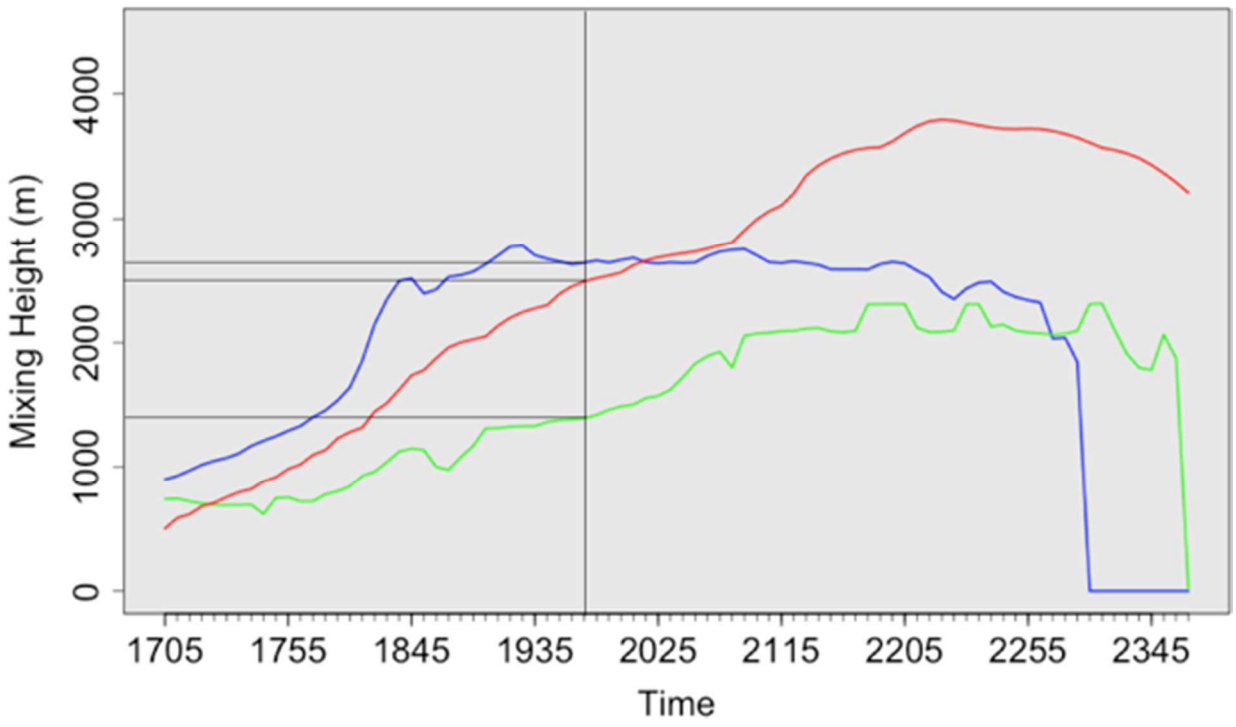

Figure 17. Same as Figure 15 except for the Northern Plains location where the black vertical line corresponds to a 2000 UTC lidar sample time.

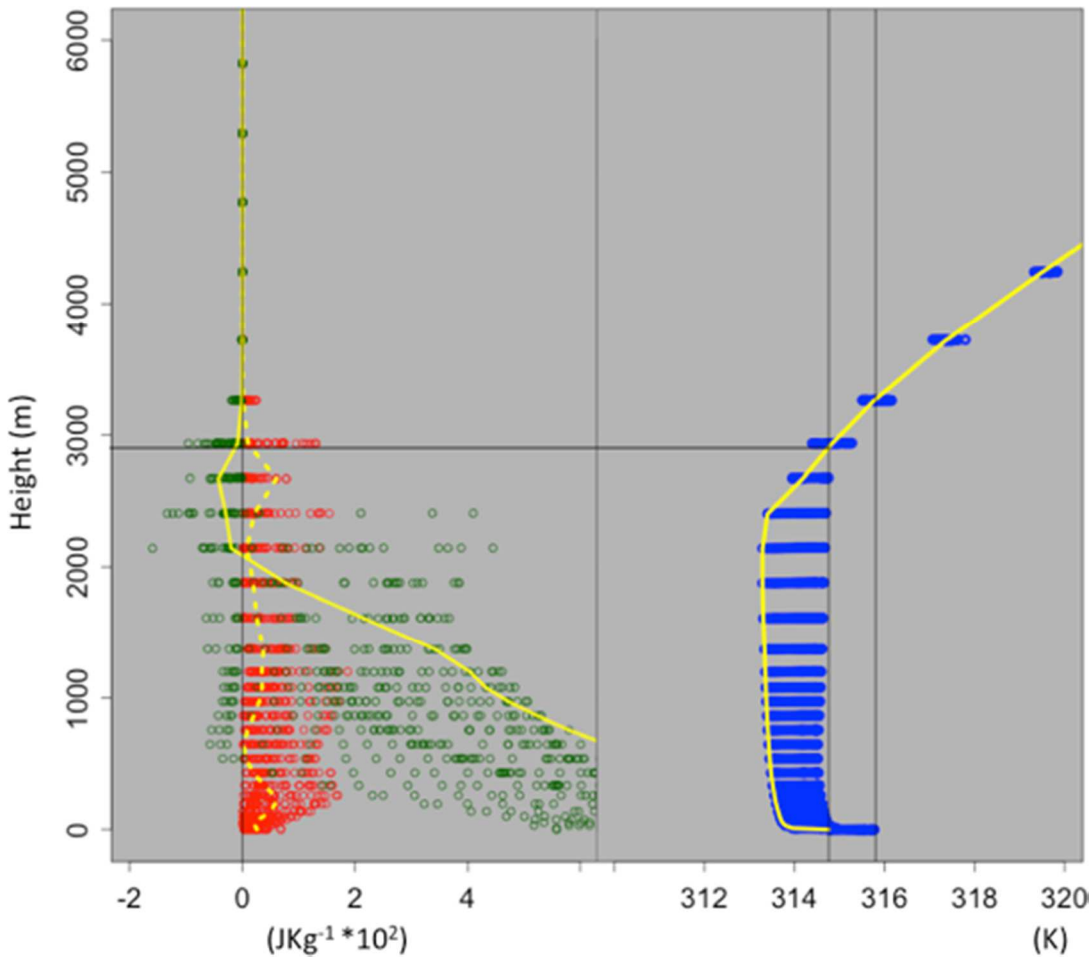

Figure 18. Same as Figure 14 except for the Western US location where yellow curves identify the 2100 UTC lidar sample time.

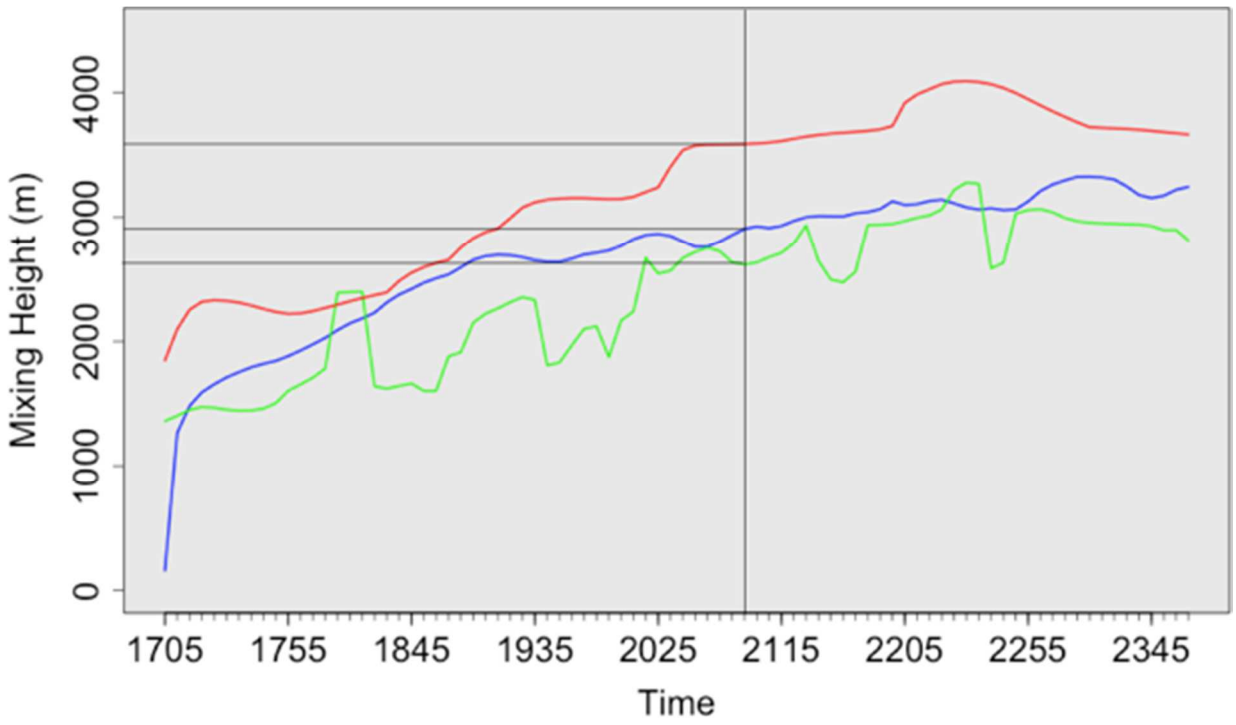

Figure 19. Same as Figure 15 except for the Western US location. Back vertical line demarks the 2100 UTC lidar sample time.

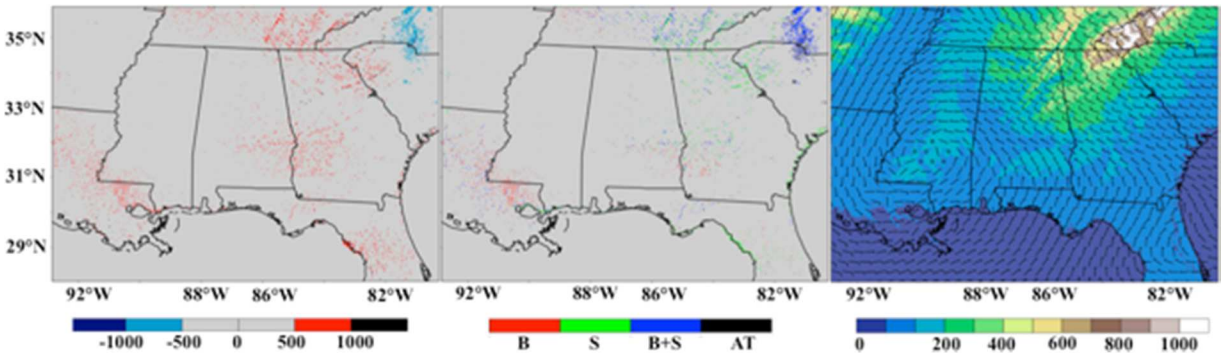

Figure 20. Maps of TKE-Stull height differences (left), spatial perturbations (center), and terrain overlain by the low-level flow field (850 mb wind in knots) for the Southeast U.S. 2 km WRF domain. Height differences and terrain units are in meters. Perturbation occurrence is represented by color for B – buoyancy (red); S – shear (green); B+S – buoyancy and shear (blue); and AT – advection and or terrain inducement.

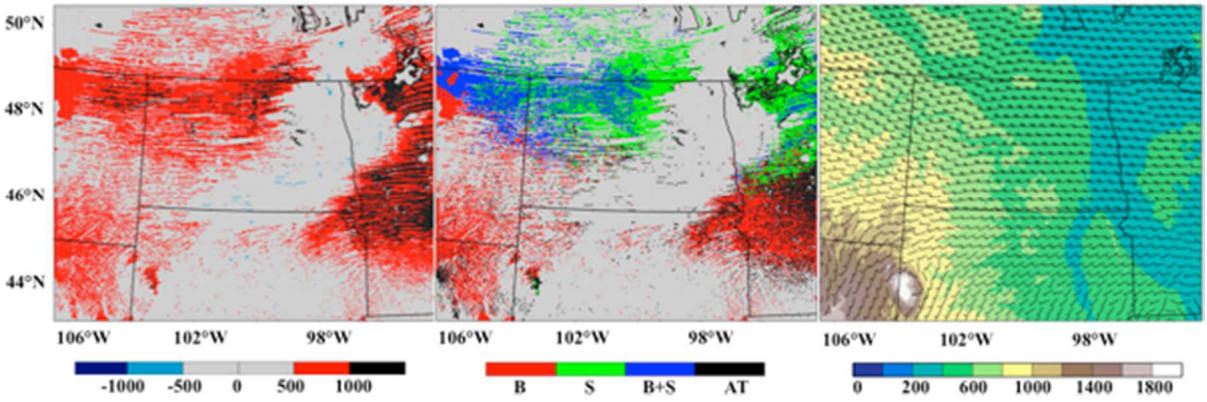

Figure 21. Same as Fig. 20 except for the Northern Plains domain.

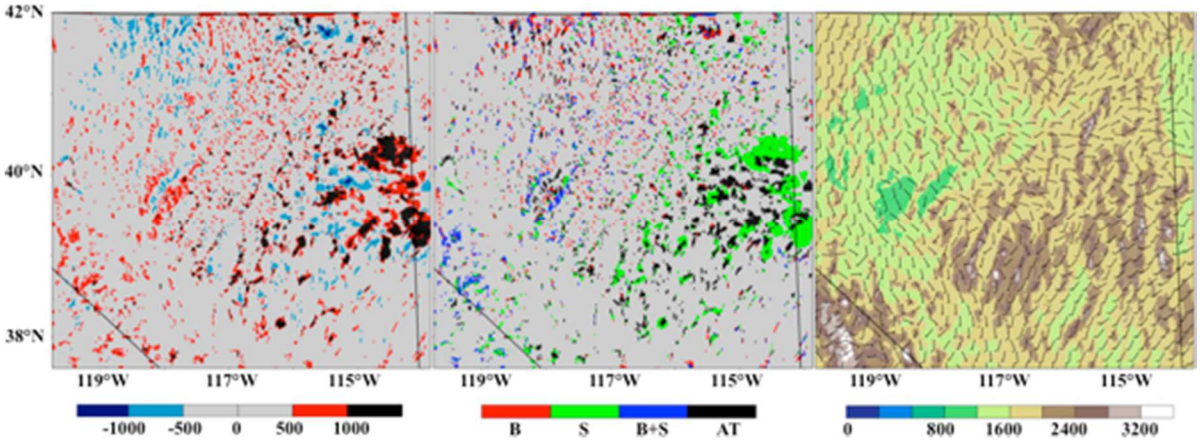

Figure 22. Same as Fig. 20 except for the Western U.S. domain with the 700 mb level representing the flow field (right).

Paper two

Hurricane Sandy (2012). Part I: The tropical-extratropical environment preceding incipient development

Matthew G. Fearon[1], Michael L. Kaplan[1], and John F. Mejia[1]

Journal of Geophysical Research - Atmospheres

---

[1]Desert Research Institute, Reno, Nevada, USA.

Corresponding Author: Matthew G. Fearon, Division of Atmospheric Sciences, Desert Research Institute, Reno, NV 89512, E-mail: matthew.fearon@dri.edu

Key Points. Precursor hurricane environment, tropical-extratropical interaction, hemispheric mass adjustments, Arctic Oscillation, equator-to-pole mass imbalance

Abstract. Large impact storm events like Hurricane Sandy (October 2012) are commonly re-analyzed during their developmental or mature stages. The state of the atmosphere preceding the storm (days to weeks) is commonly overlooked as a contributing factor in the developmental process. In this study, the preceding environment of Hurricane Sandy is reexamined. Results are presented in the form of two papers. Part one, presented herein, documents the planetary-scale adjustments that occurred prior and leading up to Hurricane Sandy's incipient development (the setup period of 1-22 October 2012) and their role on the westward progression of the pre-Sandy disturbance. Coincident amplification in the Arctic, North-Atlantic, and Madden-Julian Oscillations (with an approximate 1-2 day lag) is shown to correspond with vigorous meridional transport and mass exchange across the Northern Hemisphere (equator-to-pole). The meridional exchange is also shown to be influential on the precursor environment surrounding the pre-Sandy disturbance. In a second companion paper, the downscale impact of the hemispheric exchanges discussed in part one are viewed at the meso-beta and gamma scales of motion over Sandy's genesis region, namely the southwestern Caribbean. The terrain-induced processes, particularly in the vicinity of Costa Rica, Panama, and Colombia, are analyzed for their role in the organization of rapid intensification during the period of 22-25 October.

1. Introduction

The transient nature of the atmosphere during autumn often lends to the interaction of tropical and extratropical weather systems. Atlantic hurricanes and tropical storms that form during the months of October and November can become a representative junction point for such interaction when their warm, moist core is met by anomalously cool air penetrating equatorward. A successful merger occurs when a new storm system of hybrid characteristics emerges and deepens as it continues poleward. A stunning case example of this was revealed with the extratropical transition of Hurricane Sandy during 26-29 October 2012.

Some of the first documented analyses on the topic of tropical-extratropical interaction can be traced back to the Rossby School, including the works of Riehl (1945), Starr (1948), Rossby and Starr (1949), Palmén (1949), Yeh (1950), Palmén (1951), and Riehl et al. (1951). And even though each contribution examined the topic from a unique

perspective, the primary emphasis was on hemispheric exchange of momentum and the maintenance of thermal equilibrium by way of transient eddies or the meridional circulation, including the associated north-to-south artery of the subtropical trades. Palmén et al. (1958) carried these concepts further through an analytical computation of kinetic energy release from Hurricane Hazel (October 1954) as it transitioned into an extratropical cyclone over the southeastern U.S.

Not unlike Palmén's analysis, the majority of large hybrid-type storms are often reanalyzed to establish a deeper understanding of the atmospheric interaction across scales of motion (Harr et al. 2000; Harr et al. 2000; Jones et al. 2003). However, reanalysis of these storm events, including the case of Hurricane Sandy, are typically carried out from the beginning of their extratropical transition phase, with emphasis placed on storm-transition dynamics and predictability (e.g., in the case of Sandy, Galarneau et al. 2013; Munsell and Zhang 2014; Torn et al. 2014; Lackmann 2015). While Sandy's extratropical transition phase has received much attention, some literature on the tropical genesis period does exist, namely Shen et al. (2013) and Lussier et al. (2015).

Shen et al. (2013) examined storm formation predictability during the period of 18-22 October with a 9 km global mesoscale model for different initialization times compared to the National Hurricane Center (NHC) Best Track information and select fields from European Centre for Medium-Range Weather Forecasting (ECMWF) Re-Analysis (ERA) Interim. Results demonstrated that model initialization with greater lead times improved storm predictability and track forecasts. Multi-scale precursors upstream from the Caribbean zone wherein Sandy developed, such as a low-level westerly jet over the northeastern Pacific Ocean and an encroaching upper-level trough over the western Gulf of Mexico, were

discussed and linked to the rising branch of the Madden-Julian Oscillation (MJO; also discussed in Blake et al. 2013). Lussier et al. (2015) evaluated the evolution of the precursor Sandy disturbance (and its vorticity accretion) in the context of the marisupal paradigm (Dunkerton et al. 2009) for the 10-23 October period. Emphasis was placed on vorticity accretion into the incipient wave and potential vorticity sources in the environment, such as that from persistent open-ocean convection along with filaments produced off the Hispaniola coast and those entrained from Inter-Tropical Convergence Zone (ITCZ).

These studies provide insight on Sandy's origin and lifecycle. However, often preceding such large storm events, evidence of a setup environment (preconditioned over a timescale of several days) can be found. In general and in the case of Hurricane Sandy, the specific nature and scale of the dynamical adjustments associated with a precursor environment remain understudied yet they reveal important details on why complex tropical and extratropical dynamics are able to phase and spawn concentrated highly-intense storm development. In the case of Hurricane Sandy, preceding planetary-scale adjustments, orchestrated by an extended period of extratropical-tropical interaction, produced such an environment. The translation of these larger-scale adjustments to the mesoscale, in particular those that occurred over the Caribbean zone in association with the local orography, played a critical role in Sandy's incipient development. And while Shen et al. (2013) and Lussier et al. (2015) highlight some of these contributing factors, respectively, the organization and the specific pathways of the precursor dynamics remain undocumented.

The objective of this study is to investigate the origin of these precursor dynamics. Results are presented in the form of two papers. First, in this paper (hereafter referred to as part one), the planetary-scale adjustments that occurred prior and leading up to Hurricane

Sandy's incipient development (the setup period of 1-22 October) are analyzed. The meridional transport and mass exchange initiation over the northern hemisphere (equator-to-pole) during this period revealed extraordinary tropical-extratropical interaction— a signal well captured in Arctic Oscillation Index (AOI) and its sub-counterpart the North Atlantic Oscillation Index (NAOI). In a second companion paper (hereafter referred to as part two), the downscale impact of the hemispheric exchanges discussed in part one are viewed at the meso-beta and gamma scales of motion over Sandy's genesis region, namely the southwestern Caribbean. The terrain-induced processes, particularly in the vicinity of Costa Rica, Panama, and Colombia, and the convergence of the resultant low-level vorticity, in conjunction with the formation/enhancement of multiple jet structures, is evaluated. The organization and contribution of these features were found to be influential in Sandy's rapid intensification during the period of 22-25 October.

This part one analysis relies on many concepts documented in the literature with respect to tropical-extratropical interaction, although no one particular dynamical mechanism is emphasized. Rather, areas of mass exchange initiation are examined for their respective location in the context of the hemispheric mass balance and as they may relate to atmospheric modes. The authors refer the reader to Roundy (2011) for a comprehensive review of the topic (and dynamics) of tropical-extratropical interaction. Other related literature on tropical-subtropical cold-surge intrusions and the initiation of mesoscale features in association with topography are relevant in the case of Sandy's incipient and rapid development, however, these studies are reserved for consideration in part two.

The remainder of this manuscript (part one) is comprised of four additional sections. Section two provides an overview of the study area and Hurricane Sandy's path. Section

three describes the data and analysis procedure used in part one. Discussion and analysis are presented in section four on the planetary-scale adjustments preceding Sandy's incipient development during the period of 1-22 October. Section five is reserved for summary and concluding remarks.

2. Study area and overview of Sandy's path

The origin of Sandy was first documented as an easterly wave that departed the African coast on 11 October (Blake et al. 2013). However, analysis by Lussier et al. (2015) found that the precursor disturbance emerged independent of the easterly wave in response to a breakdown in the ITCZ on 10 October over the North Atlantic Basin near 8°N/37°W. Figure 1 illustrates Sandy's lifecycle trajectory where NHC Best Track locations of tropical depression/storm status are indicated by the orange line (October 21/18UTC – 24/06UTC and October 27/00-12UTC south-to-north, respectively); hurricane in red (October 24/06UTC – 29/18UTC); extratropical in blue (October 29/18UTC – 31/12UTC). The estimated precursor disturbance pathway is depicted by the yellow line (October 10/00UTC – 21/18UTC) where overlain black "L" symbols indicate coordinates obtained from the analysis of Lussier et al. (2015) with the origin symbol in red (October 10/00UTC). As mentioned in the introduction, Sandy's trajectory north of Cuba was the focus of several other research contributions (e.g., Galarneau et al. 2013; Munsell and Zhang 2014; Torn et al. 2014; Lackmann 2015), and based on their results, a more accurate depiction of storm status (line color in Fig. 1) would reveal the onset of extratropical characteristics near the south Florida coast.

In this study (part one), the estimated precursor disturbance trajectory (the yellow line; Fig. 1) and the influential planetary-scale adjustment sequences are the central focus.

These adjustments were found to occur over the entire Northern Hemisphere, although only the primary signals are discussed. The red rectangular box depicted within the southwestern Caribbean (Fig. 1) highlights the prime location of Sandy's tropical development and where organization of the peripheral terrain-induced mesoscale features took place (discussed in part two). For an in-depth overview and chronology of Sandy's entire trajectory, the reader is referred to the analysis of Blake et al. (2013).

3. Data and methodology

The analysis of planetary-scale adjustments presented in section 4 utilized pressure-level data from 6-hourly ERA Interim for the period 1-22 October 2012. Fields of relative vorticity, geopotential height, temperature, and horizontal winds, including computed mass flux and height anomalies (associated with a 30-year ERA Interim climatology 1985-2014) were examined. The ERA Interim data (archive Version 1.0; Dee et al. 2011) used were formatted on a global Gaussian grid (~75 km horizontal resolution; 241x480; latitude x longitude) with 23 vertical pressure levels. The reanalysis data assimilation procedure incorporates a series of observational data, in particular a more robust inclusion of satellite radiance profile information as compared to other reanalysis datasets.

A host of other complementary data sources and methods were used to facilitate this analysis. Geographical locations from the NHC Best Track compilation were used, along with precursor-disturbance coordinates adapted from the analysis of Lussier et al. (2015). The daily variability of the AOI and NAOI as computed by the National Oceanic and Atmospheric Administration's Climate Prediction Center (NOAA CPC, 2015) were used as supportive evidence alongside coincident 700 hPa geopotential height analysis and blocking

patterns (algorithm from Tibaldi and Molteni 1990). In conjunction, the daily variability of lower stratospheric temperature[8], sea surface temperature (from NOAA's high-resolution-blended analyses; described in Reynolds et al. 2007), and the Real-Time Multivariate MJO (RTM) Index (Wheeler and Hendon 2004; NOAA CPC 2015) were also studied. And even though the El Niño Southern Oscillation (ENSO) index was examined, persistent near-neutral conditions were observed (NOAA CPC 2015) ahead of and during Hurricane Sandy.

4. Analysis and discussion

The following analysis is presented and organized as a categorical description of planetary-scale adjustments (or sequences) that influenced Hurricane Sandy's early trajectory (yellow line in Fig. 1) over the period of October 1-22 and ultimately preconditioned the local mesoscale environment over the southwestern Caribbean. As part of the primary analysis of 700 hPa geopotential height anomalies, and corresponding fields of positive relative vorticity and wind (including vertical wind shear), the daily modes of AOI, NAOI, and MJO were examined along with blocking patterns in the height field and computed mass flux. The following discussion also serves as lead in to part two of this study.

a) Meridional mass exchange

During October 1-10, a series of cold troughs from the continental high latitudes penetrated equatorward and intensified the zonal geopotential height gradient at numerous locations along 30°N (or along the mid-latitude / subtropical interface). In response, the subtropics received (expelled) mass from the north (south) behind (ahead) of each cold

[8] Downward propagation of stratospheric warming has been found to modulate the Arctic Oscillation (Baldwin and Dunkerton 1999; Ripesi et al. 2012).

intrusion. The northbound transport of mass[9] over the Northern Hemisphere was examined qualitatively with the daily 700 hPa geopotential height anomalies (Fig. 2) and computed meridional mass flux (ρv, $kgm^{-2}s^{-1}$) along 25 and 60°N (Fig. 3) for the 10-day period. Analysis (west-to-east; Fig. 2) revealed three distinct geographical zones of southbound (northbound) trough (ridge) couplets. First, on October 1-4, a trough from northeastern Russia pressed southeastward across the North Pacific and amplified an existing ridge centered over the Gulf of Alaska. Northwestward amplification of this ridge also occurred on October 6-10 in response to mass influx from the tropics carried north-northeastward by the western Pacific subtropical ridge near 30°N/150°E (Fig. 2; and Fig. 3, top and bottom panel, positive flux along 150°W and 150°E, respectively). Second, on October 1-6, two troughs from North America and Greenland progressed across the North Atlantic and Europe, respectively (Fig. 2). The North American-based trough moved slower while the southeastward penetration of the Greenland-based trough prompted a south-to-north surge of warm air from the Sahara desert into the Arctic (across 35-90°N and along 40-50°E). Another pulse of warm air from the Sahara and Saudi Arabian deserts entered the Arctic on October 8-10th (across 30-90°N and along 60°E; Fig. 2; and Fig. 3, top panel, positive flux along 60°E) when the Greenland-based trough re-intensified over eastern Europe. A third trough from Scandinavia, on October 1-6, reinforced northbound mass transport (upstream and downstream) as it progressed slowly across central Asia (Fig. 2). A deep, broad area of anomalously positive geopotential height (greater +180 m) overstretched the pole and the majority of the Arctic on October 10th, excluding the zone adjacent to North America and Greenland (Fig. 2).

[9] A 700 hPa geopotential height anomaly of 100 m above (below) the 30-year climatological average was used to represent a substantial mass increase (decrease) within the vertical column, which corresponds approximately to a positive (negative) mass flux value equal to or greater (less) than 4 $kgm^{-2}s^{-1}$.

The former three cold-intrusion sequences were influential to the meridional mass exchange between the pole and the subtropics during October 1-10. Although subtropical-tropical activity was an important contributor in the exchange, whether it was convection over the southwestern Pacific; desert heating over the Sahara and the Middle East; or residual heating from southeastern Asia, respectively. Similar yet increasingly intense adjustment sequences occurred in succession during the remainder of October. The timing and north-south extent of these surges were representative and consistent with the negative signal in the daily AOI. Figure 4a illustrates the month long AOI signal, including the last few days of September. Note the sharp positive to negative reversal in the signal on October 1st followed by a brief (relatively modest) negative spike on October 4th. Subsequent negative spikes (and their respective minimums) arose on the 12th, 17th, and 24th (to be discussed).

The periodicity of other indices was found to be coincident (in time and space) with the former adjustments, such as the NAOI (Fig. 4b) and the MJO Amplitude Index (or MJOAI; Fig. 4c). The NAOI signal on October 2-5 was consistent with the amplified Greenland-based trough-ridge dipole along a southeast-to-northwest axis between 0-60°W (see Fig. 2, October 4th). The MJOAI signal revealed intensification preceding the adjustments (as early as September 27th), indicative of a time-lagged relationship. As mentioned above in proximity to the first adjustment location over the western Pacific, mid-to-upper level mass from the tropics, generated from several mesoscale convective complexes and a tropical storm (#21 - Gaemi, 2012) southwest of 30°N/150°E, was carried north-northeastward by the western Pacific subtropical ridge. The northward transport of the mass appeared to be a function of co-dependence between the subtropical ridge and another mid-latitude trough departing the Russian coast (Fig. 2, October 7th; Fig. 3, top and bottom panel,

positive flux along 150°W and 150°E, respectively). Eventually, the mass merged with the existing height anomaly downstream over the Gulf of Alaska.

As one might expect under a dominant meridional flow regime, zonal flow blocking was also observed in association with the former adjustments. Figure 5 presents a computed measure of the blocking strength along the 60°N latitude band (Tibaldi and Molteni 1990). Inspection west-to-east over the 10-day period indicates correspondence with the three distinct trough-ridge couplets discussed above. First, the Gulf of Alaska ridge and its westward amplification was found to be a persistent feature over the 10-day period along 120-180°W. Second, not discussed above, on/off blocking was noted along 60°W (upstream and downstream) and appears to be a reflection of the semi-permanent (negatively tilted) North American Subtropical High (NASH; see Fig 2, October 2-4; and Fig. 3, top panel, positive flux along 60°W). Third, modest blocking between 0-60°E during October 1-8 was representative of the northbound mass surge ahead of the Greenland-based trough. Fourth, the on/off blocking along 120°E appeared tied to pre-existing high heights over central Asia reinforced by the migration of the Scandinavian-based trough.

b) Sandy's origin

While each former adjustments prompted vigorous meridional flow across 30-90°N, zonal flow (as low-level easterlies) was also revitalized over the tropics. With respect to Hurricane Sandy's origin, the double-trough intrusion (from North America and Greenland; Fig. 2, October 4-7) also amplified the north-south pressure gradient across central Africa and the North Atlantic Basin. Note the sequential enhancement of the zonal wind field along the east-to-west transect between 5-20°N / 0-50°W (red wind barbs; Fig. 6, bottom-to-top).

Clusters of convection arose from flow convergence between the enhanced easterly jet and the southern hemisphere (cross equatorial) trades along the African west shore (~ 5-15°N; Fig. 6) and downstream (further west). The overlain vorticity pattern reveals disturbances along the African coast near 0-10°N / 0-10°E and 2-12°N / 10-30°W and downstream (Fig. 6). Enhancement of the jet appears to have re-established the ITCZ, as illuminated by the light-to-moderate ribbon of positive relative vorticity (Fig. 6, middle panel). As the leading edge of the vorticity ribbon neared the north Brazilian coast (~10°N, 50°W), easterly flow was again met by cross-equatorial southeasterlies on October 10th (Fig. 6, top panel). Tropical depression Rafael intensified in this convergence zone, and in its wake as part of the same vorticity ribbon, the pre-Sandy disturbance emerged (Fig. 6, top panel).

c) Equator-to-pole mass imbalance and redistribution

While Rafael slowly intensified along a southeast-to-northwest transect, from north of South America to just west of the Lesser Antilles on October 10-12, more subtropical air continued to enter the Arctic. Each pulse was channeled through a west-to-east mid-latitude-trough / subtropical-ridge gradient (e.g., central North Atlantic; Fig. 7, October 11-12), or was a re-amplification of pre-existing high-latitude (positive) height anomalies. Mass surges associated with the latter recurred near the same three geographical zones as described above, northeastern Russia; the North Atlantic and Europe; and central Asia. Except over North America, an extreme (positive) geopotential height anomaly now blocked and surrounded the entire pole circumference (north of 75°N; Fig. 7, October 12th). The timing of this peak equator-to-pole mass imbalance was coincident with a negative (minimum) in the AO signal (Fig. 4a; October 12th).

Over the next several days, once blocked zonal avenues across North America and the North Atlantic were freed temporarily. Note the zero to minimal blocking from ~ 122°W to 60°E (Fig. 5, October 12-16th) and thereafter from ~122°W to 0° (Fig. 5, October 12-20th). A series of the troughs (from the Alaska/Yukon and the Pacific) moved east-southeastward across this zone (Fig. 7). It is hypothesized that the mass exodus from Alaska/Yukon was a stimulus for the positive height anomaly (blocking the remainder of the Arctic) to redistribute additional mass, as a recurrence in meridional exchange occurred in succession on October 17th coincident with AOI and NAOI minimums (Fig. 4a and b) and the re-excitation of the MJOAI (Fig. 4c). A portion of the Arctic height anomaly moved southward and dispersed across the Asian continent while another piece remained north, but moved eastward (clockwise) around the pole filling the void left north of Alaska. The height anomaly time-lapse in Fig. 7 from October 13-23 provides an illustration of this theory.

d) Hurricane Rafael's contribution and Sandy's Caribbean entrance

Coincident with the former, but further south on October 12th, tropical storm Rafael had just crossed the southern extent of the Lesser Antilles and slowed temporarily (Avila 2013). The storm deepened into a hurricane north of the Greater Antilles on the 13th just south of an area of deformation produced by an upstream trough exiting the southeastern United States and a downstream ridge (i.e., the northward retreating NASH). Anticyclonic flow resided over the Gulf of Mexico (to the southwest) as Hurricane Rafael approached from the southeast (Fig. 7, October 14th, ~ near 25°N/65°W). The northern extent of the deformation zone instilled a south-to-north transect of low shear wherein Rafael intensified and tracked (Fig. 8, October 13-16). The U.S.-based trough and Hurricane Rafael eventually phased (Fig.

7, October 16-17) and then merged with another trough deepening over western Europe on October 20th (Fig. 7).

The deformation zone produced ahead of Rafael, including the subsequent wake left by the storm, was found to be important to Sandy's fate. Specifically, as Rafael developed and tracked northward, the area of deformation broadened west-to-east temporarily and extended southward (Fig. 8). This revealed a scenario in which the predecessor storm (Rafael) co-produced a more favorable environment for the successor storm (Sandy). And although deep vertical shear increased southward along the Lesser Antilles (Fig. 8, October 17-18) coincident with Sandy's eastern Caribbean entrance (Blake et al. 2013), computation of vertical shear over a reduced depth (850-500 versus 850-200 mb; see Fig. 9; Rhome et al. 2006), which is consistent with a more shallow (less mature) disturbance, revealed a much wider zone of low shear.

Hurricane Rafael also played an important role in the redistribution of the Arctic mass (Fig. 7) and the eventual northwestern Atlantic block that steered a mature Sandy westward (Fig. 5, ~60°E to 60°W, October 23-29). As Rafael transitioned to extratropical on 18th, and re-intensified on 20-23 over the northeastern Atlantic (Fig. 7; 45°N/30°W), it was blocked by a northward retreating NASH to the west and an intensifying Saharan ridge to the east (Fig. 5 and 7, October 18). The stationary deepening over the eastern North Atlantic promoted a northwestward migration of the Saharan mass (the temporary eastern block). Eventually, the Saharan mass wrapped completely around extratropical Rafael (west-to-north then south) and assumed a connection to the northwestern Atlantic blocking feature / Arctic mass buildup (Fig. 7, October 23).

f) The mesoscale environment left over southwestern Caribbean

As the pre-Sandy disturbance crossed the Lesser Antilles and entered the Caribbean on October 18th, through the deformation (and low shear) wake left by Hurricane Rafael, a series of mid-latitude troughs moved across the U.S. (from Alaska/Yukon) northwest-to-southeast. As described earlier, these mass departures from the Arctic occurred coincident with reduced zonal blocking across North America and were replaced by the extensive positive height anomaly from the eastern hemisphere, circumnavigating the pole (Fig. 7, October 12-23). The last trough in the series (October 19-21) was perhaps the most intense as, compared to its predecessors, its southern extent reached deep into Gulf of Mexico and promoted low-level mass perturbations, identified by rises (bulges) in the 975 hPa geopotential field (Fig. 10a; red contour), along the eastern high terrain of Honduras, Nicaragua, and Costa Rica. These low-level features were a response of the upper-level convergence that ensued behind the trough. Initially, a phased polar and subtropical jet accompanied the system as it entered the Gulf of Mexico, although sharp ridge amplification on the backside caused the subtropical stream to detach, buckle, and dive southward in the form of an ageostrophic jetlet over the central Gulf (see sequences in Fig. 10b).

The southward progression of the former low-level mass perturbations, including their along-mountain trajectory, further presented themselves as a series of Kelvin-edge waves. A low-level mesoscale jet (from the west) away from the Costa Rica Mountains was the downstream consequence. This feature (also an environmental vorticity source) represents one of three low-level jet contributions (to Sandy's rapid development) to be discussed in part two of this study.

The two additional contributions to be discussed in part two arise from easterly and southerly flow caused by deepening surface pressure over the central Caribbean (associated with Sandy). Low-level easterly momentum from the North Atlantic was re-routed in the form of a mesoscale jet after it encountered the high terrain along northeast Colombia and Venezuela. The third mesoscale jet emerged from southerly flow over the northeast Pacific, from a convergence zone south of Panama and west of Colombia—a merger of westerly flow, blocked by the Costa Rica Mountains and carried along the southern flank of Panama, and cross-equatorial southerly flow steered eastward by the Coriolis force and persistent convection along Colombia's west shore. Figure 11 highlights the environmental flows consistent with these three mesoscale jet features and provides a illustrative prelude of dynamics to be discussed in part two.

5. Summary and Conclusions

Large impact events like Sandy are almost always re-examined over the course of their lifecycle (from start to finish) or during an interesting sub phase. The period before the disturbance (days to weeks) is commonly overlooked as a contributing factor for development. In the case of Hurricane Sandy, the period before (the preconditioning stage) revealed a fascinating set of adjustments that proved to be influential as part of the multi-scale environmental setup. In the absence of the preliminary adjustments, one might question if the event would have occurred at all or if/how storm intensity would have been affected? Lackmann (2015) explores this question with regard to Hurricane Sandy from an interesting yet different perspective. The study evaluated the impact of historic (year pre-1900) versus future (year post-2090) environmental (climate) constraints on the Sandy's intensity in

relation to the present (observed, 2012) conditions. Although a future (warmer climate) portrayed a significantly more intense storm, the current (observed, 2012) intensity versus what would have occurred historically was not significantly different. This analysis was initiated from Sandy's mid lifecycle and preliminary adjustments that might have occurred in the days leading up to storm genesis (past versus future) were not considered.

The analysis in this paper undertook the complex yet influential temporal period well before, leading up to, and during the pre-Sandy disturbance: October 1-22, 2012. Patterns of planetary geopotential height anomalies were analyzed over the entire Northern Hemisphere, with special consideration given to the preliminary track of the pre-Sandy disturbance over the North Atlantic Basin and Caribbean Sea. Relevant patterns associated with changes in geopotential height were also evaluated, including those for zonal height blocking, wind, north-south mass flux, vertical wind shear, and positive relative vorticity. The daily temporal behavior of well-documented atmospheric modes such as the AOI, NAOI, and MJO were studied at coincident periods and revealed corroborating evidence for the height patterns observed. The behavior/contributions of the atmospheric modes and other influential measures as they occurred prior to and during the pre-Sandy disturbance are listed in Table 1. And although some signals have been well documented in the literature, the combined listing in this context has not been and may be useful for forecasters evaluating the precursor hurricane environment.

Results in this study show that meridional exchange (high/mid-latitude and subtropical/tropical interaction) occurs as way to restore imbalance in either zone. Reasons for the persistent equator-to-pole exchange initiation may be explained by the occurrence of the following, alone or in combination: 1) Cooling over continental high latitudes while

persistent warming remains over the subtropics/tropics (e.g., North America, Scandinavia, Russia landmass cooling versus Mexico-Caribbean, Middle East-Africa, southeastern Asia-Indonesia persistent heating); 2) Persistent or above normal tropical convection and or storm activity; 3) Downward sinking from a sudden stratospheric warming event over the Arctic as an initiator of Arctic imbalance and a precursor of meridional exchange in the troposphere; 4) Sea surface temperature imbalance, perhaps a warmer Arctic ocean with less sea ice promoting meridional polar jetstream behavior.

With regard to continental landmass thermal gradients (1), the October anomalies for 2012 (Fig. 12) were largely more west-to-east rather than north-to-south across the entire Northern Hemisphere. For North America, warm anomalies comprised northern Alaska through central-eastern Canada (including the northeastern U.S. and Greenland) compared to the cool signal across the western-central U.S. For Eurasia, a staggered cool-to-warm signal was present for northwestern Europe compared to the broad (meridional) area of warmth over the Middle East (including northern Africa, eastern Europe, and western Asia). A similar signal occurred over central and eastern Asia, cool and warm, respectively.

Examination of the tropical storm activity in Table 2 reveals an above average year for the Atlantic Basin only (2). However, in terms of hurricanes/typhoons alone, each zone was above normal. In general, storm frequency was less, but storm intensity was greater for those that occurred.

In terms of stratospheric warming over the Arctic (3), a rather strong signal occurred at the beginning of October (see Fig. 13). Warming also transferred downward into the troposphere and remained persistent during the remainder of the month. This occurrence co-aligns (with modest lag, eg, 3-4 days) with a persistent negative AOI signal, where the pole

remains warmer than normal and experienced transient mass gain and loss—consistent with a meridional polar jet stream. And even though much of the Arctic Ocean was frozen during October (Fig. 12), thin longitudinal bands of anomalously warm sea resided just north of Alaska and along northern Eurasia (4). Therefore, the combined effect of stratospheric warming and a warmer than normal sea over the Arctic region may explain the dominant meridional mass exchange—cooperatively supported by the west-to-east thermal gradient over the landmass. In addition, the above normal tropical storm activity in the Atlantic, and the higher intensity of storms overall, may have magnified the north-south thermal gradient in the subtropics against more frequent northwest-to-southeast cold intrusions.

In conclusion, the results presented herein raise a fundamental question: *is it characteristic of late season tropical development to be a response to a period of higher-latitude excitation?* Or expressed in another manner: *can vigorous meridional exchange over an extended period produce a wake zone of minimal kinetic energy wherein residual mesoscale perturbations (and those generated locally) can organize, develop, and re-propagate back upscale*? In this particular study, it does appear that the high-mid latitudes facilitated such an environment over the southwestern Caribbean, a zone semi-protected (and cocooned) from large-scale shear by the surrounding terrain (discussed in part two). Examination of several late-season hurricane case studies as part of future work might prove to be insightful in addressing the former question, particularly cases that developed following vigorous high-mid latitude meridional exchange. As part of such a study, evaluation of the spin-up mechanism (e.g., how rotation is initiated within an easterly wave or clustered convection) and the role of the local environment would be essential aspects.

Acknowledgements. The authors wish to acknowledge John M. Lewis for providing editorial comments and Timothy J. Brown, Desert Research Institute's Program for Climate,

Ecosystem and Fire Applications, for high-performance computing resources. The authors also wish to thank Erin C. Gleason for her support and assistance with graphics.

References

Baldwin, M. P., & Dunkerton, T. J. (1999). Propagation of the Arctic Oscillation from the stratosphere to the troposphere. *Journal of Geophysical Research*, *104*(D24), 30937. http://doi.org/10.1029/1999JD900445

Blake, E. S., Kimberlain, T. B., Berg, R. J., Cangialosi, G. P., & Beven II, J. L. (2013). *Tropical cyclone report: Hurricane Sandy. National Hurricane Center Tech. Rep. AL182012*. Retrieved from www.nhc.noaa.gov/data/tcr/AL182012_Sandy.pdf.

Dunkerton, T. J., Montgomery, M. T., & Wang, Z. (2009). Tropical cyclogenesis in a tropical wave critical layer: easterly waves. *Atmospheric Chemistry and Physics Discussions*, *8*(v), 11149–11292. http://doi.org/10.5194/acpd-8-11149-2008

Galarneau, T. J., Davis, C. A., & Shapiro, M. A. (2013). Intensification of Hurricane Sandy (2012) through Extratropical Warm Core Seclusion. *Monthly Weather Review*, *141*(12), 4296–4321. http://doi.org/10.1175/MWR-D-13-00181.1

Harr, P. A., & Elsberry, R. L. (2000). Extratropical Transition of Tropical Cyclones over the Western North Pacific. Part I: Evolution of Structural Characteristics during the Transition Process. *Monthly Weather Review*, *128*(8), 2613–2633. http://doi.org/10.1175/1520-0493(2000)128<2613:ETOTCO>2.0.CO;2

Harr, P. A., Elsberry, R. L., & Hogan, T. F. (2000). Extratropical Transition of Tropical Cyclones over the Western North Pacific. Part II: The Impact of Midlatitude Circulation

Characteristics. *Monthly Weather Review*, *128*(8), 2634–2653. http://doi.org/10.1175/1520-0493(2000)128<2634:ETOTCO>2.0.CO;2

Jones, S. C., Harr, P. a., Abraham, J., Bosart, L. F., Bowyer, P. J., Evans, J. L., … Thorncroft, C. (2003). The Extratropical Transition of Tropical Cyclones: Forecast Challenges, Current Understanding, and Future Directions. *Weather and Forecasting*, *18*(6), 1052–1092. http://doi.org/10.1175/1520-0434(2003)018<1052:TETOTC>2.0.CO;2

Lackmann, G. M. (2015). Hurricane Sandy before 1900 and after 2100. *Bulletin of the American Meteorological Society*, *96*(4), 547–560. http://doi.org/10.1175/BAMS-D-14-00123.1

Lussier, L. L., Rutherford, B., Montgomery, M. T., Boothe, M. A., & Dunkerton, T. J. (2015). Examining the Roles of the Easterly Wave Critical Layer and Vorticity Accretion during the Tropical Cyclogenesis of Hurricane Sandy. *Monthly Weather Review*, *143*(5), 1703–1722. http://doi.org/10.1175/MWR-D-14-00001.1

Munsell, E. B., & Zhang, F. (2014). Prediction and uncertainty of Hurricane Sandy (2012) explored through a real-time cloud-permitting ensemble analysis and forecast system assimilating airborne Doppler radar observations. *Journal of Advances in Modeling Earth Systems*, *6*(1), 38–58. http://doi.org/10.1002/2013MS000297

National Oceanic and Atmospheric Administration. (2015). Climate Prediction Center. Retrieved December 1, 2015, from http://www.cpc.ncep.noaa.gov/

Palmén, E. (1949). Meridional circulations and the transfer of angular momentum in the atmosphere. *Journal of Meteorology*, *6*, 429–430.

Palmén, E. (1951). The role of atmospheric disturbances in the general circulation. *Quarterly Journal of the Royal Meteorological Society*, *77*(333), 337–354. http://doi.org/10.1002/qj.49707733302

Palmén, E. (1958). Vertical Circulation and Release of Kinetic Energy during the Development of Hurricane Hazel into an Extratropical Storm. *Tellus, Series A: A Quarterly Journal of Geophysics*, *10*(I), 1–23. http://doi.org/10.1111/j.2153-3490.1958.tb01982.x

Reynolds, R. W., Smith, T. M., Liu, C., Chelton, D. B., Casey, K. S., & Schlax, M. G. (2007). Daily High-Resolution-Blended Analyses for Sea Surface Temperature. *Journal of Climate*, *20*(22), 5473–5496. http://doi.org/10.1175/2007JCLI1824.1

Rhome, J. R., Sisko, C. A., & Knabb, R. D. (2006). On the Calculation of Vertical Shear: An Operational Perspective. In *Preprints: 27th Conference on Hurricanes and Tropical Meteorology*.

Riehl, H. (1945). *Waves in the easterlies and the polar front in the tropics.* Misc. Rep. No. 17, Department of Meteorology, University of Chicago, Chicago, IL.

Riehl, H., Yeh, T. C., Malkus, J. S., & la Seur, N. E. (1951). The north-east trade of the Pacific Ocean. *Quarterly Journal of the Royal Meteorological Society*, *77*(334), 598–626. http://doi.org/10.1002/qj.49707733405

Ripesi, P., Ciciulla, F., Maimone, F., & Pelino, V. (2012). The February 2010 Arctic Oscillation Index and its stratospheric connection. *Quarterly Journal of the Royal Meteorological Society*, *138*(669), 1961–1969. http://doi.org/10.1002/qj.1935

Rossby, C.-G., & Starr, V. P. (1949). INTERPRETATIONS OF THE ANGULAR-MOMENTUM PRINCIPLE AS APPLIED TO THE GENERAL CIRCULATION OF THE ATMOSPHERE. *Journal of Meteorology*, *6*(4), 288. http://doi.org/10.1175/1520-0469(1949)006<0288:IOTAMP>2.0.CO;2

Roundy, P. E. (2011). *Tropical extratropical interactions*. (W. K. . Lau & D. E. Waliser, Eds.)*Intraseasonal Variability in the Atmosphere-Ocean Climate System* (Second Edi). Chichester, UK: Praxis Publishing.

Shen, B.-W., DeMaria, M., Li, J.-L. F., & Cheung, S. (2013). Genesis of Hurricane Sandy (2012) simulated with a global mesoscale model. *Geophysical Research Letters*, *40*(18), 4944–4950. http://doi.org/10.1002/grl.50934

Starr, V. P. (1948). ON THE PRODUCTION OF KINETIC ENERGY IN THE ATMOSPHERE. *Journal of Meteorology*, *5*(5), 193–196. http://doi.org/10.1175/1520-0469(1948)005<0193:OTPOKE>2.0.CO;2

Tibaldi, S., & Molteni, F. (1990). On the operational predictability of blocking. *Tellus A*. http://doi.org/10.3402/tellusa.v42i3.11882

Torn, R. D., Whitaker, J. S., Pegion, P., Hamill, T. M., & Hakim, G. J. (2014). Diagnosis of the Source of GFS Medium-Range Track Errors in Hurricane Sandy (2012). *Monthly Weather Review*, *143*(1), 132–152. http://doi.org/10.1175/MWR-D-14-00086.1

Wheeler, M. C., & Hendon, H. H. (2004). An All-Season Real-Time Multivariate MJO Index: Development of an Index for Monitoring and Prediction. *Monthly Weather Review*, *132*(8), 1917–1932. http://doi.org/10.1175/1520-0493(2004)132<1917:AARMMI>2.0.CO;2

Yeh, B. T. (1950). The Circulation of the High Troposphere over China in the Winter of 1945-46. *Tellus, Series A: Dynamic Meteorology and Oceanography*, *2*(3), 173–183. http://doi.org/10.1111/j.2153-3490.1950.tb00329.x

LIST OF TABLES

Table 1. Influential conditions used to evaluate the planetary-scale environment several days ahead of, leading up to, and prior to mature development of Hurricane Sandy. Listed are the behavior/contributions associated with each condition.

Index/Measure	Behavior/Contribution
AOI	Negativity corresponds to enhanced equator-to-pole meridional exchange, and more so with mass abundance (anomalously deep high heights) concentrated north of 75°N
NAOI	Negativity corresponds with AOI, however, contingent on meridional exchange occurrence within 0-60W when northwest-to-southeast ridge-trough dipole may be maximized
MJO	Value of one or greater corresponds to tropical mass buildup from persistent convection; Coincident southward extension of mid-latitude activity appeared necessary for impactful modulation northward
Blocking	Strong connection to increasing negativity of AOI and NAOI, but may be minimized when the former indices start to reverse; Maximized when mid-latitude / subtropics impinge; Minimized under strong zonal flow regime
Vertical Shear	Deep measure of strong vs weak shear was consistent with strengthening versus weakening intensity for mature storms; Shallow measure was more indicative for premature waves and their migration (consistent with Rhome et al. 2006)
Deformation	Zones are conducive pathways for storm intensification and progression as they provide temporary low vertical shear environments; Favored locales are near (often south-southwest of) mid-latitude / subtropical ridge impingement
Immediate Predecessor Storms/Activity	Tropical storms or mature hurricanes out ahead of precursor waves can leave conducive wake environments or modify the existing larger environment in a favorable manner depending upon conditions upstream and down, e.g., Rafael's track left a temporary low shear pathway for the pre-Sandy disturbance displaced the NASH temporarily (a Caribbean shear contributor), and stirred the larger hemispheric circulation in timely manner

Table 2. Total number of tropical storms and those which became hurricanes/typhoons for 2012 and the departure from the 30-year mean for the Atlantic, Eastern Pacific, and Western Pacific Basins. The 30-year mean period of 1985-2014 was chosen to be consistent with ERA Interim and sea surface temperature anomalies used in this study.

Region	**Total Storms /Departure**	**Hurricane [Typhoon] /Departure**
Atlantic	19 / +6	10 / +3
Eastern Pacific	17 / -3	10 / +2
Western Pacific	27 / -6	16 / +3
Total	63 / -2	36 / +9

LIST OF FIGURES

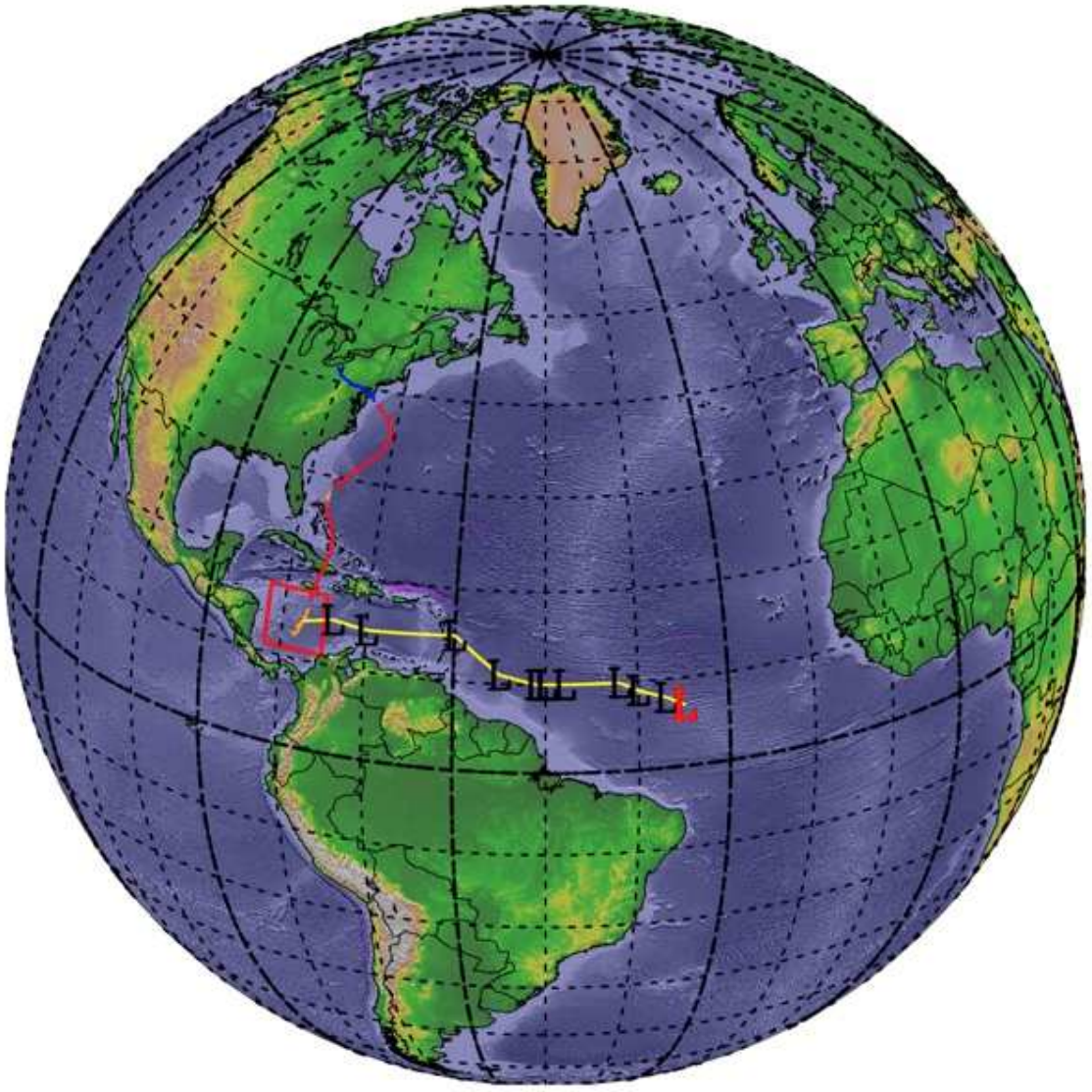

Figure 1. The trajectory of Sandy from best track where blue (extratropical), red (hurricane), and orange (tropical storm) lines identify the various stages of development. The yellow (estimated) line and red (black) symbols indicate the origin (and subsequent) locations of the precursor disturbance adapted from Lussier et al. (2015). The red box identifies the main tropical development location within the Caribbean (discussed in part two).

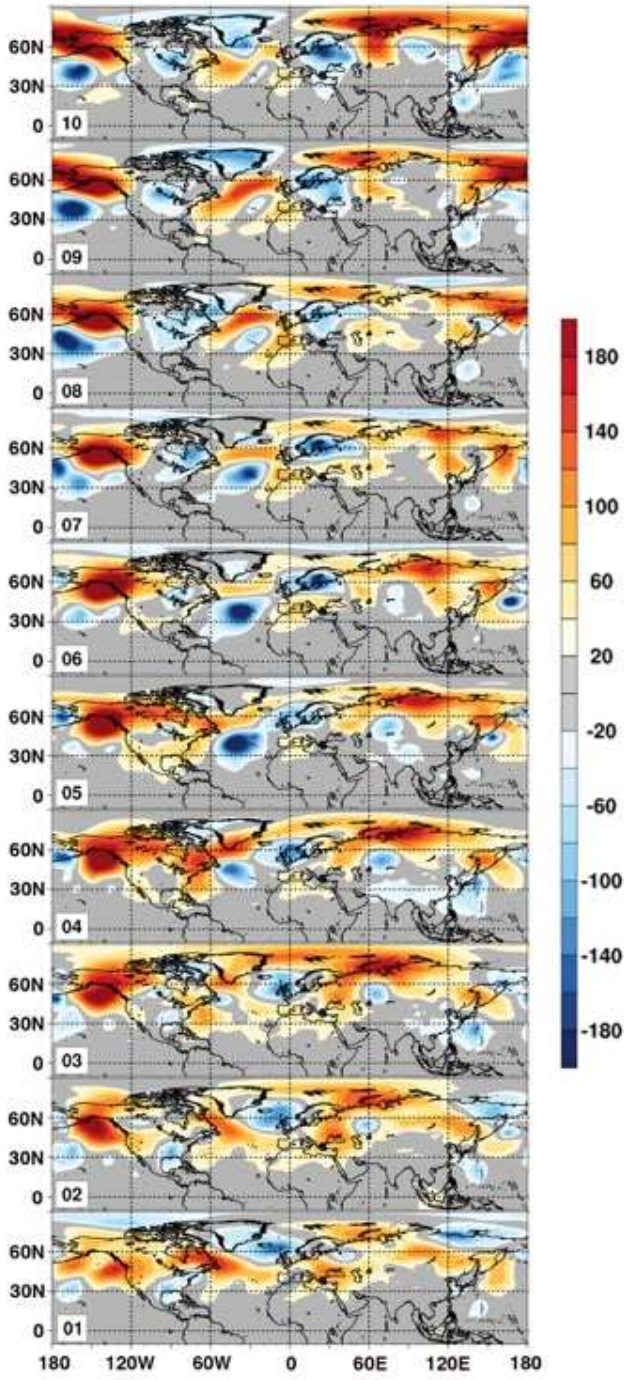

Figure 2. 700 hPa geopotential height anomalies (meters) from ERA Interim analysis computed for October 1-10, 2012 (00 UTC) against the 30-year average (1985-2014).

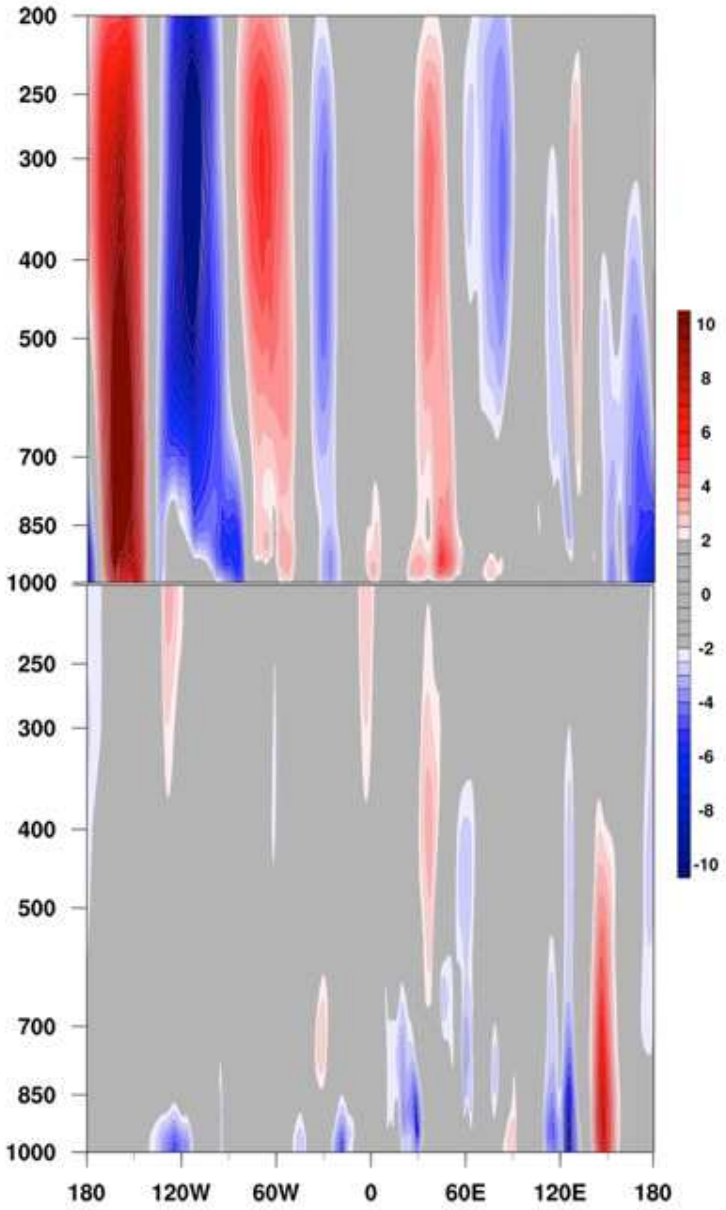

Figure 3. Meridional mass flux profile (ρv, $kgm^{-2}s^{-1}$) averaged over the 10-day period (October 1-10, 2012) along 25 and 60°N, bottom and top panel, respectively, where blue (red) shade identify southward (northward) flux motion.

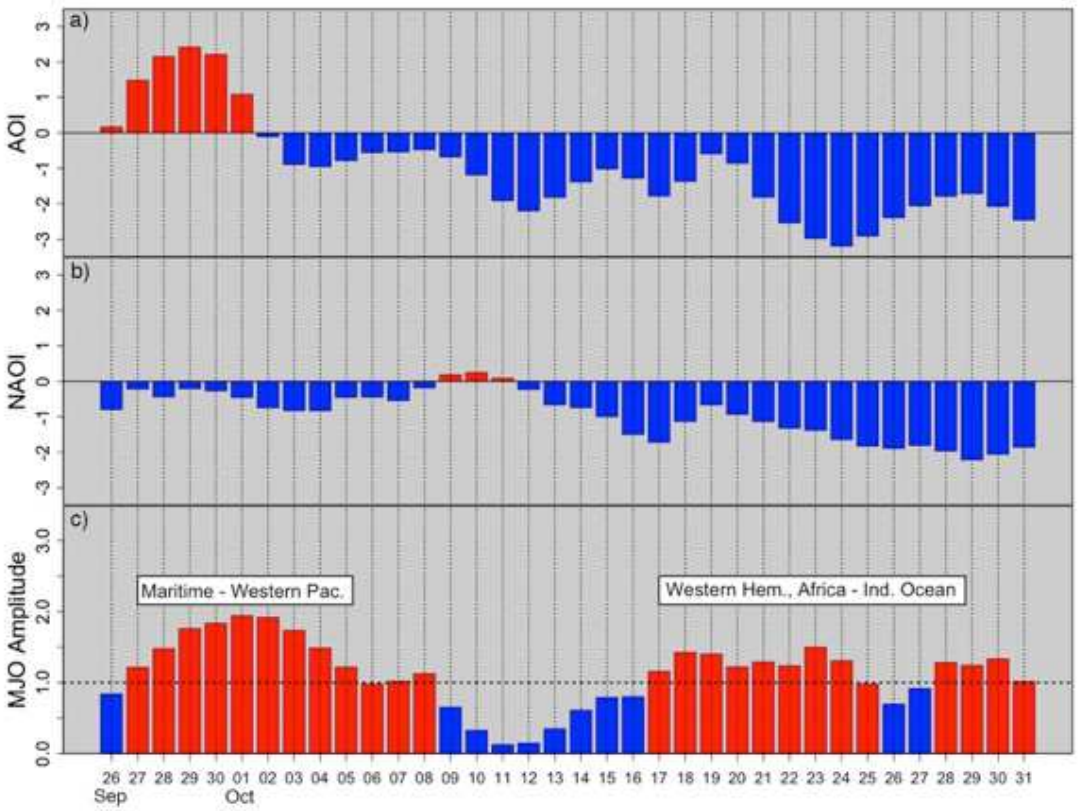

Figure 4. Daily indices for the Arctic, North Atlantic, and Madden-Julian Oscillations for September 26 – October 31, 2012. The MJO Amplitude is representative of the square root of the two lead principal components from the Real-time Multivariate MJO (RTM) Index (RMM^1 and RMM^2) as used by NOAA CPC (2015) where a value of one or greater is consistent with an active phase.

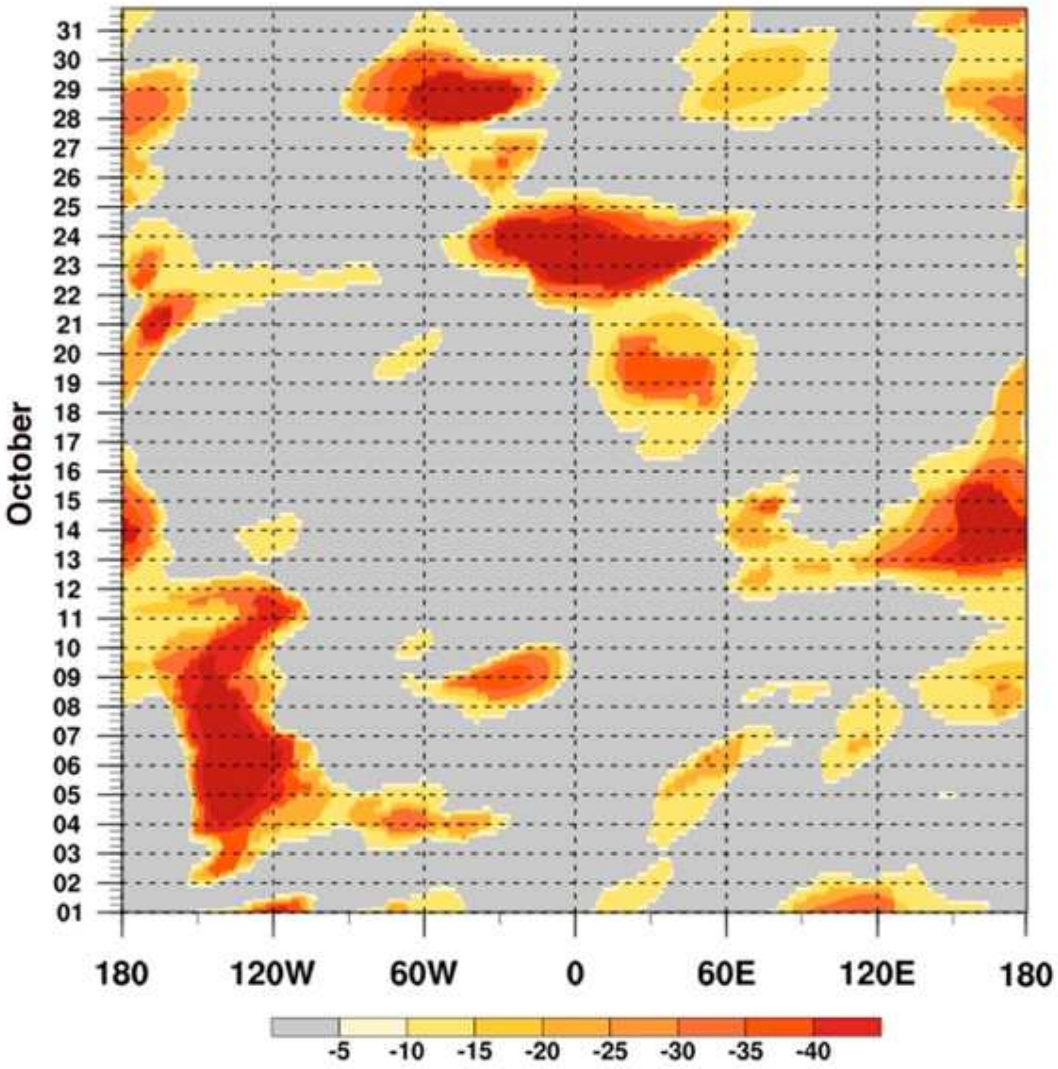

Figure 5. 6-hourly atmospheric blocking index between 80 and 60°N for the 700 hPa geopotential height field (meters $[°\text{lat}]^{-1}$) for all longitudes from ERA Interim analysis where value negativity is consistent with increased blocking strength.

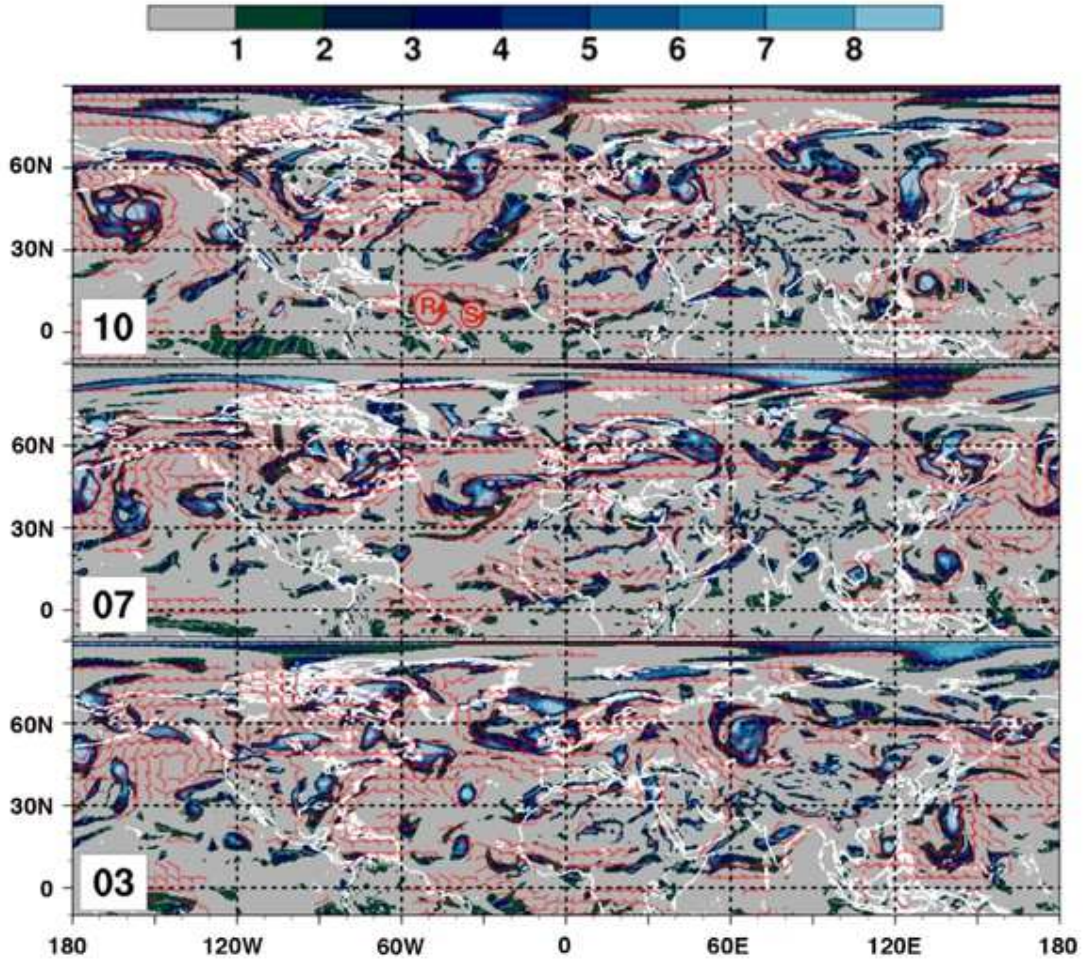

Figure 6. Positive relative vorticity (x 10^{-5} s^{-1}) shaded and wind from ERA Interim for October 3, 7, 10, 2012 (bottom-to-top) for 00 UTC. Red wind barbs signify magnitude equal to and greater than 7.5 ms^{-1}. Red cyclonic symbols of "R" and "S" (top panel only) identify the position of tropical storm Rafael and the pre-Sandy disturbance, respectively.

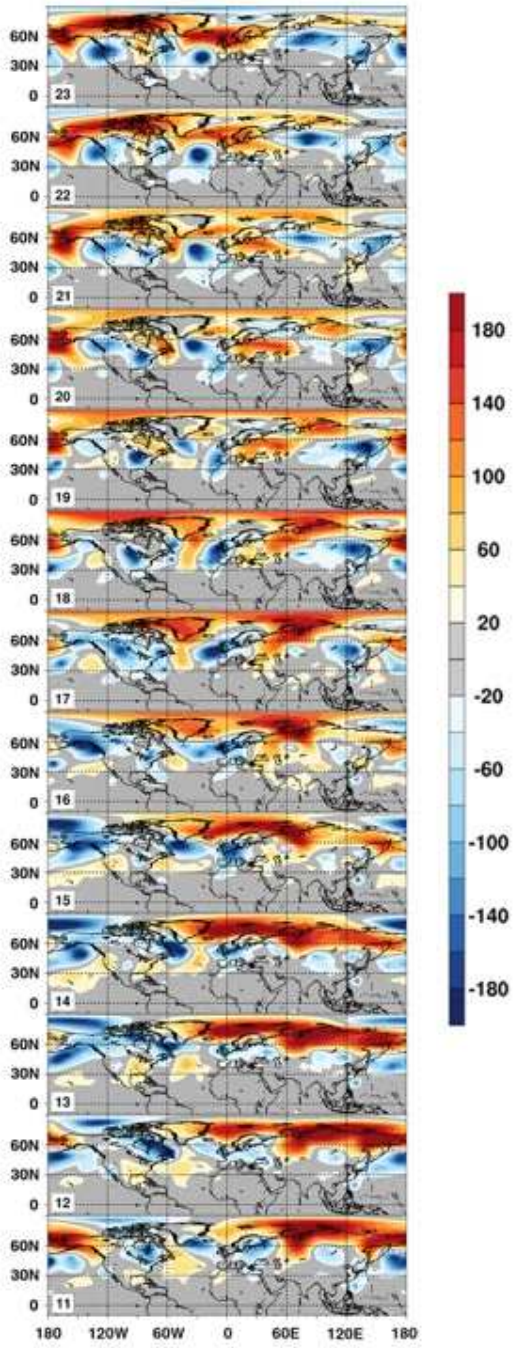

Figure 7. Same as Figure 2 except for October 11-23, 2012.

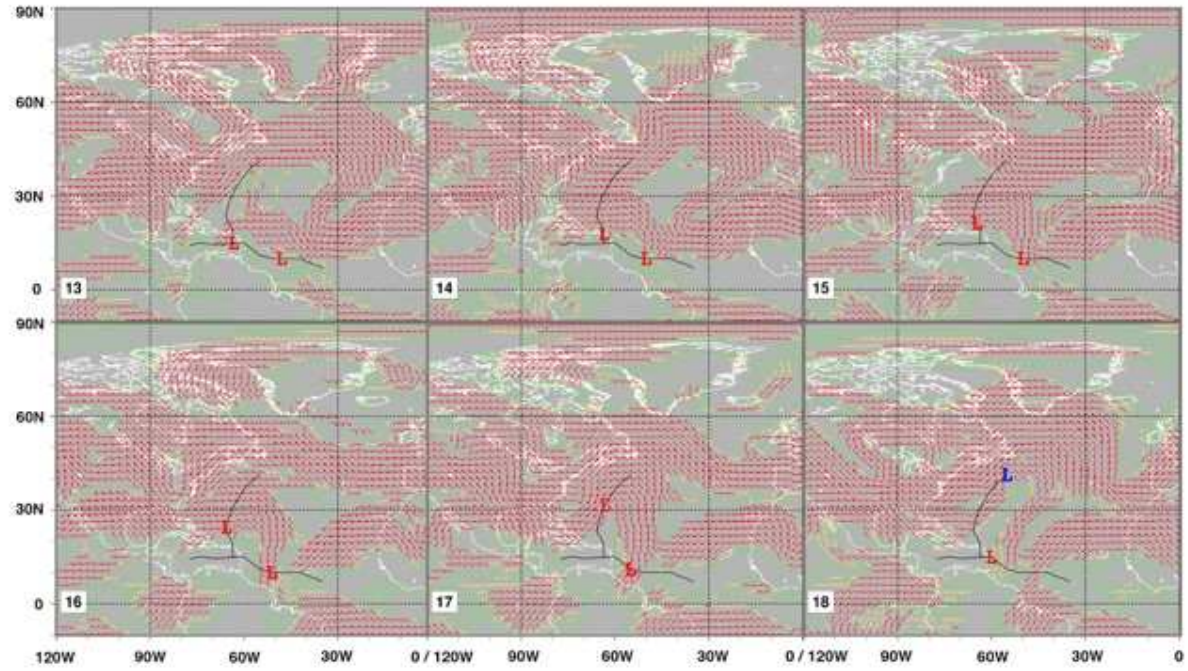

Figure 8. Regional view of deep layer wind shear [ms^{-1}, 200-850 hPa] with trajectory (location) of Rafael and precursor Sandy represented by a thin-black line (red/blue "L" symbol) where red/blue is indicative of a tropical/extratropical core as classified in best track. Wind-shear barb coloring of green, yellow, and red signifies magnitude value ranges of 7.5-12.5, 12.5-15.0, and greater than 15.0 ms^{-1}, respectively.

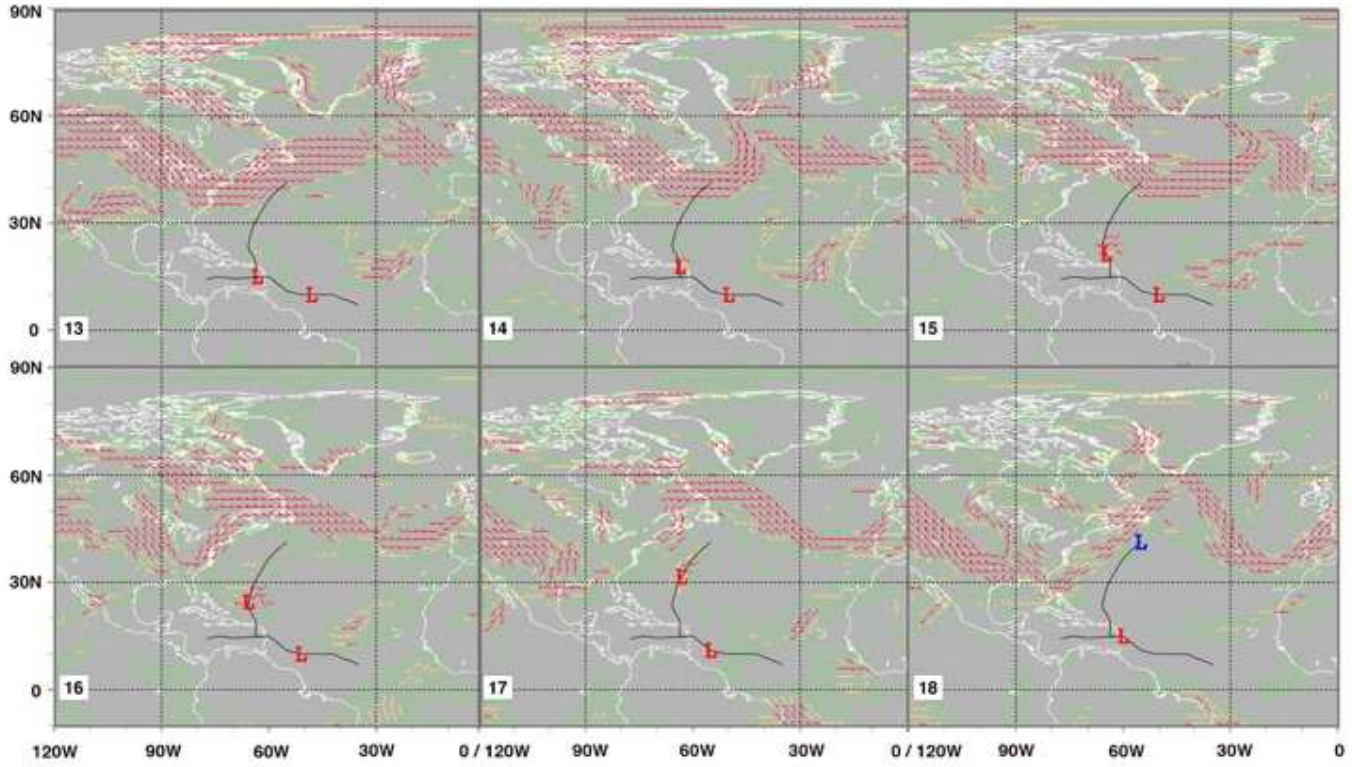

Figure 9. Same as Figure 8 except for shallow layer wind shear [ms^{-1}, 500-850 hPa].

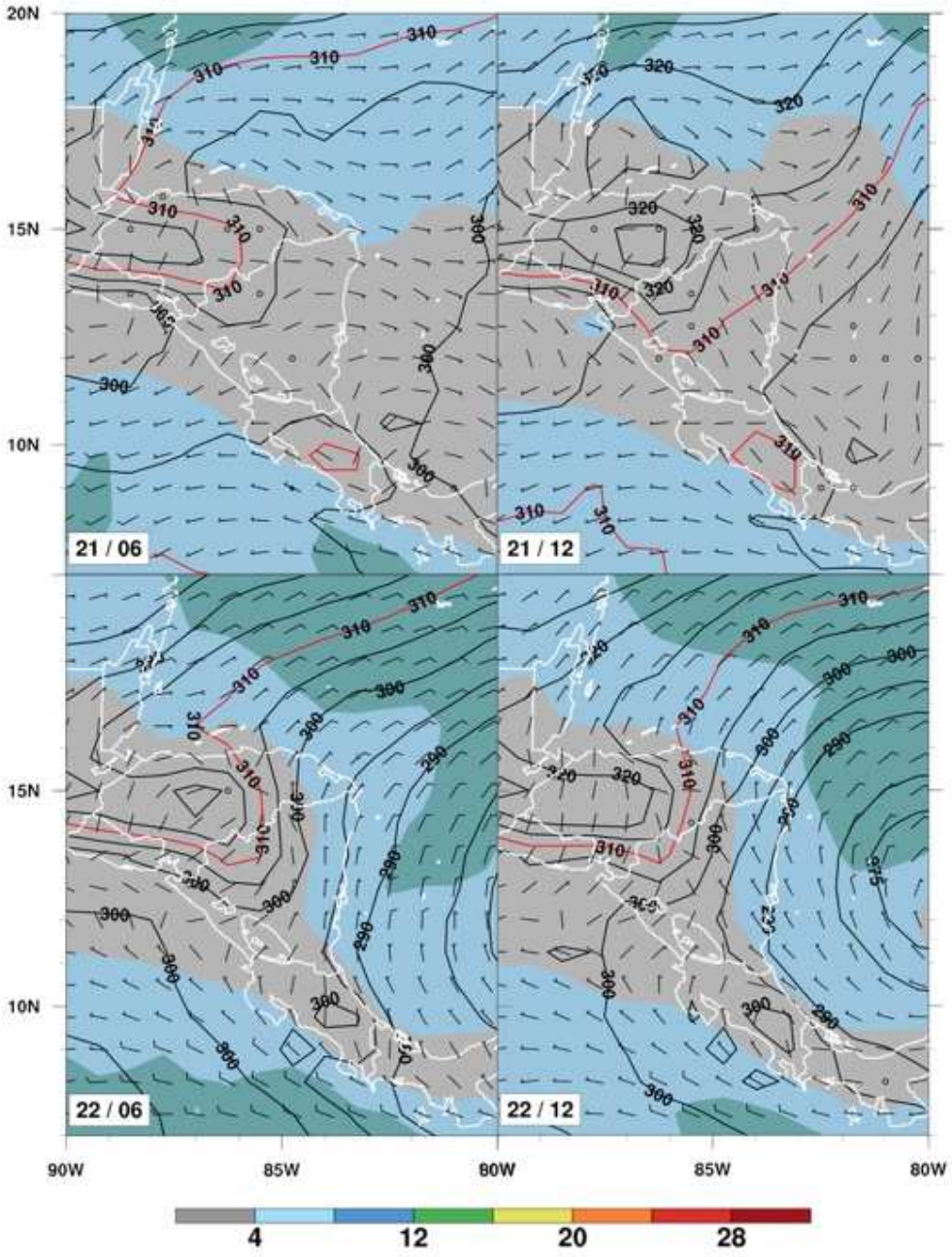

Figure 10a. Hourly snapshots of 975 hPa geopotential height (black contour lines, m) and wind (barbs and shaded speed ms^{-1} per color bar) for October 21 and 22 (top and bottom), 06 and 12 UTC (left to right), respectively, zoomed in over Central America. The red height contour (310 m) indicates the southward extension of higher heights toward Costa Rica.

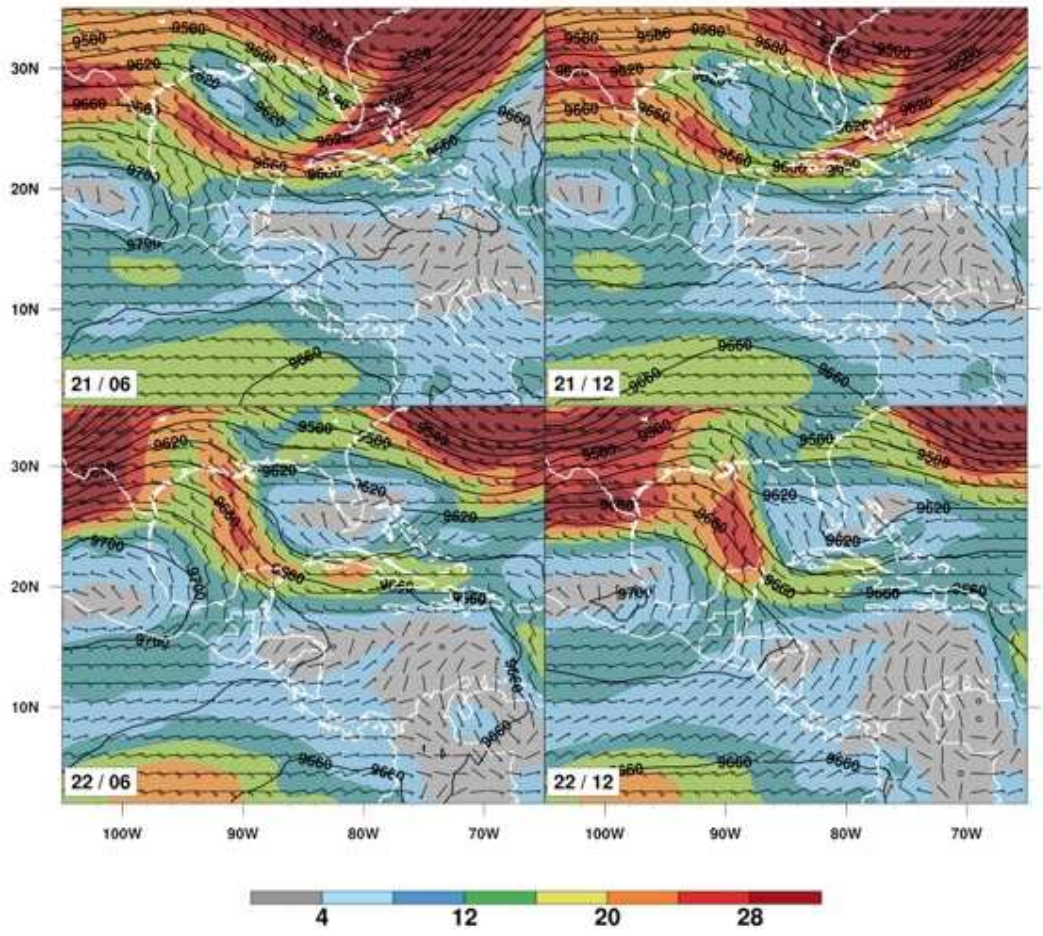

Figure 10b. Same as Fig. 10a except for 300 hPa illustrating the large-scale view.

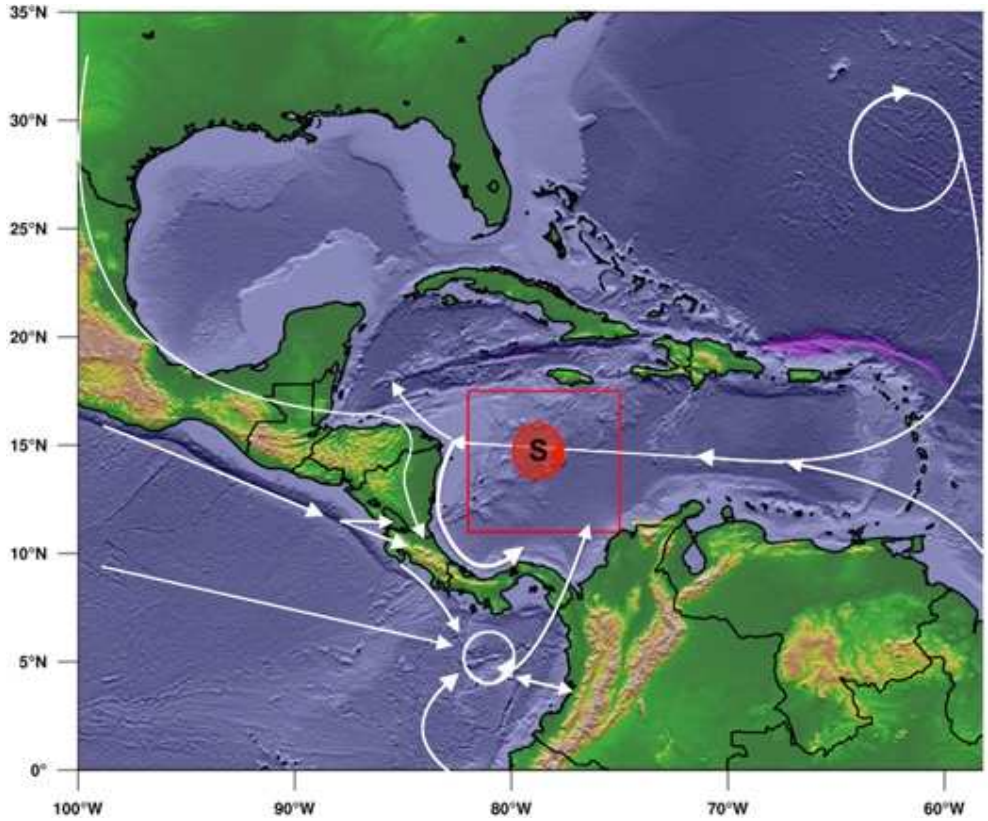

Figure 11. Map of Caribbean flows.

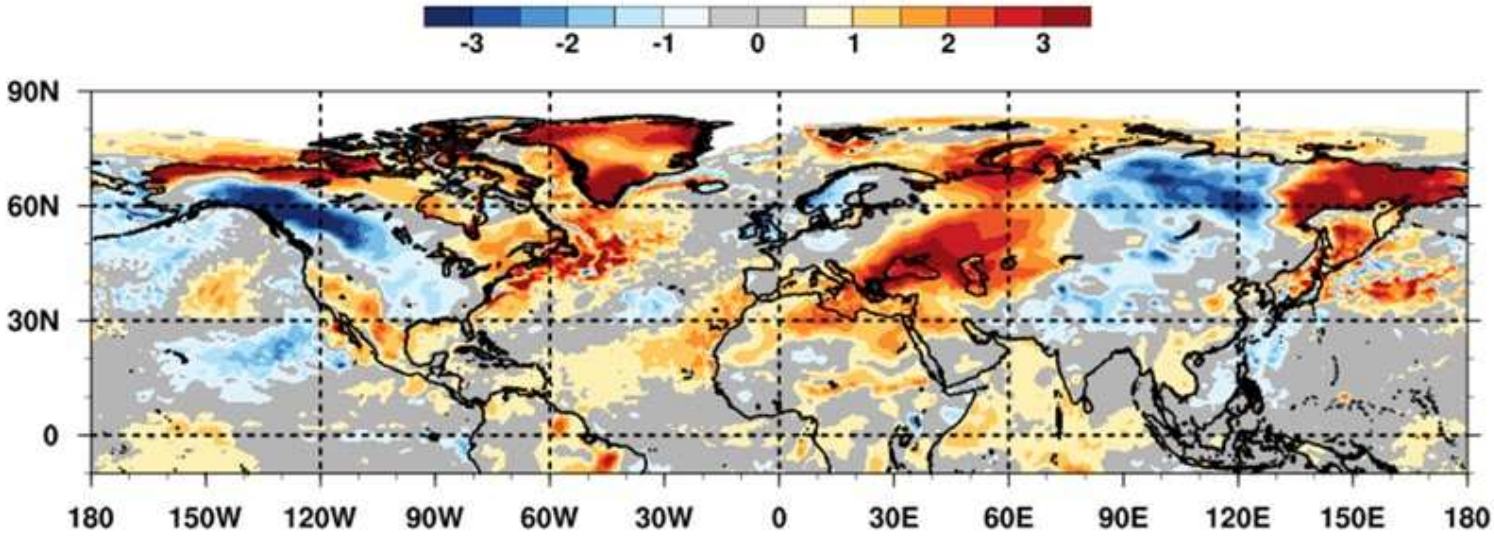

Figure 12. Averaged October 2012 sea-surface and 2-meter landmass temperature anomalies (°C) from NOAA's high-resolution-blended analyses and ERA Interim, respectively. Areas in white indicate sea ice.

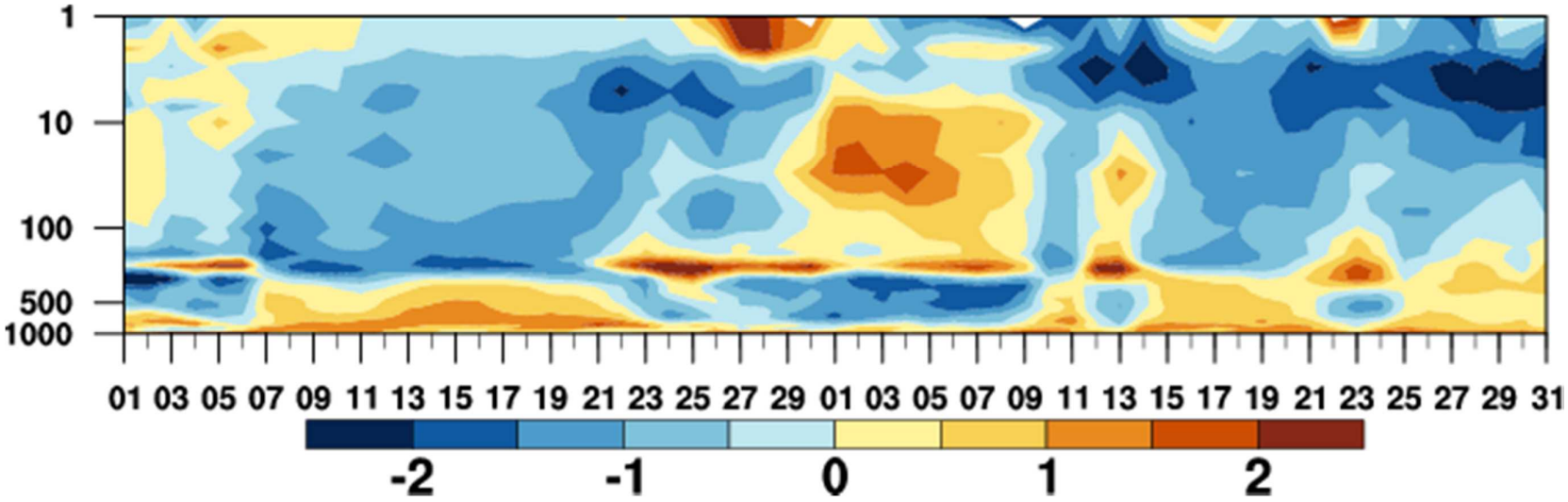

Figure 13. Standardized daily temperature anomaly with height north of 80°N from ERA Interim for October-September 2012.

Paper three

Hurricane Sandy (2012). Part II: The dynamics within the Caribbean environment preceding rapid development

Matthew G. Fearon[1], Michael L. Kaplan[1], and John F. Mejia[1]

Journal of Geophysical Research - Atmospheres

---

[1]Desert Research Institute, Reno, Nevada, USA.

Corresponding Author: Matthew G. Fearon, Division of Atmospheric Sciences, Desert Research Institute, Reno, NV 89512, E-mail: matthew.fearon@dri.edu

Key Points. Caribbean precursor hurricane dynamics, precursor hurricane environment, mountainous terrain and tropical development, terrain-induced mesoscale jets, land-ocean thermal gradients, mountain-plains solenoid circulation

Abstract. The analysis and results presented herein represent part two of a two-part series on the precursor environment associated with Hurricane Sandy (2012). In this portion of the study, the mesoscale dynamics within the Caribbean environment that preceded and contributed to tropical development are examined for the period 22-24 October. Evaluation of the potential impact of the southern Caribbean landmass and the associated complex terrain on storm development and intensification was the primary impetus for this study. Analysis of the key mesoscale dynamics in the precursor environment, including low-level jet structures and impact of daytime orographic heating, was facilitated by two mesoscale model simulations over the Caribbean Sea, a control run and no-terrain experiment generated by the Advanced Research Weather Research and Forecasting model. A host of remote sensing products were used to evaluate model performance. Results indicate that mountain-induced forcing played a critical role in the generation of environmental vorticity that comprised the primary vortex inflow band on the southeast side of the storm.

1. Introduction

In this two-part study, the precursor environment of Hurricane Sandy (2012) is examined. The motivation behind the study rests on the environmental circulations and adjustments that precede and contribute to the tropical development. In part one, the planetary-scale adjustments over the Northern Hemisphere were analyzed in terms of their role in the initiation and trajectory taken by the pre-Sandy disturbance during the period 1-22 October. Now, in part two, presented herein, the organization of the mesoscale environment over the southwestern Caribbean and the associated terrain-induced dynamics influential in Hurricane Sandy's rapid development have been evaluated for the period 22-24 October.

As discussed in part one, several recent contributions on Hurricane Sandy now exist in the literature (Shen et al. 2012; Galarneau et al. 2013; Munsell and Zhang 2014; Torn et al. 2014; Lackmann 2015; Lussier et al. 2015). Of those, two articles emphasize the precursor period, namely Shen et al. 2012 and Lussier et al. 2015. However, neither contribution describes in detail the preliminary environmental adjustments from the standpoint of the

planetary- and the meso- scales. Lussier et al. (2015) examined the general locations of the environmental vorticity filaments across the Caribbean zone and vortex accretion, but the mechanisms of vorticity generation upstream from storm-core convection, including the role of the localized concentric landscape and the associated complex topography, remain undocumented. In general, the contributing role of the nearby or surrounding landmass on the development of a preexisting (incipient) tropical disturbance remains scant in the literature with a couple exceptions (i.e., Mozer and Zehnder 1996a and b). It is from within this context that part two of this study provides a unique perspective on the precursor hurricane environment.

As in part one, this analysis complements recent contributions on Hurricane Sandy. The precursor mesoscale environment is evaluated over the southwestern Caribbean. Two distinct low-level jet features were identified in the peripheral Caribbean environment (from the west and south of the developing vortex) where each was a representative response of the flow interaction with the local landscape and topography. The organization of the westerly momentum between the disturbance and the surrounding landmass/terrain led to strong vorticity generation, just upstream from the vortex inflow region, due to the curved nature of airflow. Convergence of the latter with surging southerly momentum (from convection south of Panama) occurred on the southeast side of the vortex inflow region. The timing and inflow of the consolidated vorticity from both airstreams was found to be codependent with rapid development, as examined by the change in the central pressure, the contraction of the tangential wind field, and the positive relative vorticity accretion over time within the vortex.

Analysis of these environmental (mesoscale) features was facilitated through numerical simulation of a control and an experimental no-terrain run. The absence of the

terrain did not preempt cyclone development, however, intensification, track, and concentric organization were severely hampered where the storm structure revealed bears resemblance to a southwest-to-northeast elongated mid-latitude cyclone. The authors concede the southwestern Caribbean zone remains limited in terms of observational data, however, Best Track information and satellite-derived scatterometter surface winds, lidar profiles, and other blended (brightness) imagery on cloud field locations provided evaluation options for the control simulation, including storm position, intensity, and characteristics associated with vertical structure.

The outline of this paper is as follows. Section 2 begins with a brief background overview of relevant literature on the precursor hurricane environment, including cyclone formation avenues described in the literature. Section 3 reviews the Caribbean zone and the common flow regimes in association with the unique landscape. The observational data and remote sensing products are described in section 4 with section 5 reserved for the model description of the control and no-terrain experiment simulations. The evaluation of the model simulations against available data is presented in section 6. Analysis and discussion of model results is presented in section 7 for the period preceding and leading up to Sandy's rapid development phase during 22-24 October. As part of the discussion, an overview of the precursor environment is given with description of the key mesoscale features, including the landmass/terrain influence, the two primary mesoscale jet structures, and the resultant vorticity generation and vortex accretion. Much of the discussion is facilitated through the comparison of the control versus no-terrain simulation. The manuscript summary and concluding remarks are provided in section 8.

2. Background in brief

The literature on tropical meteorology, in particular mechanisms of tropical cyclone formation, is vast. Acquiring insight on all proposed theories (from ~ the 1940s to present), including the manner in which they differ (and or overlap), was an interesting yet monumental task. In this regard, the review chapter by Montgomery and Smith (2014) provided a welcoming summary.

The underlying premise of early and recent theories on tropical cyclone genesis (described below) appears inherently tied to the formative work presented on the northeasterly trades, the trade-wind inversion, and especially the nature and scale of the equatorward growth of convection (Riehl et al. 1951). The 1951 study represented the first quantitative analysis of tropical cumulus convection and its role in maintaining the rising branch of the Hadley Cell. The conceptual hypothesis on deep, narrow undiluted cumulonimbus clouds (namely, hot towers) was an important revelation following this study. These clouds were determined to be a manifestation and transport mechanism of the latent heat flux from the ocean. Subsequent energy-budget computations presented by Riehl and Malkus (1958) and Riehl and Simpson[10] (1979) demonstrated their substantial role in regulating the hemispheric heat budget. As recalled by Simpson,

> The trade wind inversion is essentially a leaky wall [that aids][11] the transfer of energy to the equatorial trough. Clouds make holes in it [the inversion] and gradually lift it up and, in the equatorial trough [zone] clouds transfer some of the heat energy from the ocean surface to the high troposphere. [Riehl] and I believed these clouds [hot towers] within the equatorial trough were undiluted and were carrying boundary layer air up to the tropopause region [J. Simpson 2009, personal communication; Lewis et al. 2012].

[10] In this paper, reference is also made to Joanne Malkus, her name before marriage to Robert Simpson in 1965.
[11] The authors have inserted the bracketed information within the quotes.

Over the last half-decade, these hypothesized cumuli (referred to in different ways) have remained an integral component of all proposed theories on tropical cyclone formation (e.g., Charney and Eliassen 1964; Ooyama 1964; Yanai 1964; Gray 1975; Ooyama 1982; Willoughby et al. 1982; Emanuel 1989; Montgomery and Farrell 1993; Harr et al. 1996; Gray 1998; Hendricks et al. 2004; Montgomery et al. 2006; Raymond and Sessions 2007; Dunkerton et al. 2009; and many others). And while undiluted towers have not been observed directly, vertical cloud growth to the tropopause remains viable whereby ice-based condensate aloft are believed to counteract the perceived low to mid-level entrainment process (see the synthesis by Zipser 2003).

As outlined by several authors (e.g., Gray 1998; Hendricks et al. 2004; Zawislak and Zipser 2014), a unified consensus has been established on the necessary environmental conditions needed for tropical cyclone formation. Those include concentrated low-level cyclonic vorticity, upper-level divergence, warm sea surface temperatures, low vertical wind shear, a deep moist layer, and mature clustering convection (e.g., Gray 1968; McBride and Zehr 1981; Merrill 1988; Gray 1998). However, the outstanding problem that remains is how a tropical disturbance (e.g., a lower level easterly wave, or clustering convective complexes) transforms into a finite-amplitude surface vortex (Hendricks et al. 2004; Raymond and Sessions 2007; and others)? This question has been the centerpiece in a host recent literature since the early 1990s (e.g., Montgomery and Farrell 1993; Ritchie 1995; Blister and Emanuel 1997; Hendricks et al. 2004; and many others).

Prior to the early 1990s, numerical and theoretical studies implicitly assumed the presence (or development) of a low-level rotating vortex in association with a tropical disturbance. The pathway in which the disturbance achieved rotation was not fully

elucidated. Under this premise, Charney and Eliassen (1964) proposed a numerical scheme for vortex growth whereby the upper-level convectively generated diabatic heating rate was expressed proportional to the moisture convergence profile (nonlinear terms were neglected). Independently, Ooyama (1964) introduced a similar concept, but later augmented his model to include the nonlinear feedback (warming) from convective downdraft entrainment and latent heat flux from the sea (see Ooyama 1969). Computations from Charney and Eliassen's linear model revealed horizontally uniform convective growth, however, instabilities in their equation formulations, perceived as realistic at the time, were incorrectly identified as a cross-scale cooperation between the convection and larger-scale vortex[12]. Charney and Eliassen proposed the name Conditional Instability of the Second Kind (CISK) for this mechanism. Unfortunately, the CISK name lumped Charney and Eliassen's linear model together with Ooyama's nonlinear theory. Ooyama's approach has been described as a more accurate representation of the cross-scale cooperation concept (see Smith 1997 for detailed discussion).

In contrast to the former viewpoints, Emanuel (1986) demonstrated that the intensity of a mature hurricane could be more appropriately explained by evaporation of warm ocean water into the unsaturated near-surface air, a rate prescribed by the local surface wind speed. The sharp difference in the heat capacity between the ocean and the air identified the principle mechanism behind this theory, namely Wind-Induced Surface Heat Exchange (WISHE, Emanuel 1989; 1991). As discussed by Smith (1997), strong similarities exist

[12] Akira Kasahara and Shigekata Syōno also introduced similar mathematical treatments for the tropical cyclone prior to 1964. However, their results were consumed by the convective scale, a response prompted by the development of excess conditionally instability (when the ambient lapse rate becomes steeper than moist adiabatic rate; a reservoir of convective available potential energy). The latter profile does not accurately reflect mean state of tropical soundings (Betts 1982). A proportional setting of the diabatic heating rate to the vertical velocity at the coincident heating location (an important nuance from 1964 formulations) likely introduced the over dominance of convection (see Kasahara 2000).

between WISHE and Ooyama's model and perceived differences might be more tied to physical interpretation.

As mentioned earlier, WISHE presumes a disturbance has acquired rotation. Therefore, over the last two decades, researchers have revisited the theory of incipient development in search of a mechanistic pathway in which rotation develops precedent to the WISHE process (Hendricks et al. 2004; Raymond and Sessions 2007; and others). Several hypotheses have been proposed and categorized into two paradigms that identify as "top-down", a cyclonic circulation originates at mid-levels and translates down to the surface, or "bottom-up", the inverse of top-down where rotation commences and builds upward from the surface (Montgomery and Smith 2014).

Both the former paradigms are predicated on the merger of mesoscale convective systems. Top-down theory is based on the interaction and merger of mid-level vortices, embedded in regions of stratiform precipitation in the wake of multiple convective bursts, whereby environmental background rotation facilitates the downward development of vorticity (Ritchie 1995; Ritchie and Holland 1997; Ritchie 2003). Blister and Emanuel (1997) reported similar findings where downdrafts of stratiform precipitation and associated evaporational cooling advected vorticity downward. Bottom-up theory is driven by low-level convergence that increases cyclonic vorticity near the surface through vortex stretching. Under this hypothesis, low-level convergence of angular momentum, axisymmetric spin, and upward motion develop in response to upper-level diabatic heating produced from an ensemble (of small horizontal-scale) vortical hot towers (e.g., Montgomery and Enagonio 1998; Hendricks et al 2004). Simpson et al. (1998) corroborates these findings, where hot tower clustering was found to be influential to tropical cyclone formation whereby the

production of deep profiles of latent and sensible heat (associated with updrafts and downdrafts, respectively) promoted hydrostatic surface pressure falls and an environment conducive for tropical cyclone genesis.

In a more recent paper by Dunkerton et al. (2009), tropical cyclone development was examined from the Lagrangian perspective over space and time. In this context, the local streamline minima associated with the incipient wave's low-level rotation was shown to be a protective zone (namely, the Kelvin's cat eye) wherein gradual enhancement of diabatic processes from convection and vorticity promote internal growth of the wave. A common location for cyclogenesis was found to occur at the intersection of the wave's critical latitude and its trough axis. The hypotheses associated with analysis technique have been identified as the marsupial paradigm. A series of papers where tropical cyclone development is re-examined on a case-by-case basis in the context of this paradigm have emerged in the recent literature (e.g., Hurricane Felix (2007) Wang et al. 2010a and 2010b; Hurricane Sandy (2012) Lussier et al. 2015).

3. Study area

a. Description of the unique southwestern Caribbean shoreline and topography

The southwestern Caribbean Sea represents a unique environment with its diverse surrounding landscape. The resident warm ocean body resembles a concentric-like bowl with the islands of Hispaniola, Jamaica, and Cuba to the north-northeast, Central America to the west and southwest, South America to the south-southeast, with minor openings to the northwest into the Gulf of Mexico (between the Mexican-Yucatan and Cuba) and to the east into the North Atlantic passing through the perforated Lesser Antilles Island chain. Although

steep, rugged terrain exists on the northern islands, the landscape along the southern perimeter, from west-southwest to south-southeast including Nicaragua, Costa Rica, Panama, and Colombia, arguably consists of orography that is even more complex. This southern portion of the bowl reveals undulating high terrain, at times in excess of 3,000 m, that is setback from the coast over Nicaragua, steep and narrow along Costa Rica and Panama, and broad yet massive along the northwest shore of Colombia. Gaps in the sierra that channel flow between the Caribbean and northeastern Pacific are well-documented features. Equally important, but largely undocumented to date, is the flow blocking capability of these mountains and the mesoscale phenomena that can result under certain low-level flow regimes. The near-circular geometry of the surrounding coastline also promotes a semi-permanent cyclonic circulation across the extreme southwestern portion of the Sea, namely the Caribbean gyre. This eddy flow pattern originates from easterly flow, as part of the Caribbean low-level jet deflected south and alongshore, following its intersection with the Nicaragua-Honduras coastline (see Fig. 1; white arrows).

b. Observed low-level Caribbean flow regimes

Although the low-level northeasterly trades and the upper-level return (from equatorial convection) facilitate the main north-south background circulation (i.e., the meridional circulation) over the Caribbean region, sub components of this flow regime either strengthen or weaken under certain scenarios. These sub-flow regimes manifest at the subsynoptic/meso-α scale, induced typically from baroclinicity and sea-surface temperature gradients, and work downscale (to the meso-β scale) triggering or enhancing tropical convection, that then builds (and re-propagates) back upscale. Several of these sub-flow

patterns were on display during and preceding Hurricane Sandy's incipient development (Fig. 1).

A cool air intrusion into the subtropics from the mid-latitudes exemplifies one such sub-component flow that deviates from the background meridional circulation. Such air originates from poleward latitudes over the North American continent, typically from October through March, and is modified as it moves equatorward over the warm Gulf of Mexico and Caribbean Sea. More intense variations of this airmass type may propagate along the eastern slopes of the Rocky Mountains, the Mexican Sierra Madre Oriental, and eventually the mountains of Nicaragua and Costa Rica upon entry into the Caribbean.

Alternatively, westerly airflow over the northeastern Pacific is often blocked by the mountains of Nicaragua and Costa Rica, or enters via gap flow near the Nicaragua-Costa Rica border. Due to the northwest-to-southeast orientation and transition of the terrain along the northeastern Pacific side, blocked flow often continues eastward and accelerates along the southern flank of Costa Rica and Panama before curling poleward and entering the Caribbean bowl through Panamanian mountain gaps. If a pressure gradient develops south of this landmass, in association with the sea-surface temperature, westerly-blocked flow may continue eastward toward the Andes Mountains of western Colombia. An oscillatory sea breeze circulation or related coastal-valley upslope flow on the west coast of Colombia, associated with the near-coast Andes (e.g., Lloró, Colombia), may also be operative as part of this flow scenario (see Poveda and Mesa 2000).

In concert with westerly flow along the southern coasts of Costa Rica and Panama, persistent southerly momentum, that originates as part of the southern hemisphere trades, often parallels the near-coast Andes of Peru and Ecuador and curls east (in response to the

Coriolis force) after it crosses the equator. This airstream may accelerate under certain conditions such as gradients between the land (or near-coast mountains) and the sea, in response to pressure falls in the southern Caribbean, or diabatic heating-induced gradients associated with local convection. Acceleration of this airstream has been identified as the Choco low-level jet consistent with its southeasterly approach into northwestern Colombia and the state of Choco, which borders eastern Panama (Poveda and Mesa 2000). Excitation of this airstream can yield strong anticyclonic vortices across the Sinu Valley of northern Colombia when incoming momentum from the North Pacific is initially blocked, then funneled north across the Panamanian/Colombian border, and wrapped inland around the northern extent of the Andes.

Finally, easterly flow associated with the Caribbean low-level jet, a southwest extension of the northeasterly trades (and a byproduct of the North American Subtropical High or NASH; white anticyclonic arrow near Bermuda, Fig. 1), represents another subsynoptic airstream. It has been documented in numerous studies and was found to be influential in the case of Hurricane Sandy's precursor environment, particularly as it relates to the wind shear environment over the Caribbean bowl (Wang and Lee 2007). In the presence of deepening low pressure in the Caribbean bowl, intensification of this jet is common. Similar to the Choco jet, easterly momentum may at times be blocked by the isolated Sierra Nevada de Santa Marta barrier over extreme northeastern Colombia. However, in this case, blocked flow is redirected northeastward. The combined effect of blocking on the Choco and Caribbean low-level jets over northern Colombia (southwest and north of Sinu Valley, respectively) appears to promote a concentrated zone of acceleration

and curvature (to the northwest) on the unblocked (offshore) components of momentum, respective to each jet.

The former airflow regimes are also influenced by thermal gradients generated according to the evolution of the diurnal cycle. Near-coast nighttime cooling over the landmass, at the base of high terrain and adjacent to the sea, is not uncommon and produces a low-level inversion where atop nocturnal jets frequent and accelerate offshore while insulated from surface friction. Daytime heating of the landmass, particularly the northeastern aspect of mountain slopes, introduces flow accelerations as part of a mountain-planes solenoid (MPS) circulation where air below the morning inversion is forced upslope, as the depth of the heated near-slope air column expands vertically, and the return branch aloft is stimulated and directed offshore. In this study, both the nighttime and daytime mechanisms are operative and examined. MPS circulations appear common along the southern periphery of the Caribbean bowl in association with the mountains of Costa Rica, Panama, and Colombia.

4. Observational datasets

Although the southwestern Caribbean zone remains data sparse in terms ground-based measurements, a variety of remote sensing products exist, which can provide a complementary perspective against model experiments. Those chosen for this study include National Aeronautics and Space Administration's (NASA)'s Cloud-Aerosol Lidar and Infrared Pathfinder Satellite Observation (CALIPSO), composite Geostationary visible and infrared imagery, Tropical Rainfall Measuring Mission (TRMM) data, and scatterometer surface wind derived from the ocean surface. A description of the satellite products used in this study and measurements extracted from the Best Track HURricane DATabase

(HURDAT2) are presented in Table 1. In addition, selected fields from North American Regional Reanalysis (NARR) were used in this study to facilitate the discussion.

5. Model description

a. Model physics and settings

The mass core non-hydrostatic (Advanced Research) Weather Research and Forecasting (WRF, version 3.5.1) model (Skamarock et al. 2008) was employed for this study. A horizontal grid resolution of 54 km (202 x 118 grid points) defined the parent domain in the east-west and north-south directions, respectively. Three nested grid domains of 18 (433 x 253), 6 (613 x 529), and 2 (898 x 862) km horizontal resolution, with one-way interactive strategy, were positioned within the parent domain and started at the same time (Fig. 2). The inner nest choice of 2 km horizontal resolution followed the discussion presented in Moeng and Wyngaard (1988) in conjunction with the finest resolution options possible given local computing resources. Furthermore it was determined that 2 km should be sufficient to resolve the interaction among moist convection and the low-level jets driven into the developing storm. The model configuration remained consistent for all four domains with 47 levels in the vertical extending up to 15 km Above Ground Level (AGL), 18 vertical levels below 1.5 km AGL, with the lowest model level set at 10 m AGL. The model physics included: (1) momentum and heat fluxes at the surface computed using an Eta surface layer scheme (Janjić 2001) following Monin-Obukhov similarity theory, (2) turbulence parameterization following the Mellor-Yamada-Janjić level 2.5 model (Mellor and Yamada 1974 and 1982; Janjić 2001), (3) convective processes following the Betts-Miller-Janjić cumulus scheme (Betts 1986; Betts and Miller 1986; Janjić 1994)—applied only on 54 and 18 km grids, (4)

cloud microphysical processes following explicit bulk representation of microphysics (Thompson et al., 2004; 2008), (5) radiative processes are parameterized using the Rapid Radiative Transfer Model for long wave radiation (Mlawer et al. 1997) and Dudhia's short wave scheme (Dudhia 1989), and (6) the land-surface processes following the Noah land surface model (Noah LSM) which provides the surface sensible, latent heat fluxes, and upward longwave and shortwave fluxes to the atmospheric model (Chen and Dudhia 2001; Ek et al. 2003). Performance evaluation of other model settings was not performed, as a sensitivity study of that type is beyond the scope of this paper. Instead, model results were compared against observational datasets for mean vortex location, sea-level pressure, tangential wind speed and direction (including environmental flows), and collocated water/ice vertical structure. Model-derived reflectivity patterns were also evaluated against observed data. Comparisons revealed close agreement overall and track error proved to be consistent with previous studies (discussed below).

b. Model simulations

To evaluate the mesoscale contributions in the Caribbean environment on Sandy's storm genesis and rapid development, the WRF model was initialized on 22 October at 00 UTC for a 72-hour period. This choice provided a 12-hour spin-up period prior to the depression stage and preceded storm genesis and hurricane status (according to Best Track) by 18 and 48 hours, respectively. Boundary conditions were defined using the 6-hourly European Centre for Medium-Range Weather Forecasting (ECMWF) Re-Analysis (ERA) Interim dataset. In addition to the control run, an experimental (no-terrain) simulation was performed to evaluate the sensitivity of the Caribbean terrain on storm genesis and hurricane

development. All model physics and settings remained consistent for the experimental simulation except the orography was reset to a constant value of 0.5 meters for all four domains (consistent with other mesoscale modeling studies on terrain sensitivity, e.g., Koch et al. 2001 and Brewer et al. 2013). Select fields from the control and the experimental simulations were evaluated against Best Track, composite satellite imagery, scatterometer winds, TRMM data, and CALIPSO Lidar in section 7.

The 22 October 00 UTC initialization time was also evaluated by Shen et al. (2013) in terms of storm genesis location and track predictability for the period of 22-29 October (Sandy's entire lifecycle). An early track error with the incipient vortex position (of 152 km), associated with a clockwise movement instead of the observed counterclockwise path, was discussed. A similar track and movement was found with the control and experimental simulations in this study. However, despite this initial disparity, the timeline of storm intensity for the control run was consistent when compared to observations (discussed below). And even though a closer positional correspondence is preferred at the outset of the simulation, observational evidence presented in section 6 demonstrates that the physical characteristics of vortex development in relation to the contributions from the surrounding environmental flows were preserved. In addition, two other initialization times were evaluated that straddled the chosen time by six hours (i.e., 21 October 18 UTC and 22 October 06 UTC, respectively). Neither an earlier or later initialization time resolved the clockwise track error and results varied slightly from the 22 October 00 UTC initialization (discussed below).

6. Model evaluation against observational data

a. Best Track

In Fig. 3 (a-c), the time series of the vortex minimum sea level pressure (MSLP), maximum tangential wind speed, and track error distance are depicted, respectively, for the control, the no-terrain experiment, and the two other initialization times (6 hours before/after the chosen time) against the Best Track compilation values. For MSLP and wind speed, values from all simulations show close correspondence with Best Track over the first 48 hours (until 24/00 UTC). Deviation thereafter occurs in concert with the onset of rapid deepening (24/06 UTC onward). For track error distance, values from the no-terrain simulation (black squares) show the largest discrepancies against Best Track early on—a result that may be characteristic of model build down in the absence of terrain. Later on, values of distance error from other simulations grow, excluding the control run, while those from the no-terrain run improve. Track error values for the control run remain consistent and within 250 km over the entire 72-hour simulation period. The value of 250 km is representative of the mean ensemble track error distance taken from sensitivity studies on track predictability performed for Hurricane Sandy (e.g., Shen et al. 2013; Bassill 2014).

In general, values from the control simulation (blue curve and squares) for all three variables show the best overall correspondence within and beyond the 48-hour mark. This result is encouraging as the disturbance undergoes rapid development (i.e., 24/06-12 UTC). After 24/16 UTC, the control simulation begins to deviate (with premature vortex weakening) compared to Best Track. Premature landfall with the Island of Jamaica may explain this disparity, even though track error distance values remained small. Another important finding related to wind speed arises in the Best Track value at 24/06-12 UTC.

During this time period, which was consistent with the onset of rapid deepening, the maximum wind speed from the control simulation is significantly larger than the value from Best Track and those reported for other runs. Despite this disparity, the deepening rate (in terms of MSLP with time) remains more closely captured by the control run. The closer alignment of speed values (Best Track versus the no-terrain simulation) is perhaps misleading, as the overall vortex structure (depicted by the no-terrain run) is not consistent when compared to the observed (discussed below).

b. Composite satellite imagery

Composite satellite (brightness) imagery is shown in Fig. 4 (center panels) for available time steps over Sandy's incipient to rapid deepening period (22-24 October, top to bottom). Vortex organization and concentricity are evident over time from the images with eye formation revealed later on 23 and 24 October. West-to-east brightness fragments extending from the Costa Rica shoreline are detectable over the first three time steps with enhanced consolidation shown in the fourth image. South-to-north brightness filaments are also observed crossing eastern Panama on the third time step and again in the fifth image. These brightness filaments are coincident with the low-level jet structures discussed in section 7. Rapid intensification is revealed in the final image 24/1100 UTC October.

Left and right panels of Fig. 4 illustrate 925 hPa streamlines overtop of coincident brightness for the control and the no-terrain simulation, respectively. Over the time sequence, vortex offset (in model streamlines versus brightness patterns) is evident for both the control and no-terrain run. However, concentricity from the control run (analogous with vortex deepening) is remarkably consistent with the brightness evolution over time. The west-to-east

elongation of the vortex from the no-terrain run, including (most importantly) the reduced streamline tightening in the core region (consistent with less tilt southwest-to-northeast), reveals less core intensification and organization (consistent with Fig. 3a and b, 24/06-12 UTC). Another important distinction between the simulations is the transition and curvature of the wind field on the west and south side of the developing vortex. For the no-terrain simulation, all images illustrate a north to broad westerly transition with less along-stream curvature. The control run depiction portrays a more consolidated and concave wind field along the same path. As discussed in the next section, this particular disparity in the wind field between the simulations is shown to underpin the primary differences in the vorticity in terms of environmental generation and vortex accretion.

c. Scatterometer surface winds

Similar to the brightness imagery comparison, the surface wind field from the control and no-terrain simulations was compared against WindSAT in Fig. 5 for available time steps over 22-24 October. Despite some disparity in vortex offset, consistent flow geometry and coincident accelerations are depicted between the control run and WindSAT. For the no-terrain simulation, streamlines show less concentricity where vortex tilt (reduced southwest-to-northeast) and elongation (greater west-to-east) characterize differences. Further evidence of concentrated west-to-east and south-to-north jet structures emanating from the Costa Rica shoreline and across Panama, respectively, is shown in WindSAT on 23 and 24 October. These features are again well captured in the control-run streamlines, as is their convergence on the southeast side of the developing vortex. The aforementioned jets are washed out in the

no-terrain simulation where a broad (more linear) cross continental flow from the west and south is portrayed in the surface wind field.

d. TRMM data

Images of maximum reflectivity from the control and no-terrain simulations are compared against TRMM precipitation in Fig. 6 for select time steps over 22-24 October. The time sequence of vortex spin-up is captured in the reflectivity patterns from both simulations, as are the areas of broad convection along the southern shoreline of Panama. However, the banding associated with reflectivity patterns in the no-terrain image sequence is inconsistent when compared to the observed. Careful inspection reveals discrepancies in all images, early on and during rapid development. At 22/1500 UTC (early development phase), the control run shows an obvious cyclonic structure on its south-southwest flank that is absent from the no-terrain simulation. At 23/2200 and 24/1000 UTC (rapid development onset phase), the no-terrain simulation shows extraneous linear banding that is spread west-to-east and the vortex-core signature is less definitive. The banded features shown in the no-terrain simulation also extend much further over surrounding landmass in the absence of the terrain. The vortex location is shifted westward in the image sequence of the control run, however, the banding intensity and vortex spin-up signature are well characterized in relation to TRMM.

e. CALIPSO Lidar

Figures 7 a-c illustrates the cloud (light blue, top panels), aerosol (orange, top panels), and water phase (middle panels) vertical structure from CALIPSO lidar Vertical Feature

Mask. The bottom panels depict coincident water-phase profiles from the control run[13]. The consistent feature in all three cross sections is the well-characterized ice structure, model versus CALIPSO. The horizontal extent and depth bears remarkable correspondence. The vertical extent and horizontal variation of the aerosol structure from CALIPSO in Fig. 7a is also nicely coupled to the behavior of the red line (planetary boundary layer height) from the model[14]. Evaluation of water phase collocation between CALIPSO and the model is only possible in the first cross section (Fig. 7a) and for small sub portions within the other two (Fig. 7 b and c), as beam attenuation often inhibits direct comparison. For the un-attenuated regions, water phase from the model appears to be over-predicted in some instances (e.g., Fig. 7b, 18-20°N) with co-existence but vertical misalignment at other times (e.g., Fig. 7c, 13-14°N). However, actual vapor amount (gkg^{-1}) is not provided by CALIPSO and therefore it is possible that disparities are not large.

f. Corozal, Panama soundings

Figure 8 illustrates a comparison of model-derived soundings from the control run to those observed at the Corozal, Panama site location for three 12 UTC time periods for 22-24 October. Upon inspection, the model largely captures the structural behavior of the temperature, moisture, and especially the wind field for all time periods. The strength of the surface temperature inversions is not replicated by the model on the 22nd and 23rd, however, the profile aloft is better resolved. The consistency in the wind field (through the column)

[13] Only three Caribbean overpass times were available for 22-24 October along the periphery of the developing vortex. As a consequence, differences between the control and no-terrain simulation were insignificant, and therefore only control-run profiles are shown against lidar.

[14] Note the vertical resolution of the lidar is finer than the model through the entire vertical depth and therefore point-to-point comparison (model versus lidar) requires careful inspection. In addition, the vertical extent of CALIPSO aerosol has been shown to be a good proxy for planetary boundary layer depth when the lower extent remains in contact with the ground surface. This proxy breaks down for elevated aerosol layers or when ground separation in excess 250 m occurs (Fearon et al. 2015).

between the model and observed inspires additional confidence. One implication for discrepancies may rest on the choice land use in the model. Corozal, Panama is an urban location with sample measurements taken in close proximity to the local airport.

7. Analysis and discussion

a. Synopsis of the precursor environment and identification of key mesoscale features

As described in part one, the precursor Sandy disturbance entered the eastern Caribbean on 18 October (Blake et al. 2013) and migrated west-southwest in a counterclockwise fashion while reaching tropical depression and storm status on 22nd at 12 and 18 UTC, respectively. Figure 9 illustrates a brightness composite of the clustering convection associated with the disturbance (and a near-coincident WindSAT image, inset) from 20 October 15 UTC near 71°W / 15°N. A weak rotational signature can be observed in the surface wind field. The manner in which the low-level spin initiated (e.g., bottom-up or top-down) was not discernable from available satellite imagery. However, rotation at 700 hPa was determined as early as 13 October by Lussier et al. (2015) as the disturbance moved across the North Atlantic.

As the disturbance moved west-southwest across the Caribbean from 20-23 October, the low-level pressure gradient tightened east-to-west ahead of and along its southern periphery (i.e., along the land-ocean interface from Costa Rica to Panama to Colombia). Two source mechanisms downstream, in contrast with the disturbance, were responsible for this gradient. The first was related to an area of transient high heights that migrated southward

along the eastern high terrain of Nicaragua and Costa Rica[15]. Figure 10 illustrates the southward progression of the higher heights from NARR 975 hPa for 21/18 and 22/06 UTC October, left and right, respectively. The second mechanism, which was non-transient and in-place for the duration of development, was associated with the daytime thermal gradient over the landmass, particularly over the mountain slopes with a northeastern aspect. The latter mechanism behaved much like a mountain-plains solenoid (MPS) circulation where cooler morning valley-surface air is forced upslope in response to nonuniform and tilted surface heating (Koch et al. 2001; Lin 2007). In succession, both mechanisms promoted a concave ring (or perimeter, see Fig. 11 yellow ribbon) of high pressure—a result of hydrostatic thickness increases above the near surface lower density/pressure. The mass field between this perimeter and the developing disturbance became a curved channel of strong westerly momentum wherein vorticity generation was maximized (Fig. 11, westerly jet channel or WJC symbol, red arrows). This jet structure amplified gradually over the first 24 hours (22-23 October) and intensified more rapidly later on the 23 and early on the 24 October. This jet was augmented and slightly redirected (from westerly to northwesterly) during the evening hours in response to independent nocturnal jet structure, above the insulated surface layer, that emanated from the Costa Rica shoreline (Fig. 11, black arrow). As the westerly momentum and vorticity generation within maximized on 23 October, it was met by southerly momentum that crossed Panama from the northeastern Pacific (Fig. 11, southerly jets or SJ symbol, red arrows). The latter manifested from two broad areas of clustered convection over northeastern Pacific (Fig. 11, white translucent ovals). One spanned north-south near offshore western Colombia and the other took a more east-west orientation along

[15] The alongshore height rises were a downstream signal of strong upper-level convergence associated with a subtropical jetlet over the southern Gulf of Mexico two days earlier (described in part one, section 4f).

the Costa Rica/Panama southern shoreline. Two branches of southerly momentum entered the Caribbean through the zonal gaps in the Panamanian terrain and partially merged just prior to their convergence with the curved westerly jet on the southeast side of the developing vortex. Rapid intensification of tropical storm Sandy ensued soon after consolidated vorticity (from the west and south) entered the vortex core on 23-24 October (discussed below).

b. Landmass/terrain-induced mesoscale features

The initial alongshore perimeter of higher heights (representative of mesoscale ridging) that propagated southeastward transitioned to even higher heights during the afternoon that opposed the lowering heights associated with the deepening disturbance over the interior sea. This was manifestation primarily of the daytime heating over the high terrain as part of a mountain-plains solenoid circulation. Figure 12 a and b illustrate the temperature difference (on the 304 K surface) between the control and the no-terrain simulation at 22 UTC on 22 and 23 October, top to bottom, respectively. Positive values depicted are a reflection of the warmer afternoon temperatures produced by the control run. The migration of the warmer air from the heated mountain slopes toward the sea is a thermal signal associated with the MPS circulation. The sounding profiles shown in Fig. 13c and d (solid light blue point locations in Fig 12) offer further evidence of the MPS structure, where each depicts a shallow surface adiabatic lapse rate (consistent with a heated slope), a near-surface northeasterly (upslope) flow, and slightly more elevated flow reversal (from the west-southwest). The net result of the MPS circulation is the solenoidal vorticity that is produced downstream of the mountain. However, perhaps more important in this situation, is the local higher pressure built aloft (just above the heated slope). The latter builds upward and outward

toward the sea amplifying the pressure gradient imposed on the curved channel that straddles the terrain and the developing disturbance. The alongshore ridging also provides downstream shear protection for the developing disturbance, as one could envision how upstream flow from the west and or south would be redirected temporarily as it encounter the ridge. The terrain barrier itself also blocks upstream flow and provides shear protection for the vortex (e.g., Schar and Durran 1997).

Preceding the daytime MPS circulation on 22 October, a low-level nocturnal jet was observed in the control run simulation between the hours of 06-12 UTC. Fig. 13a and b (solid purple point locations in Fig. 12) illustrate the vertical profiles of two distinct examples that emanated from the alongshore, eastern slopes of Costa Rica. Note the near-surface shallow inversion layer (~100-200 m) as portrayed by the temperature structure and the moderate westerly momentum (jet) atop. The manifestation of the jet structure occurred in concert with upstream mountain blocked northerly flow redirected westerly atop of the inversion. The offshore surge of momentum converged with the WJC flow (to be illustrated) and temporarily enhanced vorticity production in that zone. Figure 14 (left panel, control run) illustrates a plan view of the nocturnal jet feature exiting the Costa Rica coast and its convergence with the WJC offshore, which is ill-defined in the no-terrain simulation (right panel).

c. Description of low-level curved westerly jet channel (WJC)

As described above, the curved westerly jet channel manifested between higher pressure adjacent to the near-shore mountains (in response to the MPS circulation) and the lower pressure over the sea associated with the tropical disturbance. Curvature and

downstream acceleration of this airstream gradually created and transported vorticity to the developing vortex. The curved mass field built by the pressure field (mountain versus disturbance) was critical for the vortex development, as vorticity was continuously generated within the channel and carried downstream to the inflow region. Figure 15 illustrates the time integral of the positive relative vorticity (22/00 UTC – 24/12 UTC) from the control and no-terrain simulation, left and right panels, respectively. There is a remarkable difference in the banding structure of the vorticity pattern revealed between the two simulations, especially in the WJC region, the vortex core, and in the vicinity of the SJ. Examination of the WJC region from the control run reveals a concave curved signature (between the landmass/terrain and the disturbance) where the vorticity banding grows inward and northwest-to-southeast-to-north toward the vortex inflow (southeast side). The vorticity generation through this zone and its downstream accretion by the vortex is hypothesized to be the primary mechanism for storm intensification. Such WJC is absent from the no-terrain depiction. Vorticity grows inward, however, the progressive northwest-to-southeast-to-north trajectory of banding is missing. Rather, comparable banding exists on the southern side of the vortex in the no-terrrain simulation with a progressive nature oriented south-to-northeast—a signature that resembles a mature mid-latitude vortex. The latter statement is further illustrated in Fig. 16. Here, a three-panel comparison of the control and no-terrain simulations (side-by-side) for three time intervals where the top panel (24/12 UTC) is representative of vortex rapid development, the middle panel (24/00 UTC) shows the wind field prior to rapid-phase onset by ~4-5 hours, and the bottom panel (23/18 UTC) reveals later stage tropical storm status. The curved northwest-to-southeast flow versus the more linear west-to-east flow on the southwest side of vortex (control versus no-terrain, respectively) is shown and grows through

the time sequence. The vortex tilt and elongation differences (southwest-to-northeast versus west-to-east, respectively) are characteristic of the former compared flow descriptions.

d. Description of low-level southerly jet (SJ) and near-inflow convergence zone

During the primary period of interest, from 22/00 through 24/12 UTC, areas of persistent, deep convection blossomed over the northeastern Pacific near offshore Costa Rica, Panama, and Colombia (see evolution in TRMM image sequence, Fig. 6, center panel). These areas gradually evolved and took a banded orientation (northwest-to-southeast) along the southern shorelines of Costa Rica/Panama. Upstream low-level airflow from the west-northwest was funneled between the convection bands and the mountain barrier to the north and followed a northwest-to-southeast-to-northeast trajectory—a scenario similar to the WJC but on the southern flank of the mountains. The cyclonic curvature associated with this channel, similar to the WJC, maximized vorticity generation as the airstream wrapped northward cyclonically and entered the southwestern Caribbean through Panamanian sierra gaps. The maximized vorticity signature associated with the curved southerly momentum is illustrated in the control (Fig. 15, left panel, along the southern side of the Costa Rica-western Panama mountains and northward). Over the same location, a much weaker and less concentrated signal is reveal in the no-terrain simulation (Fig. 15, right panel).

A second, more linear southerly jet from the northeastern Pacific was also operative during this period. This momentum achieved acceleration as it was funneled northward between the eastern extent of the banded convection (over the northeastern Pacific) and near-shore Andes Mountains of western Colombia. The jet crossed eastern Panama and entered the Caribbean along a path similar to a Choco jet. Less vorticity developed in association with

this airstream, although some cyclonic curvature was imposed as it entered the Caribbean (near the Panamanian/Colombian border, Fig. 15, control run, left panel). Upon crossing the Panamanian coast, the two aforementioned southerly jets partially converged as they continued north and met the flow associated with the WJC on the southeast side of the vortex (Fig. 15, bottom-top, left panels). A different scenario is portrayed with the no-terrain simulation with much less vorticity and flow concentration. Mountain absence yields more linear and broad (west-to-east) flow crossing Costa Rica and Panama. Curvature is lost under this scenario and hence so is vorticity. The vorticity pattern in Fig. 15 (in the control run) shows a concentrated band crossing the Panama Coast between 80 and 78°W oriented southwest to northeast that converges with the curved westerly jet near the inflow region (~ 14°N / 76°W) with downstream inflow just north and directed radially inward (i.e., note the notch in the vorticity pattern near ~15.5°N / 77°W, left panel). Weaker vorticity patterns exist in the no-terrain depiction and flow convergence exists further north and out ahead of the main vortex with inflow notching ill-defined.

f. Core structure and upstream flow origin

The vertical structure of vorticity and horizontal winds across the vortex core for the control and no-terrain simulation are depicted in Fig. 17, left and right, respectively, for 24/12 UTC, and 24/00UTC, and 23/18 UTC (top to bottom). The difference in vorticity accretion at 24/12 UTC (top panels) is remarkable and clearly demonstrates a developmental difference between the simulations during the rapid phase period. The control run shows a tight, concentric, and deep cyclonic column of vorticity with relaxed central winds (indicative of eye center) and lateral wind convergence and divergence, right and left respectively. The

low-level inflow, on the right side, in the control run simulation illustrates strong convergence directed radially inward. The aforementioned features are near absent from the no-terrain simulation at 24/12 UTC and the wind field is broadly accelerative through the column. Inspecting the earlier time periods shown in Fig. 17, a narrowing column of convergence (and vertical accretion of vorticity) is discernable in the control run images (left middle and bottom panels). The vorticity also appears to build up from the surface in the control run time sequence. A broader wind field and hints of organization exist in the earlier time sequences of the no-terrain simulation, but vorticity accretion never materializes.

Fig. 18 further corroborates the former core cross sections. Here, the core-averaged vorticity anomalies (the inner 3° associated with the core vortex minus outer surrounding 3°) by time versus pressure are shown for the control and no-terrain simulations. Preceding and during rapid development (24/12 UTC or hour 60) remarkable differences in vorticity accretion are evident between the simulations. The lack of environmental flow curvature and vorticity in the no-terrain simulation is clearly portrayed via the reduced vorticity accretion pattern in the no-terrain depiction.

The overall vortex circulation structure and environmental upstream flow differences between the simulations are presented in Fig. 19. Here, 30 coincident back trajectories attempts for the control and no-terrain simulations are depicted, left and right maps, respectively. Red lines exemplify three case examples amongst other attempts shown in blue. For the control run, upstream flow is comprised of westerly and southern momentum that enters a tightly developing vortex on the southeast side along a pathway directed radially inward. For the no-terrain run, upstream flow is from the southwest and southeast into a

broad elongated vortex with limited inward contraction. The parcel pathways re-emphasize the important differences in upstream curvature and its absence in the no-terrain simulation.

8. Conclusions

The goal of this study was to examine the precursor hurricane environment for the case of Hurricane Sandy and the potential role of the terrain (and the associated dynamics) on vortex development and intensification. To this end, two numerical simulations were performed, a control run and no-terrain experiment where the latter was used to evaluate the sensitivity of the terrain. Several mesoscale features were detected in the mass field of the control simulation and examined across the southwestern Caribbean Sea including 1) transient low-level mass perturbations that propagated southward in response to an upstream mid-latitude jetlet, 2) a nocturnal jet along the Costa Rica mountains/shoreline, 3) the mountain-plains solenoid circulation along the northeastern mountain slopes of Costa Rica, Panama and Colombia, and 4) broad areas of convection south of Panama/Costa Rica and west of Colombia. Each feature in connection with the nearby complex terrain was shown to be influential in initiating flow curvature and vorticity. Two distinct, curved jet features were identified. First, a WJC that formed between the developing disturbance and the concave landmass/terrain of Nicaragua/Costa Rica/Panama within which vorticity was maximized and carried to the vortex inflow region (southeast side of the storm). The daytime MPS circulation amplified the pressure gradient offshore away from the terrain where through this flow traveled. Second, a two-branch southerly jet formed south of Panama/Costa Rica, over the northeastern Pacific. The western branch of this southerly momentum also followed a curved path, similar to the WJC, between banded convection and the southern flank of the

Costa Rican mountains. It met additional southerly momentum, accelerating north between banded convection and the Andes Mountains of Colombia. The two branches of southerly momentum merged north of Panama and then converged with the upstream WJC near the inflow region where a distinct notch was initiated in the vorticity field just prior to vortex rapid intensification.

The role of the Caribbean terrain in association with the aforementioned mesoscale features was shown to be instrumental on the vortex development. Comparisons of a no-terrain numerical simulation against the control run revealed distinct developmental differences in vortex geometry, size, and tilt over the spin-up time period. The evolution of these attributes inherently links back to the surrounding terrain, which in this case, cocooned the incipient vortex and organized the structure of the environmental mass field and flow orientation within it.

Given the influential nature of the terrain on the Hurricane Sandy's development, as shown in this study, one has to wonder how this result translates to other tropical cyclones. Is some degree of continental proximity a requirement (or at least a key ingredient) for tropical cyclone development in combination with other well documented environmental factors (e.g., low vertical wind shear; a warm sea surface, a deep moist column etc..)? The primary role of the continent in this case appears to rest on the surrounding mass field organization, specifically the curvature of it, and the resultant production of environmental vorticity. This question may be important toward addressing why some tropical cyclones develop and others do not despite the presence of similar environmental conditions. Examination of several other storm scenarios is necessary to fully evaluate these questions, although if some degree of

continental proximity proves to be a consistent influential factor, the implications may prove to be invaluable for hurricane prediction.

Acknowledgements: Author Kaplan acknowledges support received from a Desert Research Institute IPA Grant. We also thank Wallace Hogsett and Elizabeth A. Ritchie for their insight on tropical cyclone development and personal correspondence. High-performance computing resources were provided by Timothy J. Brown and the Desert Research Institute's Program for Climate, Ecosystem and Fire Applications. The authors also wish to thank Erin C. Gleason for her support and assistance with graphics.

References

Bassill, N. P. (2014). Accuracy of early GFS and ECMWF Sandy (2012) track forecasts: Evidence for a dependence on cumulus parameterization. *Geophysical Research Letters*, 3274–3281. http://doi.org/10.1002/2014GL059839.

Betts, A. K. (1982). Saturation Point Analysis of Moist Convective Overturning. *Journal of the Atmospheric Sciences*. http://doi.org/10.1175/1520-0469(1982)039<1484:SPAOMC>2.0.CO;2

Betts, A. K. (1986). A new convective adjustment scheme. Part I: Observational and theoretical basis. *Quarterly Journal of the Royal Meteorological Society*, *112*(473), 677–691. http://doi.org/10.1002/qj.49711247307

Betts, A. K., & Miller, M. J. (1986). A new convective adjustment scheme. Part II: Single column tests using GATE wave, BOMEX, ATEX and arctic air-mass data sets. *Quarterly Journal of the Royal Meteorological Society*, *112*(473), 693–709. http://doi.org/10.1002/qj.49711247308

Blake, E. S., Kimberlain, T. B., Berg, R. J., Cangialosi, G. P., & Beven II, J. L. (2013). *Tropical cyclone report: Hurricane Sandy. National Hurricane Center Tech. Rep. AL182012*. Retrieved from www.nhc.noaa.gov/data/tcr/AL182012_Sandy.pdf.

Brewer, M. C., Mass, C. F., & Potter, B. E. (2013). The West Coast Thermal Trough: Mesoscale Evolution and Sensitivity to Terrain and Surface Fluxes. *Monthly Weather Review*, *141*(8), 2869–2896. http://doi.org/10.1175/MWR-D-12-00305.1

Charney, J. G., & Eliassen, A. (1964). On the growth of the hurricane depression. *Journal of Atmospheric Sciences*, *21*, 68–75.

Chen, F., & Dudhia, J. (2001). Coupling an Advanced Land Surface–Hydrology Model with the Penn State–NCAR MM5 Modeling System. Part I: Model Implementation and Sensitivity. *Monthly Weather Review*, *129*(4), 569–585. http://doi.org/10.1175/1520-0493(2001)129<0569:CAALSH>2.0.CO;2

Dudhia, J. (1989). Numerical Study of Convection Observed during the Winter Monsoon Experiment Using a Mesoscale Two-Dimensional Model. *Journal of the Atmospheric Sciences*, *46*(20), 3077–3107. http://doi.org/10.1175/1520-0469(1989)046<3077:NSOCOD>2.0.CO;2

Dunkerton, T. J., Montgomery, M. T., & Wang, Z. (2009). Tropical cyclogenesis in a tropical wave critical layer: easterly waves. *Atmospheric Chemistry and Physics Discussions*, *8*(v), 11149–11292. http://doi.org/10.5194/acpd-8-11149-2008

Ek, M. B. (2003). Implementation of Noah land surface model advances in the National Centers for Environmental Prediction operational mesoscale Eta model. *Journal of Geophysical Research*, *108*(D22), 8851. http://doi.org/10.1029/2002JD003296

Emanuel, K. A. (1986). An air-sea interaction theory for tropical cyclones.Part I: Steady-state maintenance. *Journal of Atmospheric Sciences*, *43*, 585–604.

Emanuel, K. A. (1989). The Finite-Amplitude Nature of Tropical Cyclogenesis. *Journal of the Atmospheric Sciences*. http://doi.org/10.1175/1520-0469(1989)046<3431:TFANOT>2.0.CO;2

Emanuel, K. A. (1991). The theory of Hurricanes. *Annu. Rev. Fluid Mech*, *23*(1982), 179–96.

Fearon, M. G., Brown, T. J., & Curcio, G. M. (2015). Establishing a national standard methodology for operational mixing height determination, *3*(15), 1–48.

Galarneau, T. J., Davis, C. A., & Shapiro, M. A. (2013). Intensification of Hurricane Sandy (2012) through Extratropical Warm Core Seclusion. *Monthly Weather Review*, *141*(12), 4296–4321. http://doi.org/10.1175/MWR-D-13-00181.1

Gray, W. M. (1967). The mutual variation of the wind, shear, and baroclinicity in the cumulus convective atmosphere of the hurricane. *Monthly Weather Review*, *95*, 55–73.

Gray, W. M. (1975). *Tropical cyclone genesis*. Dept. of Atmospheric Sciences Pap. 234, Colorado State University, 121 pp.

Gray, W. M. (1998). Meteorology , and Atmospheric Physics The Formation of Tropical Cyclones. *Meteorology and Atmospheric Physics*, *67*, 37–69. http://doi.org/10.1007/BF01277501

Harr, P. A., & Elsberry, R. L. (1996). Structure of a Mesoscale Convective System Embedded in Typhoon Robyn during TCM-93. *Monthly Weather Review*, *124*(4), 634–652. http://doi.org/10.1175/1520-0493(1996)124<0634:SOAMCS>2.0.CO;2

Hendricks, E. a., Montgomery, M. T., & Davis, C. a. (2004). The Role of "Vortical" Hot Towers in the Formation of Tropical Cyclone Diana (1984). *Journal of the Atmospheric Sciences*, *61*(1984), 1209–1232. http://doi.org/10.1175/1520-0469(2004)061<1209:TROVHT>2.0.CO;2

Janjić, Z. I. (1994). The Step-Mountain Eta Coordinate Model: Further Developments of the Convection, Viscous Sublayer, and Turbulence Closure Schemes. *Monthly Weather Review*. http://doi.org/10.1175/1520-0493(1994)122<0927:TSMECM>2.0.CO;2

Janjić, Z. I. (2001). *Nonsingular Implementation of the Mellor-Yamada Level 2.5 Scheme in the NCEP Meso model*. Camp Springs, MD.

Kasahara, A. (2000). On the origin of cumulus parameterization for numerical prediction models. In D. A. Randall (Ed.), *General Circulation Model Development* (pp. 199–224). San Diego: Academic Press.

Koch, S. E., Zhang, F., Kaplan, M. L., Lin, Y.-L., Weglarz, R., & Trexler, C. M. (2001). Numerical Simulations of a Gravity Wave Event over CCOPE. Part III: The Role of a

Mountain–Plains Solenoid in the Generation of the Second Wave Episode. *Monthly Weather Review*, *129*(5), 909–933. http://doi.org/10.1175/1520-0493(2001)129<0909:NSOAGW>2.0.CO;2

Lackmann, G. M. (2014). Hurricane Sandy before 1900 and after 2100. *Bulletin of the American Meteorological Society*, *96*(4), 547–560. http://doi.org/10.1175/BAMS-D-14-00123.1

Landsea, C. W., Hagen, A., Bredemeyer, W., Carrasco, C., Glenn, D. A., Santiago, A., … Dickinson, M. (2014). A Reanalysis of the 1931–43 Atlantic Hurricane Database. *Journal of Climate*, *27*(16), 6093–6118. http://doi.org/10.1175/JCLI-D-13-00503.1

Lewis, J. M., Fearon, M. G., & Klieforth, H. E. (2012). Herbert Riehl: Intrepid and Enigmatic Scholar. *Bulletin of the American Meteorological Society*, *93*(7), 963–985. http://doi.org/10.1175/BAMS-D-11-00224.1

Lin, Y.-L. (2007). *Mesoscale Dynamics* (First Edit). Cambridge, U.K. 630 pp.

Lussier, L. L., Rutherford, B., Montgomery, M. T., Boothe, M. A., & Dunkerton, T. J. (2015). Examining the Roles of the Easterly Wave Critical Layer and Vorticity Accretion during the Tropical Cyclogenesis of Hurricane Sandy. *Monthly Weather Review*, *143*(5), 1703–1722. http://doi.org/10.1175/MWR-D-14-00001.1

McBride, J. L., & Zehr, R. (1981). Observational Analysis of Tropical Cyclone Formation. Part II: Comparison of Non-Developing versus Developing Systems. *Journal of the*

Atmospheric Sciences, *38*(October), 1132–1151. http://doi.org/10.1175/1520-0469(1981)038<1132:OAOTCF>2.0.CO;2

Mellor, G. L., & Yamada, T. (1974). A Hierarchy of Turbulence Closure Models for Planetary Boundary Layers. *Journal of the Atmospheric Sciences*, *31*(7), 1791–1806. http://doi.org/10.1175/1520-0469(1974)031<1791:AHOTCM>2.0.CO;2

Mellor, G. L., & Yamada, T. (1982). Development of a turbulence closure model for geophysical fluid problems. *Reviews of Geophysics*, *20*(4), 851. http://doi.org/10.1029/RG020i004p00851

Merrill, R. T. (1988). Characteristics of the Upper-Tropospheric Environmental Flow around Hurricanes. *Journal of the Atmospheric Sciences*, *45*(11), 1665–1677. http://doi.org/10.1175/1520-0469(1988)045<1665:COTUTE>2.0.CO;2

Mlawer, E. J., Taubman, S. J., Brown, P. D., Iacono, M. J., & Clough, S. A. (1997). Radiative transfer for inhomogeneous atmospheres: RRTM, a validated correlated-k model for the longwave. *Journal of Geophysical Research*, *102*(D14), 16663. http://doi.org/10.1029/97JD00237

Moeng, C.-H., & Wyngaard, J. C. (1988). Spectral Analysis of Large-Eddy Simulations of the Convective Boundary Layer. *Journal of the Atmospheric Sciences*. http://doi.org/10.1175/1520-0469(1988)045<3573:SAOLES>2.0.CO;2

Montgomery, M. T., & Farrell, B. F. (1993). Tropical Cyclone Formation. *Journal of the Atmospheric Sciences*. http://doi.org/10.1175/1520-0469(1993)050<0285:TCF>2.0.CO;2

Montgomery, M. T., Nicholls, M. E., Cram, T. a., & Saunders, a. B. (2006). A Vortical Hot Tower Route to Tropical Cyclogenesis. *Journal of the Atmospheric Sciences*, *63*(1997), 355–386. http://doi.org/10.1175/JAS3604.1

Montgomery, M. T., & Smith, R. K. (2014). Paradigms for tropical cyclone intensification. *Australian Meteorological and Oceanographic Journal*, *64*, 37–66.

Mozer, J. B., & Zehnder, J. A. (1996a). Lee vorticity Production by Large-Scale Tropical Mountain Ranges. Part I: Eastern North Pacific Tropical Cyclogenesis. *Journal of the Atmospheric Sciences*, *53*(4), 521–538. http://doi.org/10.1175/1520-0469(1996)053<0521:LVPBLS>2.0.CO;2

Mozer, J. B., & Zehnder, J. A. (1996b). Lee vorticity Production by Large-Scale Tropical Mountain Ranges. Part II: A Mechanism for the Production of African Waves. *Journal of the Atmospheric Sciences*, *53*(4), 539–549. http://doi.org/10.1175/1520-0469(1996)053<0539:LVPBLS>2.0.CO;2

Munsell, E. B., & Zhang, F. (2014). Prediction and uncertainty of Hurricane Sandy (2012) explored through a real-time cloud-permitting ensemble analysis and forecast system assimilating airborne Doppler radar observations. *Journal of Advances in Modeling Earth Systems*, *6*(1), 38–58. http://doi.org/10.1002/2013MS000297

Ooyama, K. (1964). A dynamical model for the study of tropical cyclone development. *Geofis Int*, *4*, 187–198.

Ooyama, K. (1969). Numerical simulation of the life cycle of tropical cyclones. *Journal of Atmospheric Sciences*, *26*, 3–40.

Ooyama, K. (1982). Conceptual evolution of the theory and modeling of the tropical cyclone. *Journal of Meteorology Society Japan*, *60*, 369–379.

Poveda, G., & Mesa, O. J. (2000). On the existence of Lloró (the rainiest locality on Earth): Enhanced ocean-land-atmosphere interaction by a low-level jet. *Geophysical Research Letters*, *27*(11), 1675–1678. http://doi.org/10.1029/1999GL006091

Raymond, D. J., & Sessions, S. L. (2007). Evolution of convection during tropical cyclogenesis. *Geophys. Res. Lett.*, *34*(6), L06811. http://doi.org/10.1029/2006GL028607

Riehl, H., & Malkus, J. S. (1958). On the heat balance in the equatorial trough zone. *Geophyisca*, *6*, 503–538.

Riehl, H., & Simpson, J. (1979). On the heat balance in the equatorial trough, revisited. *Contributions to Atmospheric Physics*, *52*, 287–305.

Riehl, H., Yeh, T. C., Malkus, J. S., & la Seur, N. E. (1951). The north-east trade of the Pacific Ocean. *Quarterly Journal of the Royal Meteorological Society*, *77*(334), 598–626. http://doi.org/10.1002/qj.49707733405

Ritchie, E. A. (1995). *Mesoscale aspects of tropical cyclone formation*. Ph.D. Dissertation, Monash University, Melbourne, Australia, 167 pp.

Ritchie, E. A. (2003). Some Aspects of Midlevel Vortex Interaction in Tropical Cyclogenesis. *Meteorological Monographs*, *29*(51), 165. http://doi.org/10.1175/0065-9401(2003)029<0165:CSAOMV>2.0.CO;2

Ritchie, E. A., & Holland, G. J. (1997). Scale Interactions during the Formation of Typhoon Irving. *Monthly Weather Review*, *125*(7), 1377–1396. http://doi.org/10.1175/1520-0493(1997)125<1377:SIDTFO>2.0.CO;2

Schär, C., & Durran, D. R. (1997). Vortex Formation and Vortex Shedding in Continuously Stratified Flows past Isolated Topography. *Journal of the Atmospheric Sciences*, *54*, 534–554. http://doi.org/10.1175/1520-0469(1997)054<0534:VFAVSI>2.0.CO;2

Shamrock, W. C., Klemp, J. B., Dudhia, J., Gill, D. O., Barker, D. M., Duda, M. G., … Powers, J. G. (2008). *A Description of the Advanced Research WRF Version 3*. Boulder, CO.

Shen, B.-W., DeMaria, M., Li, J.-L. F., & Cheung, S. (2013). Genesis of Hurricane Sandy (2012) simulated with a global mesoscale model. *Geophysical Research Letters*, *40*(18), 4944–4950. http://doi.org/10.1002/grl.50934

Simpson, J., & Halverson, J. (1998). On the role of "hot towers" in tropical cyclone formation. *Meteorol. Atmos. Phys.*, *35*, 15–35. http://doi.org/10.1007/BF01277500

Thompson, G., Field, P. R., Rasmussen, R. M., & Hall, W. D. (2008). Explicit Forecasts of Winter Precipitation Using an Improved Bulk Microphysics Scheme. Part II: Implementation of a New Snow Parameterization. *Monthly Weather Review*, *136*(12), 5095–5115. http://doi.org/10.1175/2008MWR2387.1

Thompson, G., Rasmussen, R. M., & Manning, K. (2004). Explicit Forecasts of Winter Precipitation Using an Improved Bulk Microphysics Scheme. Part I: Description and Sensitivity Analysis. *Monthly Weather Review*, *132*(2), 519–542. http://doi.org/10.1175/1520-0493(2004)132<0519:EFOWPU>2.0.CO;2

Torn, R. D., Whitaker, J. S., Pegion, P., Hamill, T. M., & Hakim, G. J. (2014). Diagnosis of the Source of GFS Medium-Range Track Errors in Hurricane Sandy (2012). *Monthly Weather Review*, *143*(1), 132–152. http://doi.org/10.1175/MWR-D-14-00086.1

Vaughan, M. A., Young, S. A., Winker, D. M., Powell, K. A., Omar, A. H., Liu, Z., … Hostetler, C. A. (2004). Fully automated analysis of space-based lidar data: an overview of the CALIPSO retrieval algorithms and data products. In U. N. Singh (Ed.), *Remote Sensing* (pp. 16–30). International Society for Optics and Photonics. http://doi.org/10.1117/12.572024

Wang, C., & Lee, S. K. (2007). Atlantic warm pool, Caribbean low-level jet, and their potential impact on Atlantic hurricanes. *Geophysical Research Letters*, *34*(2), 1–5. http://doi.org/10.1029/2006GL028579

Wang, Z., Montgomery, M. T., & Dunkerton, T. J. (2010a). Genesis of Pre–Hurricane Felix (2007). Part I: The Role of the Easterly Wave Critical Layer. *Journal of the Atmospheric Sciences*, *67*(6), 1711–1729. http://doi.org/10.1175/2009JAS3420.1

Wang, Z., Montgomery, M. T., & Dunkerton, T. J. (2010b). Genesis of Pre–Hurricane Felix (2007). Part II: Warm Core Formation, Precipitation Evolution, and Predictability. *Journal of the Atmospheric Sciences*, *67*(6), 1730–1744. http://doi.org/10.1175/2010JAS3435.1

Willoughby, H. E., Clos, J. A., & Shoreibah, M. G. (1982). Concentric eye walls, secondary wind maxima and the evolution of the hurricane vortex. *Journal of Atmospheric Sciences*, *39*, 395–411.

Yanai, M. (1964). Formation of tropical cyclones. *Reviews of Geophysics*, *2*, 367–414.

Zawislak, J., & Zipser, E. J. (2014). Analysis of the Thermodynamic Properties of Developing and Nondeveloping Tropical Disturbances Using a Comprehensive Dropsonde Dataset. *Monthly Weather Review*, *142*(3), 1250–1264. http://doi.org/10.1175/MWR-D-13-00253.1

Zipser, E. J. (2003). Some Views On “Hot Towers” after 50 Years of Tropical Field Programs and Two Years of TRMM Data. *Meteorological Monographs*, *29*(51), 49. http://doi.org/10.1175/0065-9401(2003)029<0049:CSVOHT>2.0.CO;2

LIST OF TABLES

Table 1. Description of observational data used in this study.

Dataset	Description
Best Track	Data on geographical position (deg), minimum sea-level pressure (mb), and maximum wind speed (kts) for (tropical storm and hurricane) Sandy for the period of October 21-26, 2012 were extracted from the Best Track HURricane DATabase (HURDAT2; Landsea et al. 2013).
CALIPSO Lidar	National Aeronautics and Space Administration's (NASA)'s Cloud-Aerosol Lidar and Infrared Pathfinder Satellite Observation (CALIPSO) profiles (Vertical Feature Mask, VFM version 3.01) were compared to model cross sections for coincident times. This product was chosen for its simplicity, as it is a post-processed version of the aerosol backscatter and provides cloud depth identification including ice, water, and mixed-phased determination. The horizontal footprint of the lidar beam is 5 km within which are 15 individual profiles at a horizontal resolution of 333 m. The vertical resolution of each profile is 30 m within the first 8 km of the surface and 60 m between 8 and 20 km. Additional details regarding the CALIPSO system and data can found in Vaughan et al. (2004). The term lidar and CALIPSO are synonymous in this study and are used interchangeably in the text.
Composite Satellite Imagery	Post-processed composite satellite imagery available from the Navel Research Laboratory (NRL)'s Tropical Cyclone Page (TCP) was compared against model output for coincident snapshots for position and intensity assessment. Products used in study included composite brightness imagery from Geostationary visible (~ 1 km), Infrared (~ 4 km), and several microwave channels. Additional information on all data is available from the NRL-TCP web page (NRL-TPC 2015).
Scatterometer Surface Winds	Derived surface wind speed and direction from microwave retrievals (25 km), including data from WindSAT, OceanSAT, and ASCAT were compared to coincident 10 m model wind data for evaluation of storm position and circulation patterns. Image data were obtained from the National Environmental Satellite, Data, and Information Service (NESDIS 2015). The WindSAT acronym is used as a "catchall" term for all scatterometer wind data referenced in the text.
TRMM Data	Tropical Rainfall Measuring Mission (TRMM) data was acquired from the NASA-Goddard Earth Sciences Data and Information Center, GIOVANNI Interactive Visualization and Analysis Tool (version 4.16). Data have a 0.25° resolution and represent accumulated rainfall every 3 hours (version 3B42_v7; NASA 2015) and were compared to model estimated reflectivity for available coincident times.

NARR Data	North American Regional Reanalysis (NARR) at 32 km horizontal resolution from the National Oceanic Atmospheric Administration's National Operational Model Archive and Distribution System (NOMADS) for 925 hPa was used to illustrate height and wind patterns over the Caribbean zone in advance of numerical simulation period.

LIST OF FIGURES

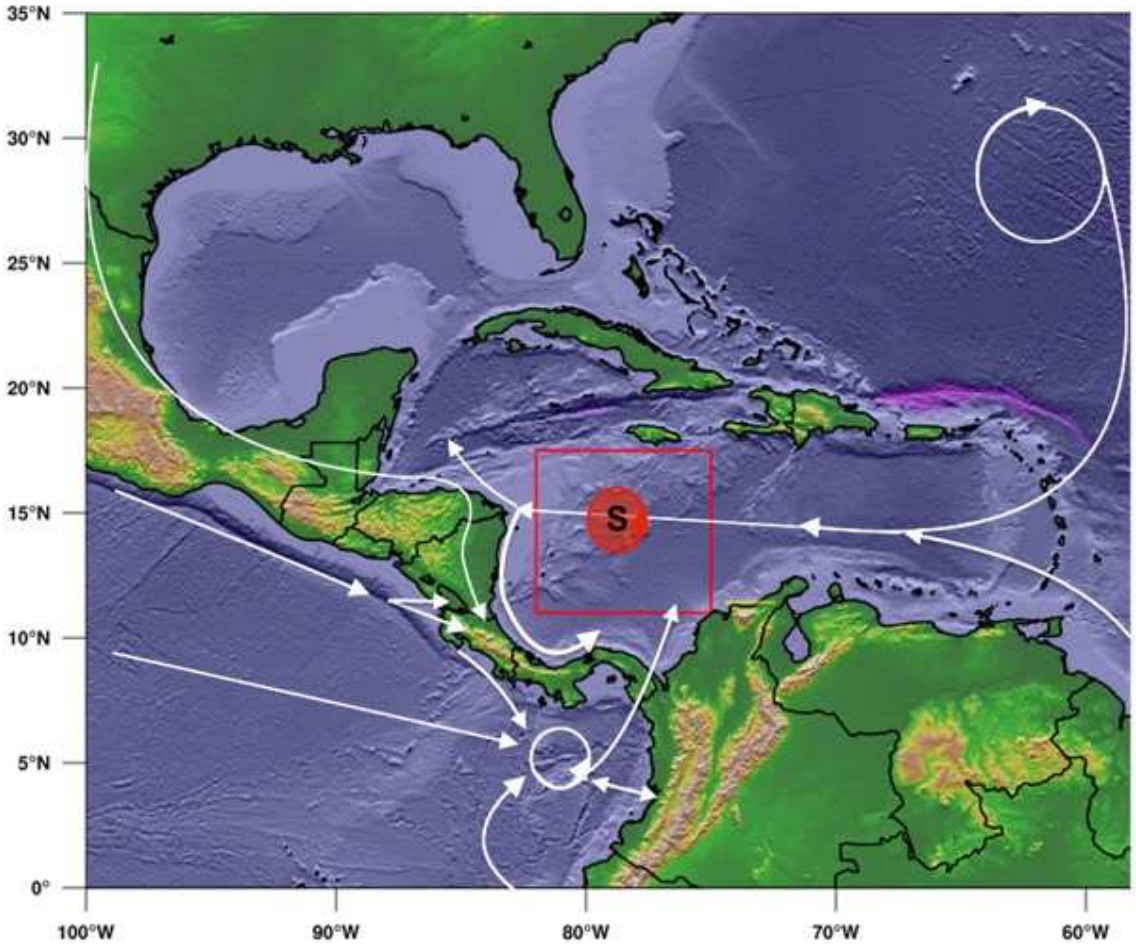

Figure 1. Caricature depiction of transient and semi-permanent subsynoptic scale flows across the Caribbean Basin.

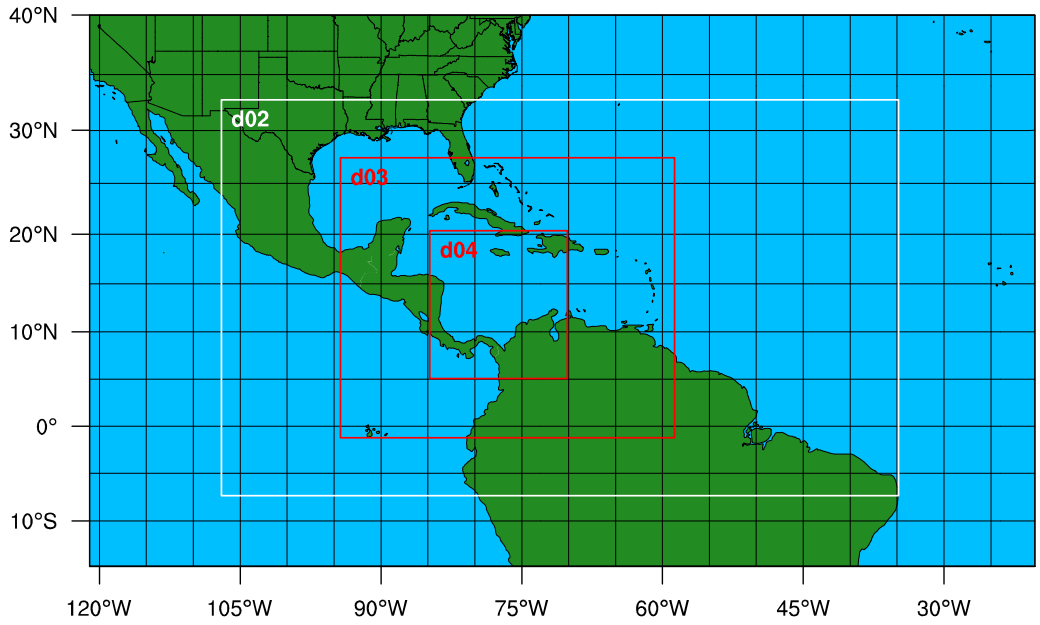

iment simulations.

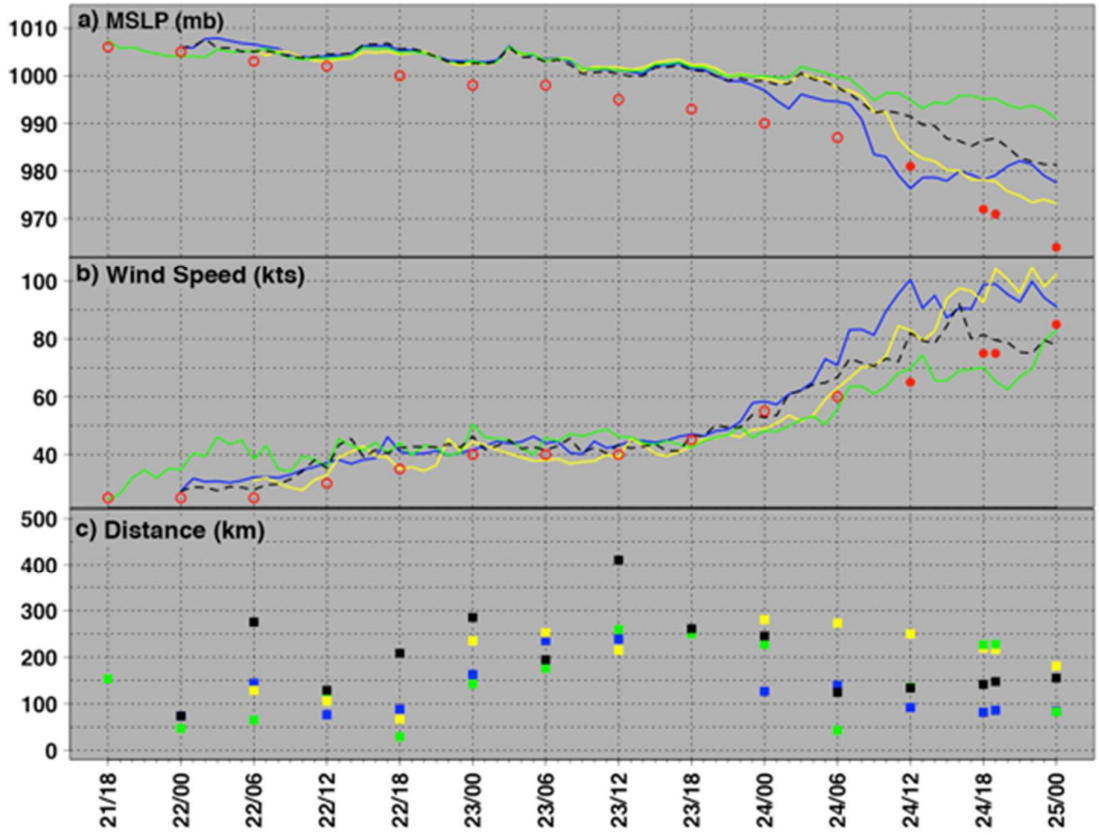

Figure 3. Mean sea-level pressure (MSLP, mb) and maximum tangential wind speed (kts) for the control (blue line), no-terrain (black dashed line), control initialization minus six hours (green line), and control initialization plus six hours (yellow line) simulations top and middle panels, respectively, against Best Track (red circles, open=depression/storm status and filled=hurricane status). Track error distance (km, corresponding colored squares) is shown in the bottom panel.

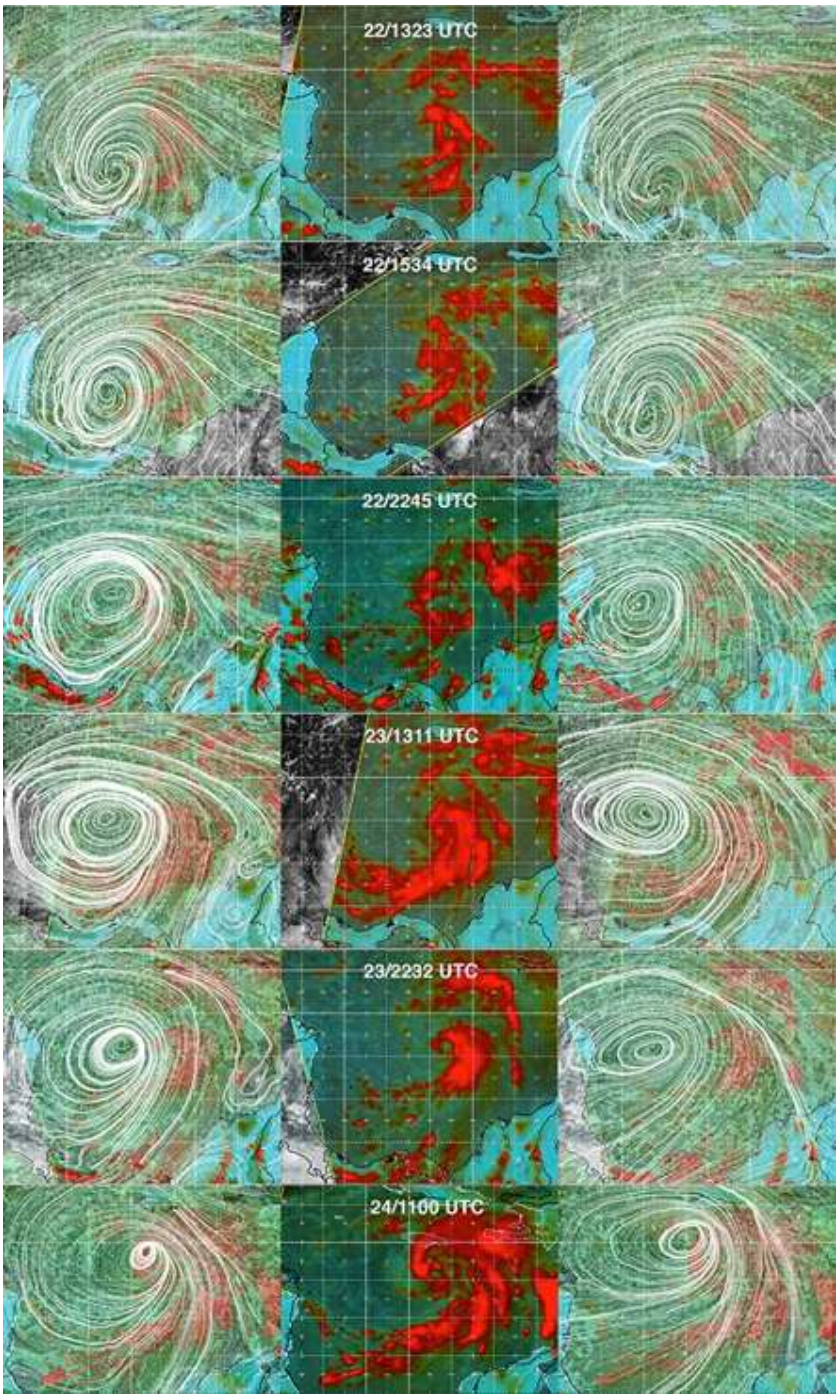

Figure 4. Composite brightness satellite imagery of Hurricane Sandy (2012) courtesy of the Naval Research Laboratory for six time periods over 22-24 October (center panel). Left and right panels re-illustrate the center panel with coincident 925 hPa streamlines overlain for the control and no-terrain simulation, respectively.

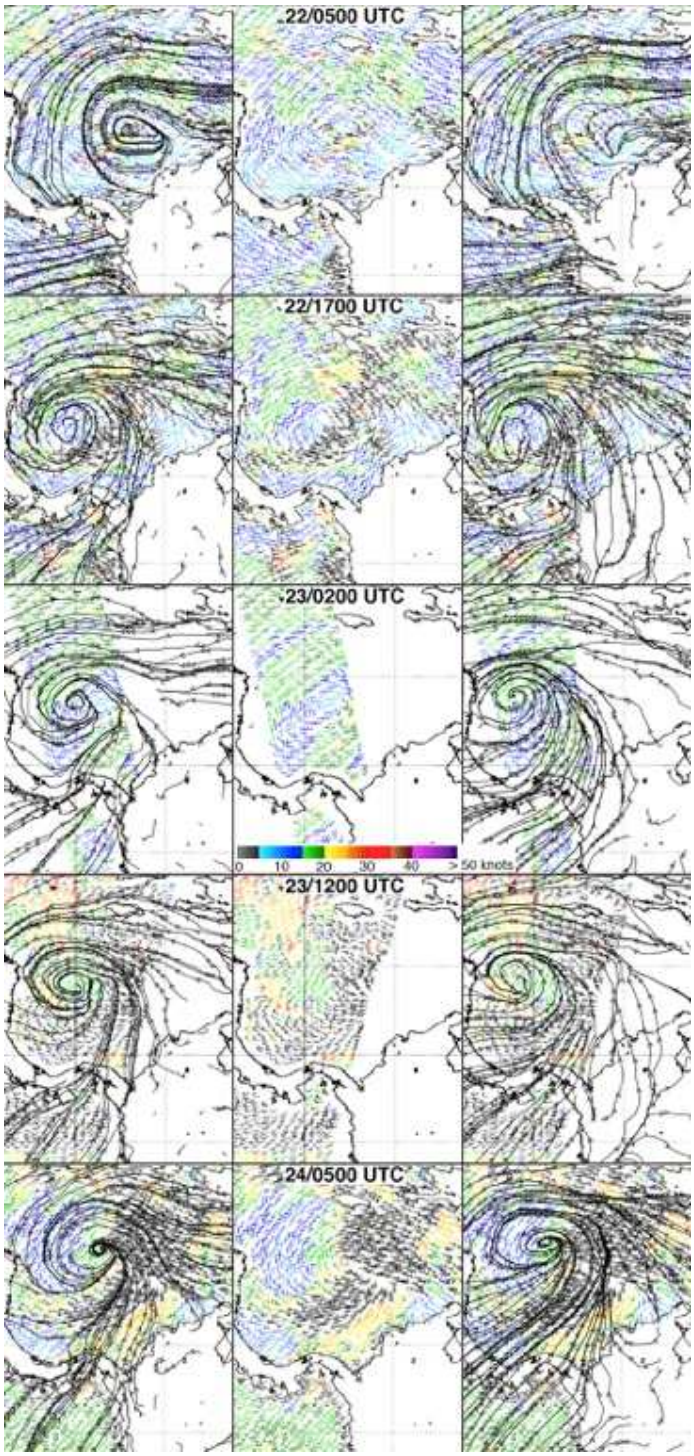

Figure 5. Same as Fig. 4, except scatterometer retrievals of the surface wind field courtesy of NESDIS underlie model streamlines for five snapshots.

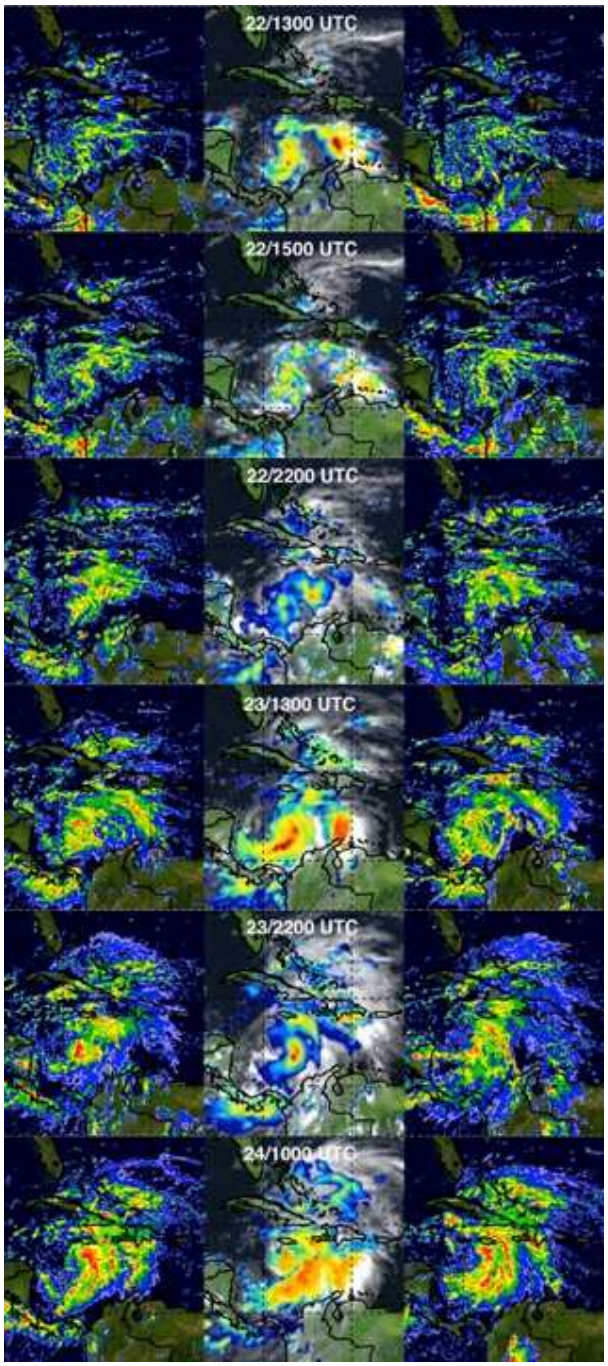

Figure 6. TRMM hourly rainfall accumulation courtesy of JAXA Global Rainfall Watch System for six time periods over 22-24 October (center panel). Left and right panels illustrate model-derived maximum reflectivity for the control and no-terrain simulation, respectively.

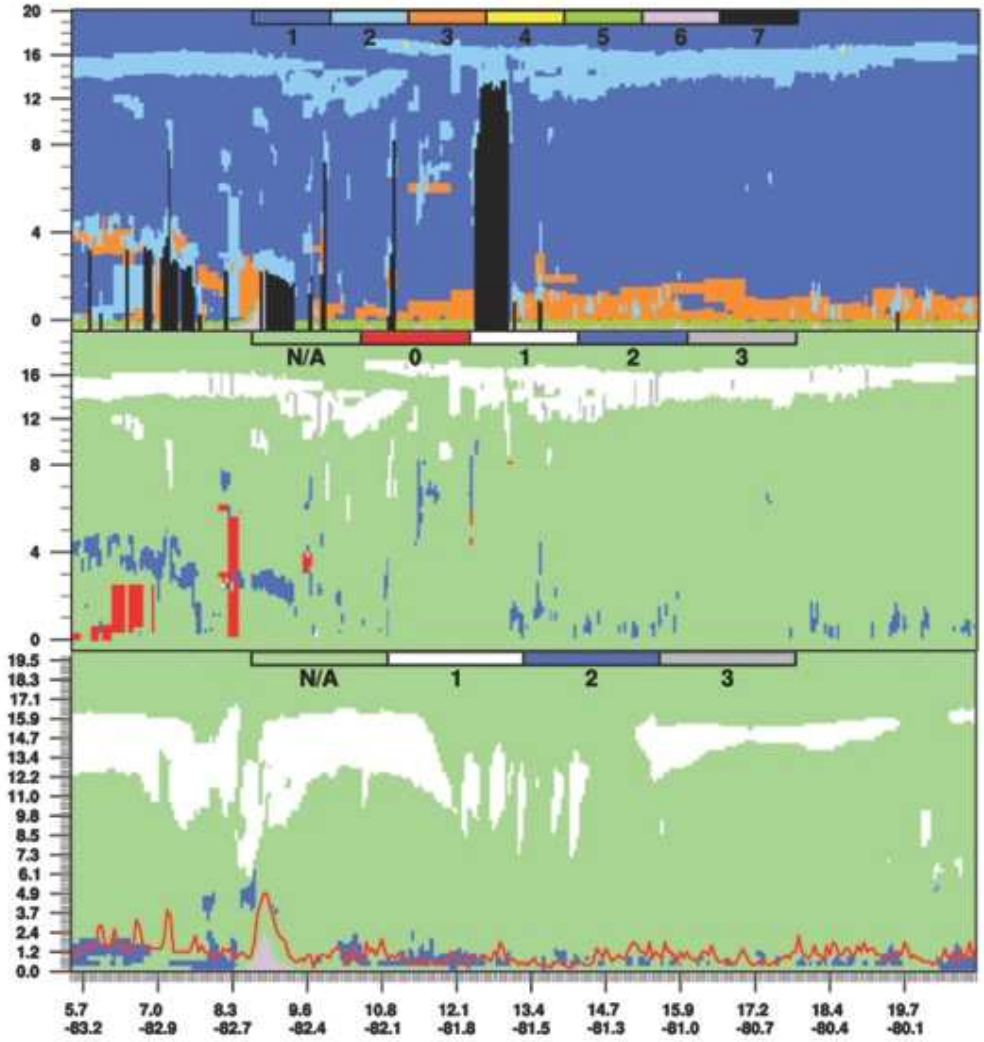

Figure 7a. Horizontal distance (x-axis, degrees) – height (y-axis, km) cross sections from CALIPSO lidar and WRF for 22 October 2012 07 UTC. Top panel illustrates CALIPSO Vertical Feature Mask where signal values of 1=clear air; 2=cloud; 3=aerosol; 4=stratospheric layer; 5=surface; 6=subsurface; and 7=totally attenuated. Middle panel illustrates CALIPSO liquid/ice phase where green=Not Available or background; red or 0=unknown; white or 1=ice phase; and 2=liquid water phase; and grey or 3=horizontal ice. Bottom panel illustrates the liquid/ice phase from the WRF control run (colors align with middle panel definitions). The red horizontal line indicates planetary boundary layer height (km) derived from turbulent kinetic energy.

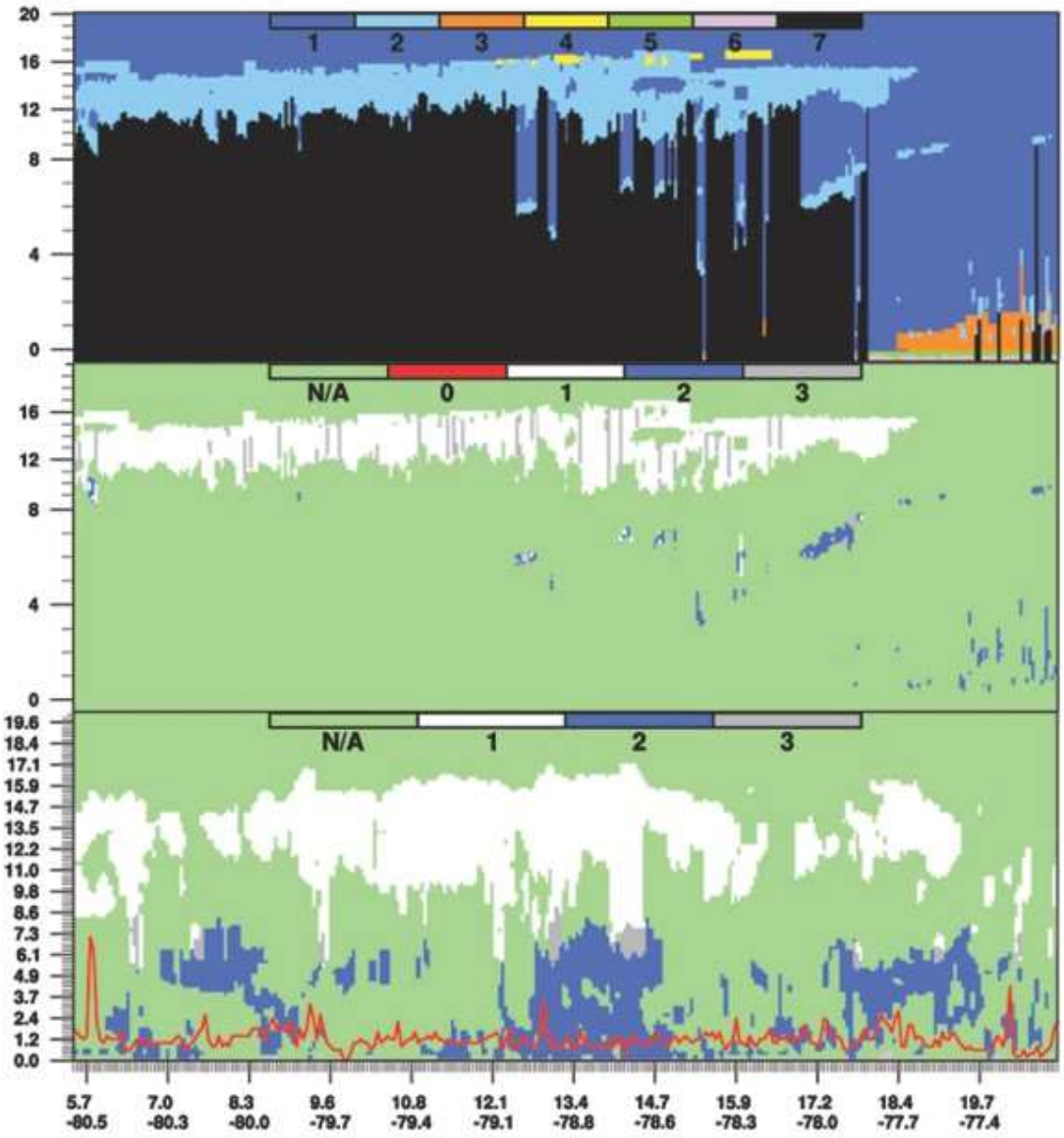

Figure 7b. Same as Fig. 7a except for 23 October 2012 18UTC.

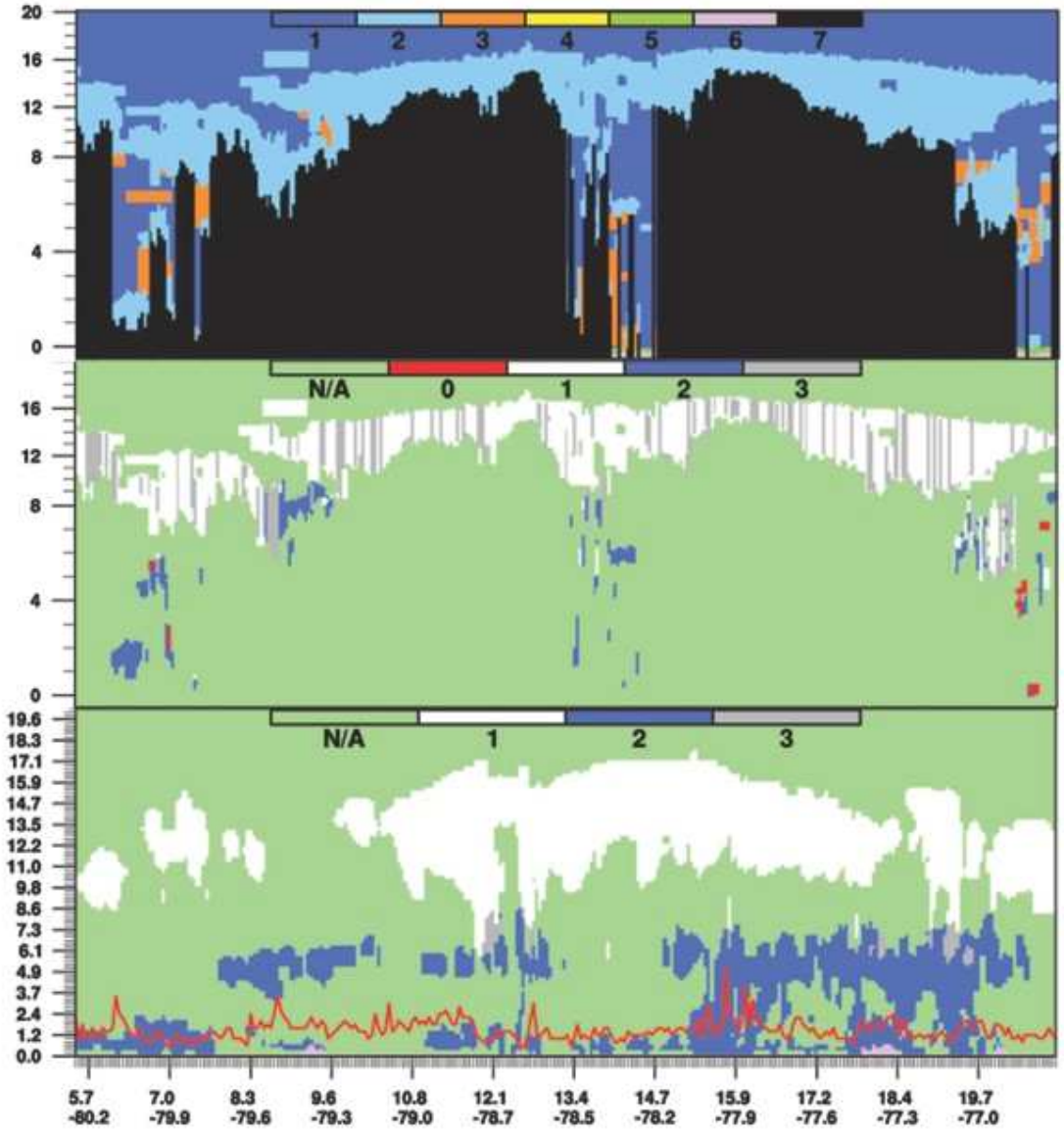

Figure 7c. Same as Fig. 7a except for 24 October 07 UTC.

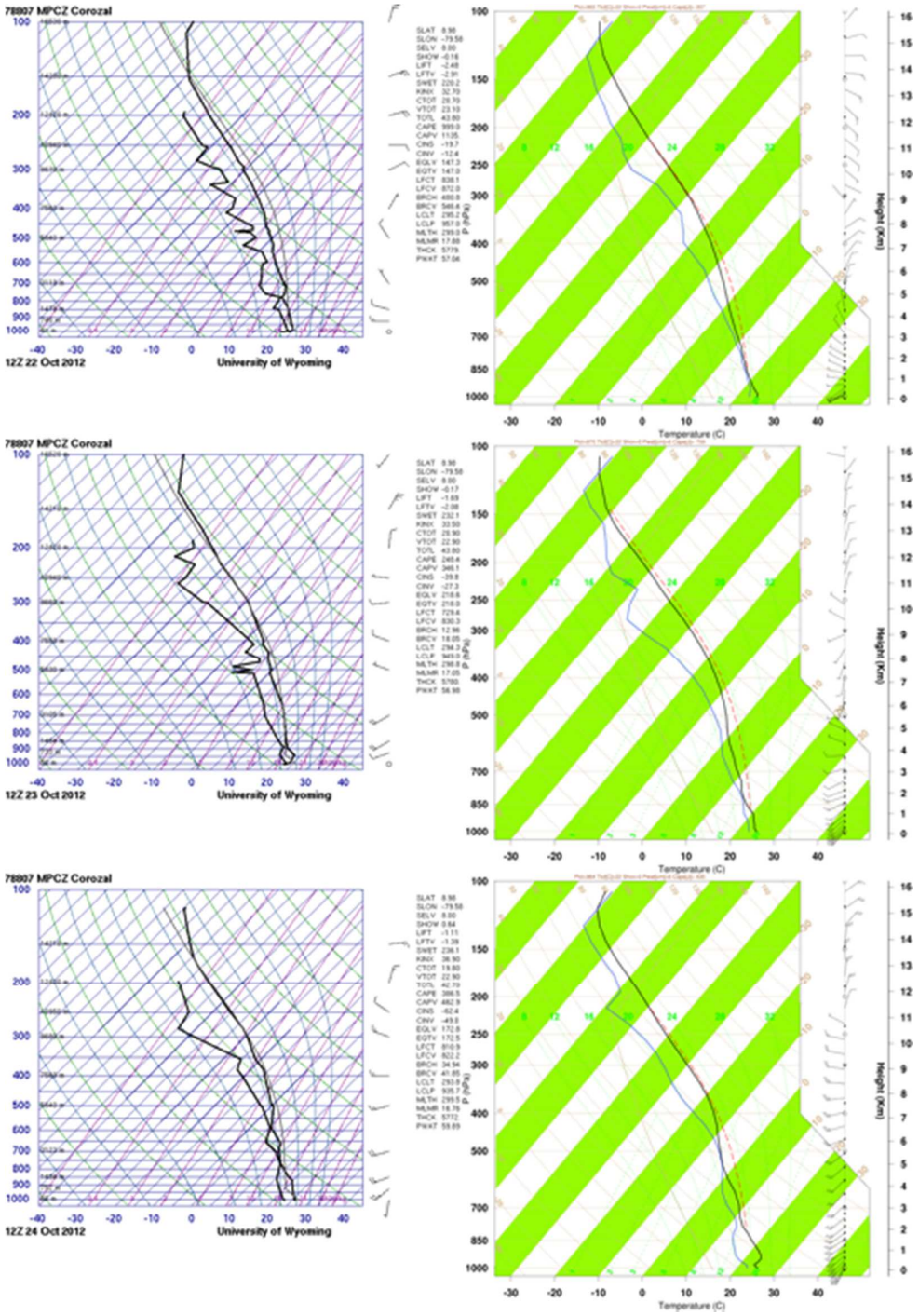

Figure 8. Observed versus (model-derived) soundings from the control run for three 12 UTC time periods for 22-24 October top to bottom and left to (right), respectively.

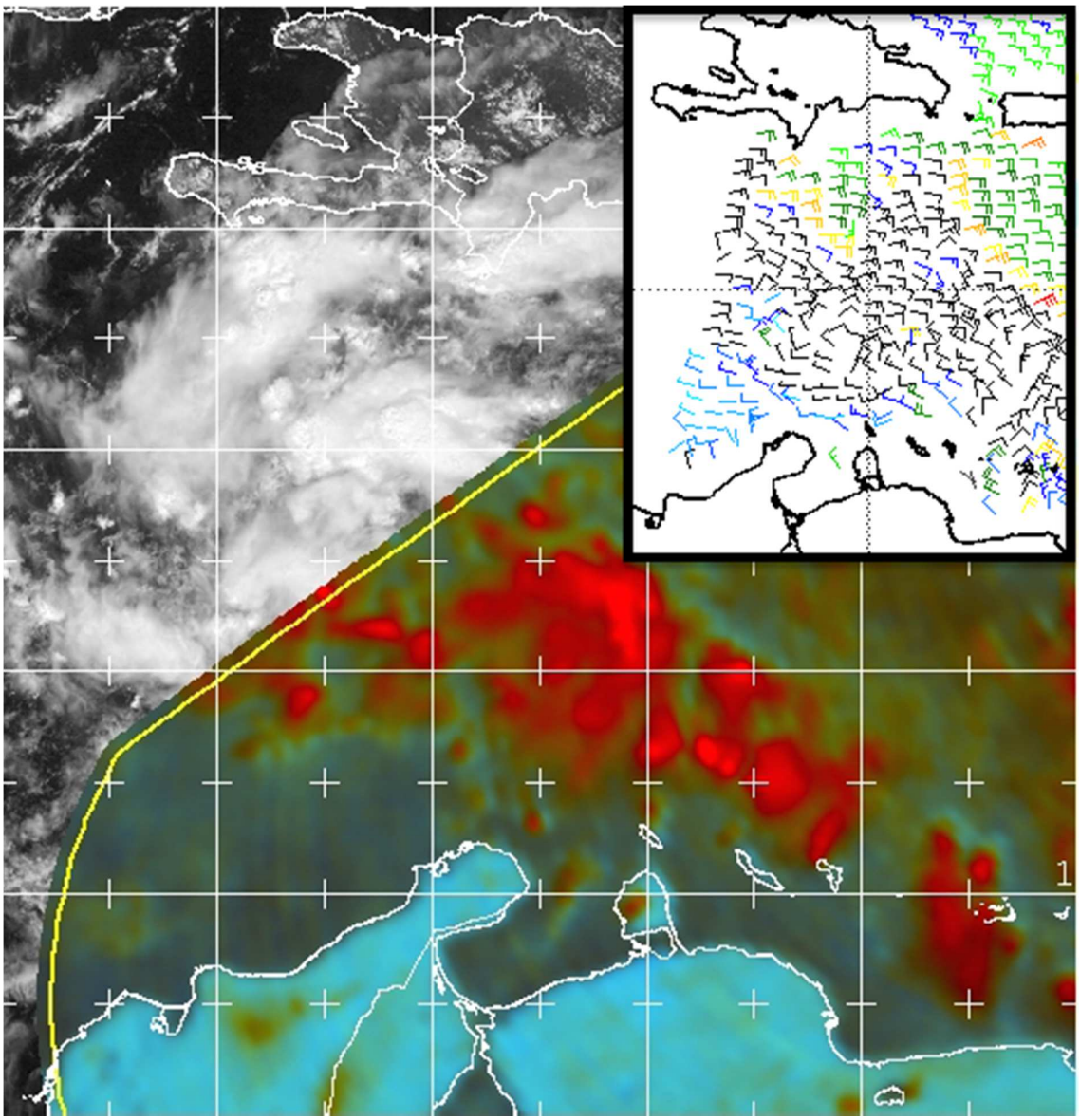

Figure 9. Depiction of the pre-Sandy disturbance short after crossing the Lesser Antilles from composite brightness imagery (base panel, as shown in Fig. 4) for 20 October 2012 at 1548 UTC with near-coincident scatterometer surface wind (kts; inset panel as shown in Fig. 5) for 20 October 2012 at 1048 UTC.

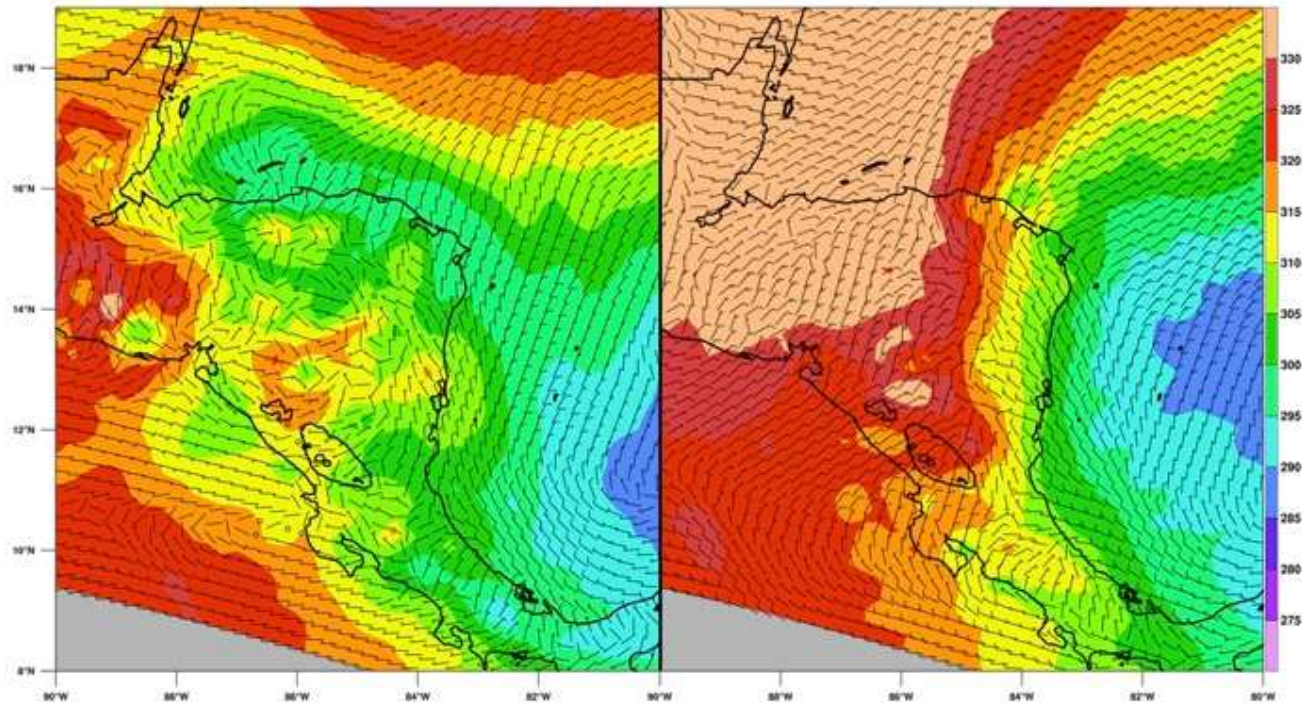

Figure 10. Depiction of the 975 hPa geopotential heights (shaded) and winds (barbs, kts) from NARR for 21 October at 18 UTC and 22 October at 06 UTC left and right, respectively. The southward progression of the transient higher heights and the associated offshore flow along the eastern mountain slopes of Honduras, Nicaragua, and Costa Rica represent the primary features of discussion.

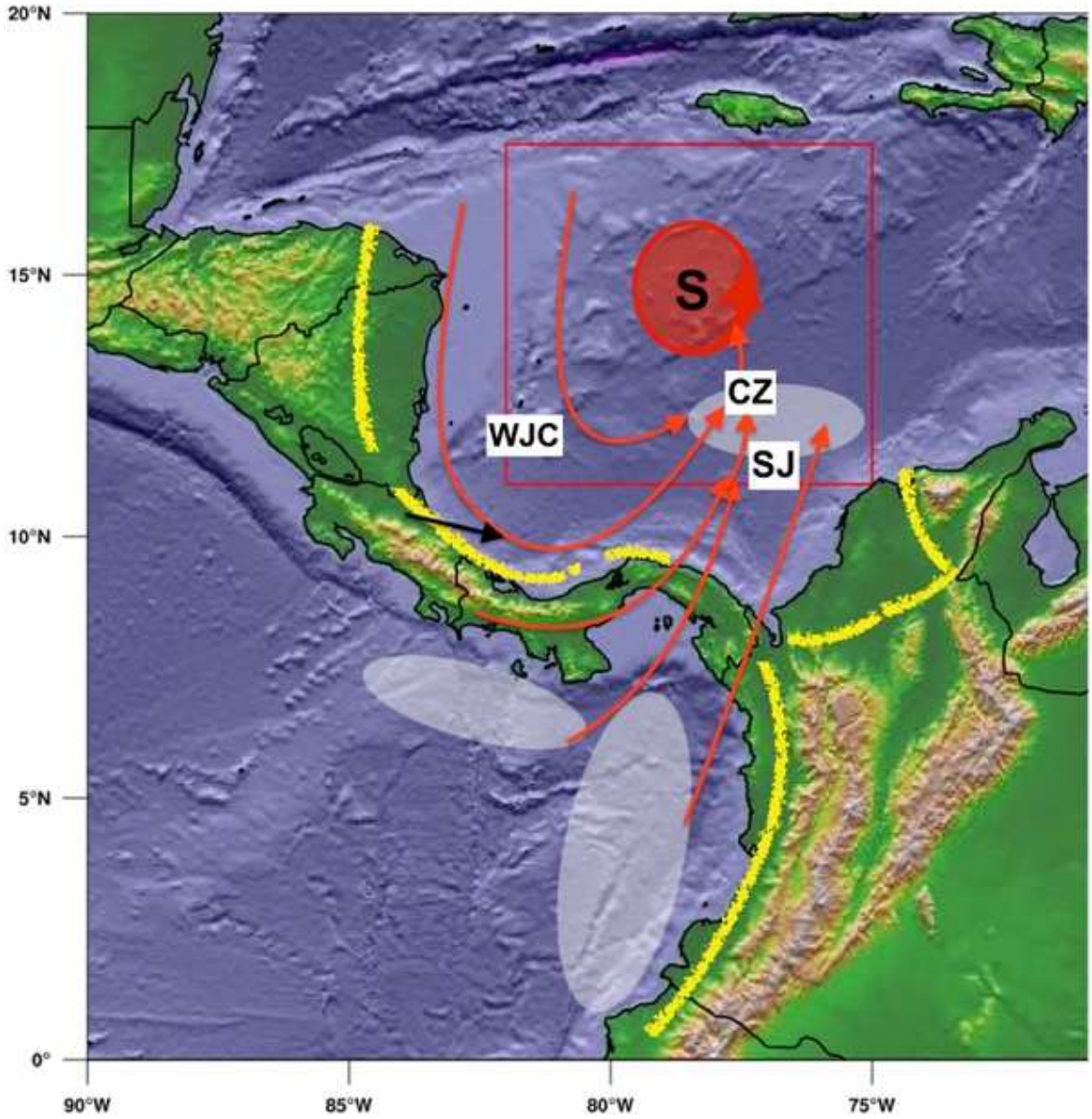

Figure 11. Caricature depiction of the westerly jet channel (WJC) that ensued between the topography/landmass and the disturbance, the southerly mesoscale jets (SJ), and their convergence zone (CZ) on the southeast side of the vortex (S=Sandy, red cyclonic circulation). White translucent ovals indicate broad areas of clustered convection. The yellow rough-edged lines demark the alongshore ridging that developed adjacent to the topographic barriers and emanated toward the sea.

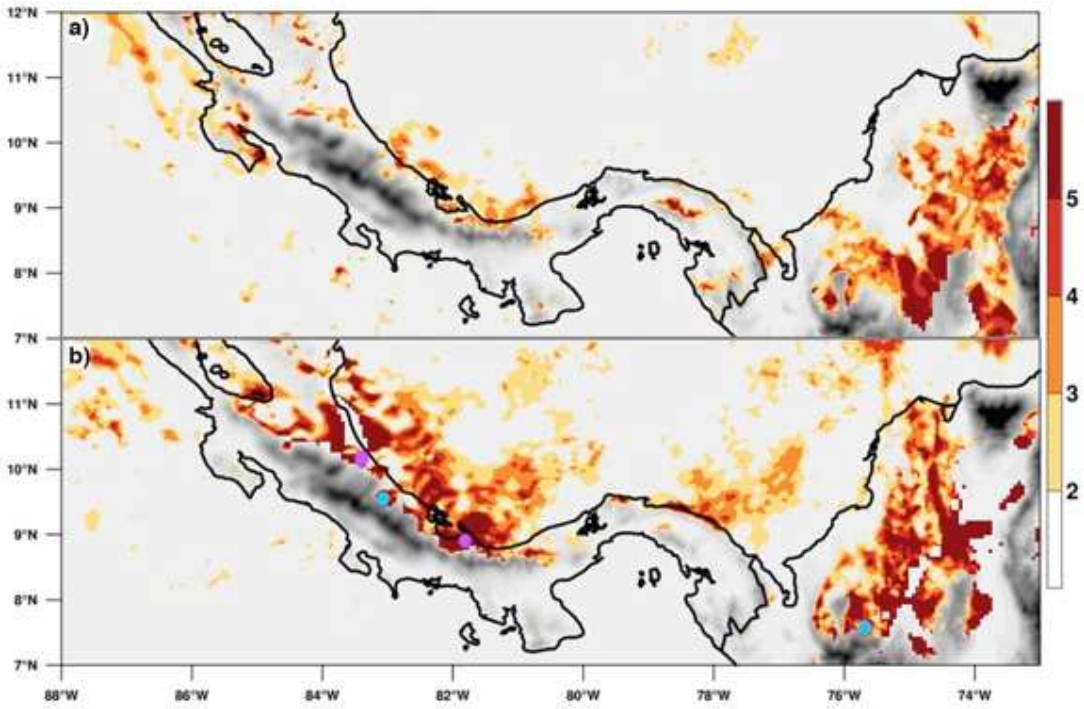

Figure 12. Temperature difference (C) from the control minus no-terrain simulation on the 304K potential temperature surface for positive values only (control > no-terrain) for 22 and 23 October 2012 at 22 UTC, top and bottom, respectively. Solid purple and light blue dots in the bottom panel indicate the four sounding locations depicted in Fig. 13.

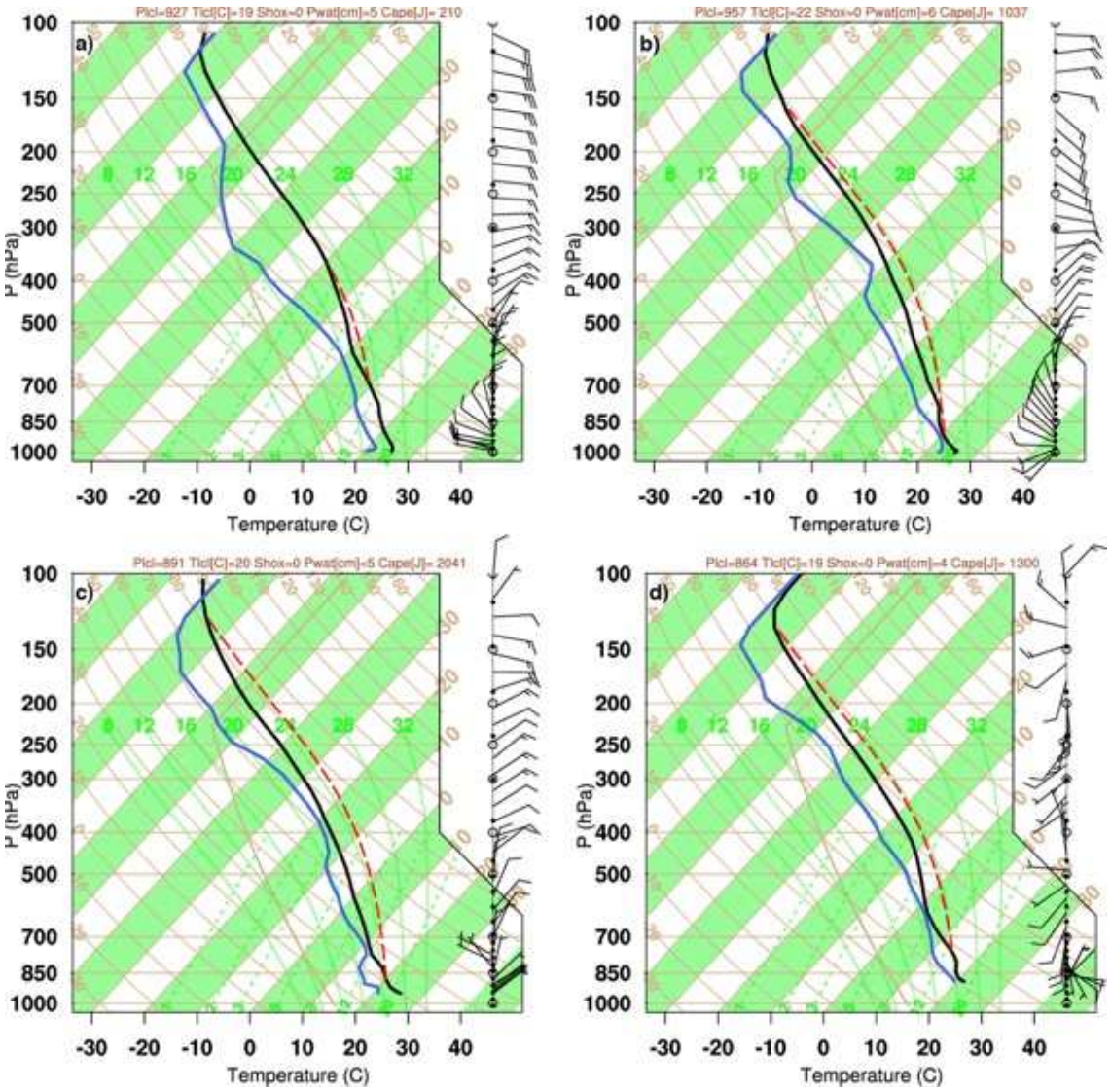

Figure 13. Sounding profiles illustrating the vertical structure of the nocturnal inversion for 22 October 2012 at 09 UTC (top panels, a and b) and the MPS circulation for 22 October at 16 and 14 UTC (bottom panels, c and d, respectively). Profile locations are indicated as solid purple and light blue dots, respectively in Fig. 12 (bottom panel).

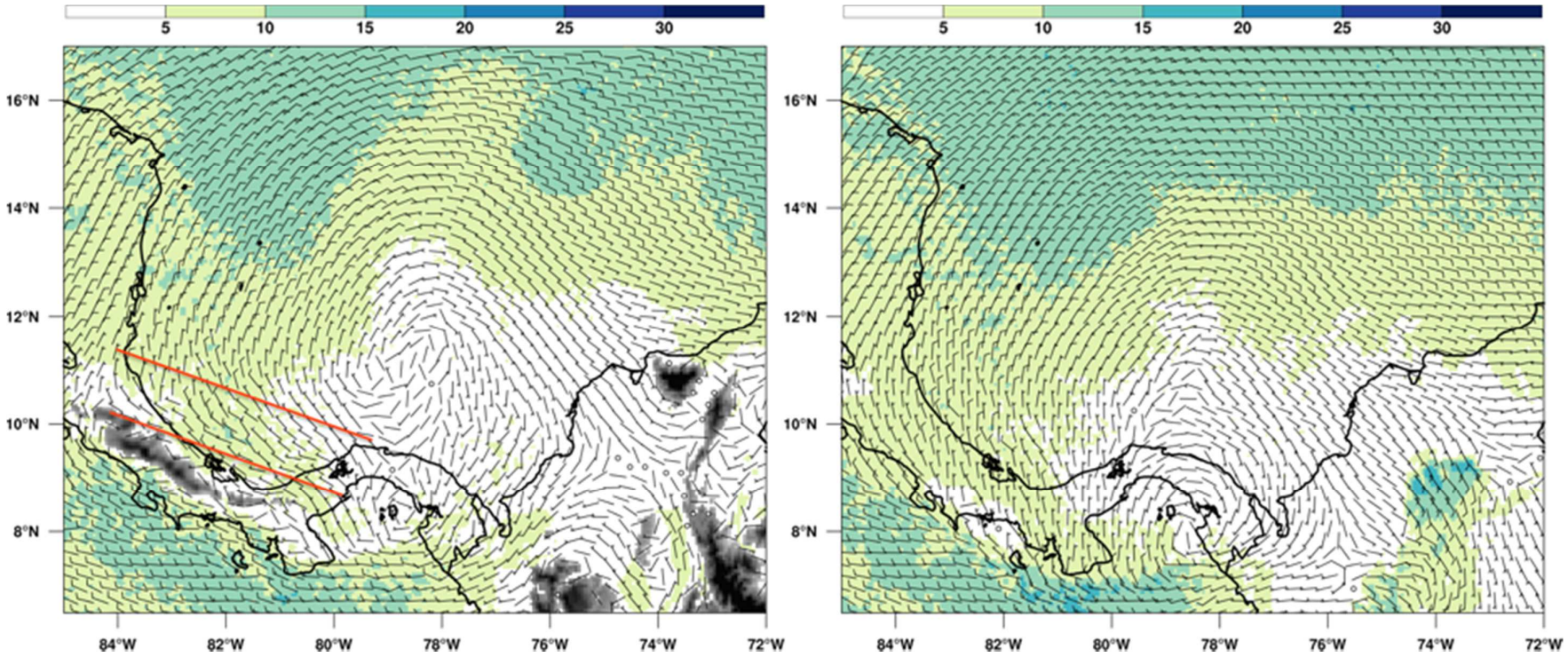

Figure 14. Illustration of the horizontal wind field (kts, barbs, shaded speed) on the 302 K potential temperature surface for the control and no-terrain simulation, left and right panels, respectively for 22 October at 08 UTC. The westerly nocturnal jet feature in the control run is prominent within the two overlain red lines, left panel.

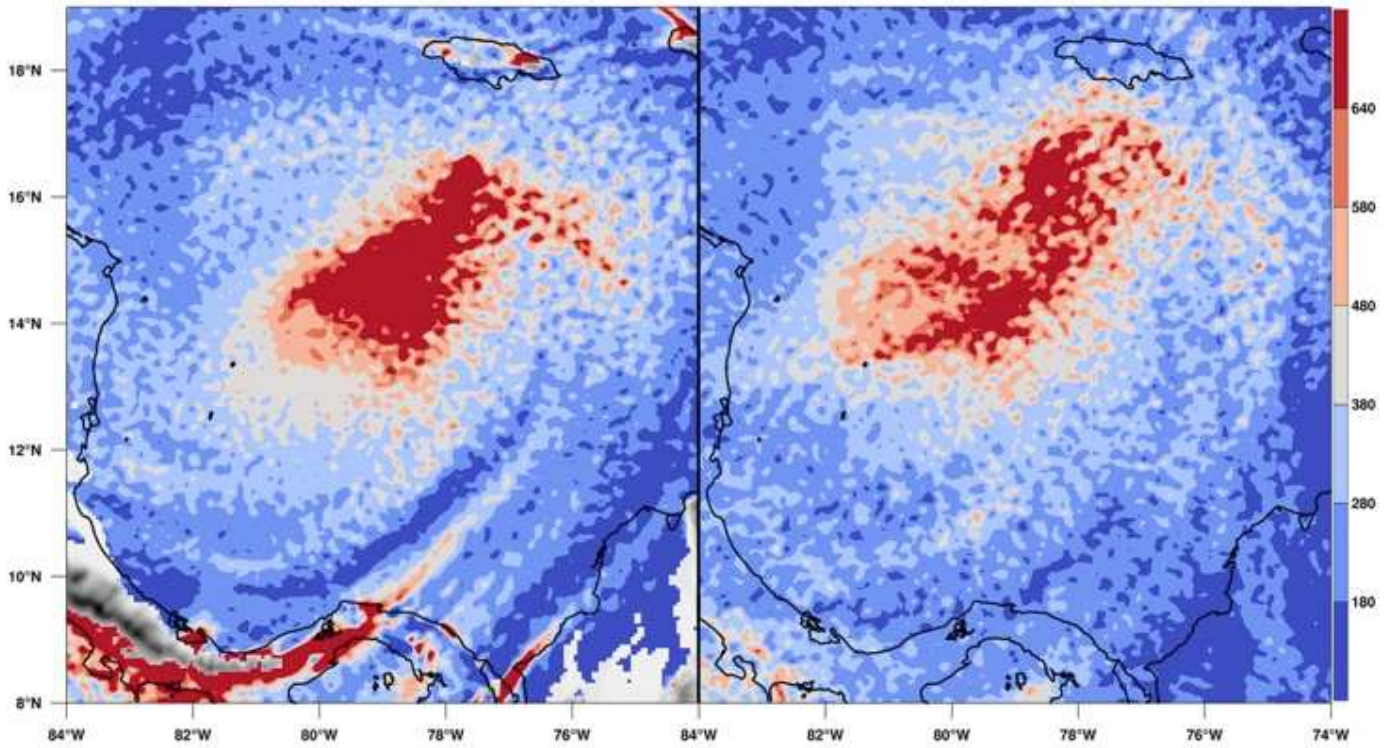

Figure 15. Time integral of positive relative vorticity (x 10^{-5} s^{-1}, 22/00 UTC through 24/12 UTC) on the 304 K potential temperature surface for the control and no-terrain simulation, left and right panels, respectively.

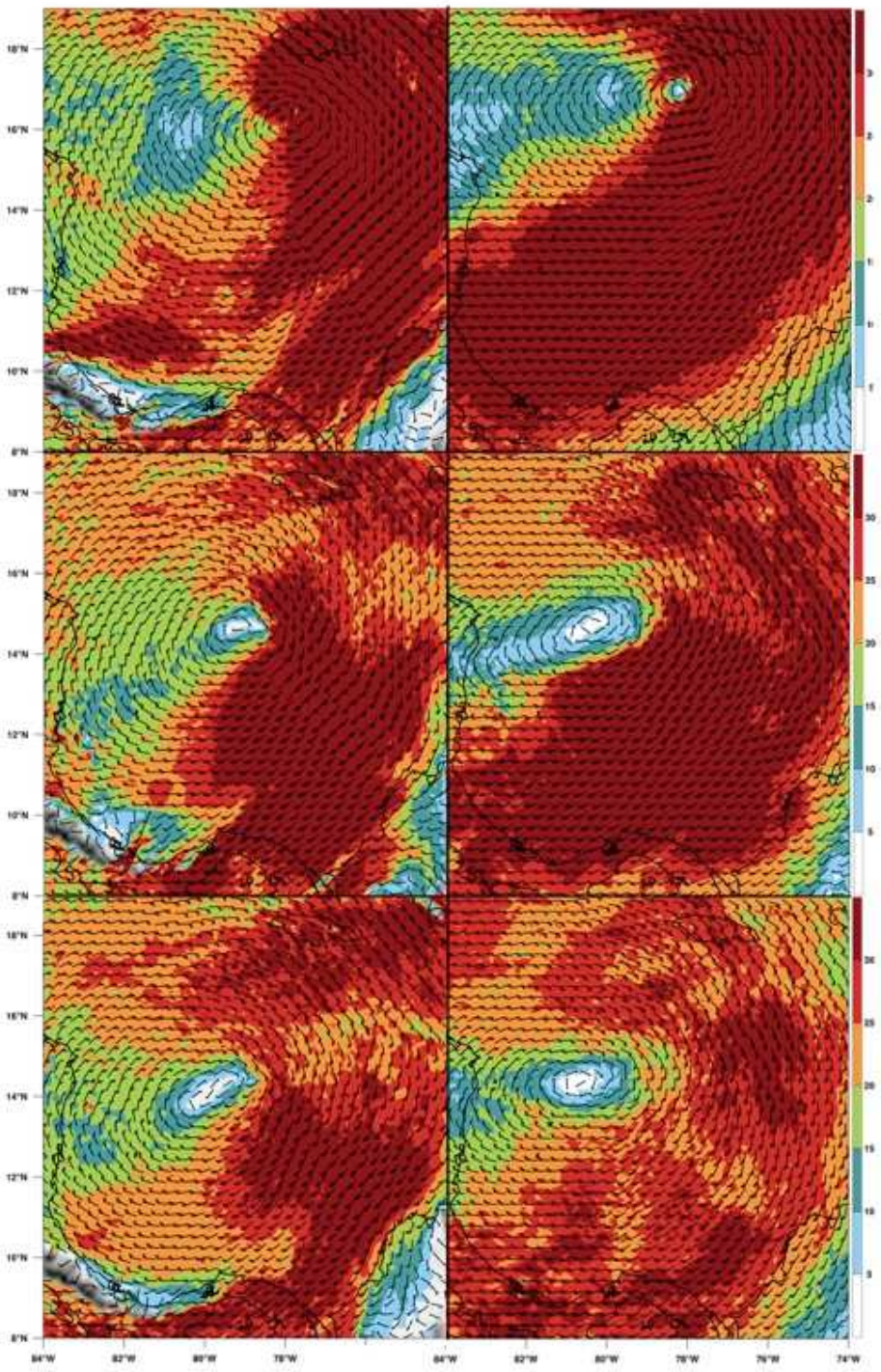

Figure 16. Depiction of shaded wind speed with barbs (black; kts) on the 304 K potential temperature surface for 24/12, 24/00, and 23/18 UTC October 2012 for the control and (no-terrain) simulations, top to bottom and left (right) panels, respectively.

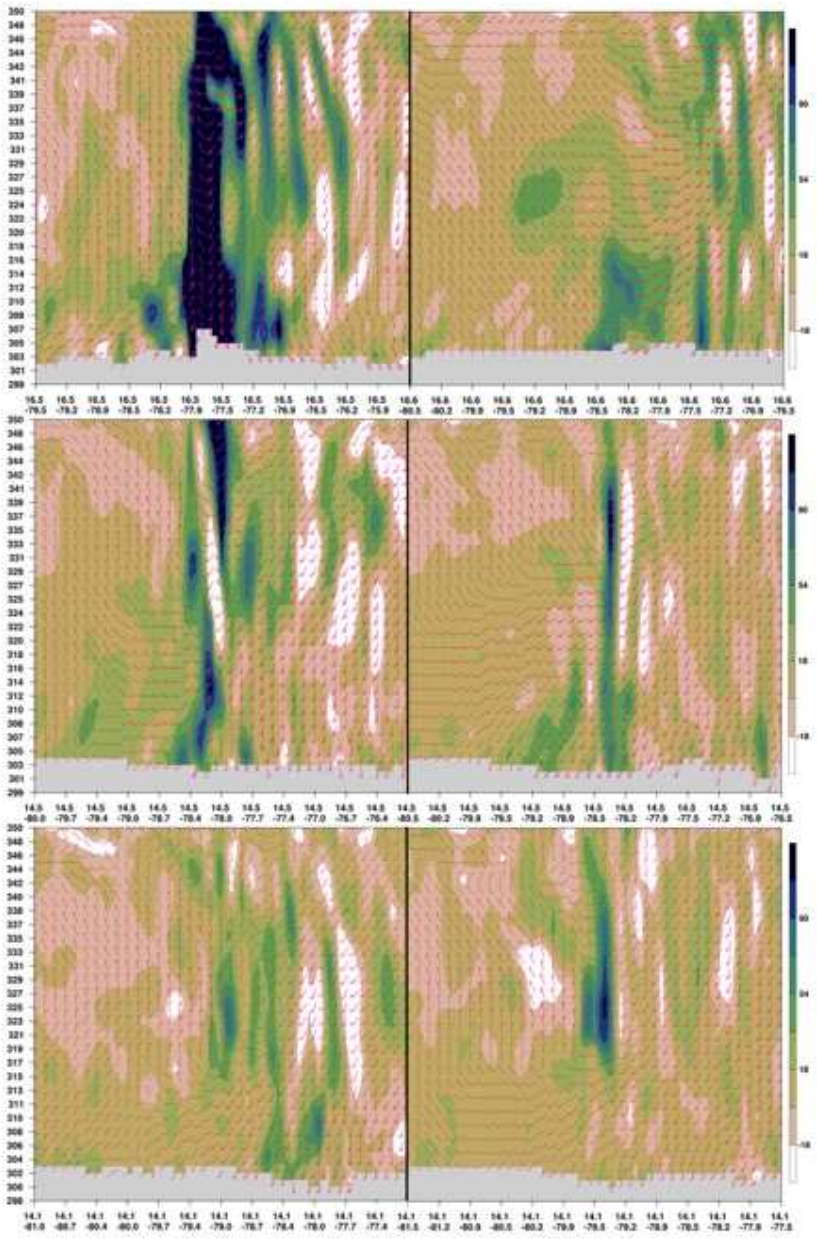

Figure 17. Depiction of shaded relative vorticity (x 10^{-5} s^{-1}) and wind barbs (pink, kts) cross sections (west-to-east) across and centered on the vortex core for 24/12, 24/00, and 23/18 UTC October 2012 for the control and (no-terrain) simulations, top to bottom and left (right) panels, respectively. The vertical units are potential temperature (K) and degrees represents horizontal distance. Gray shading indicates the intersection of potential temperature with the ocean surface.

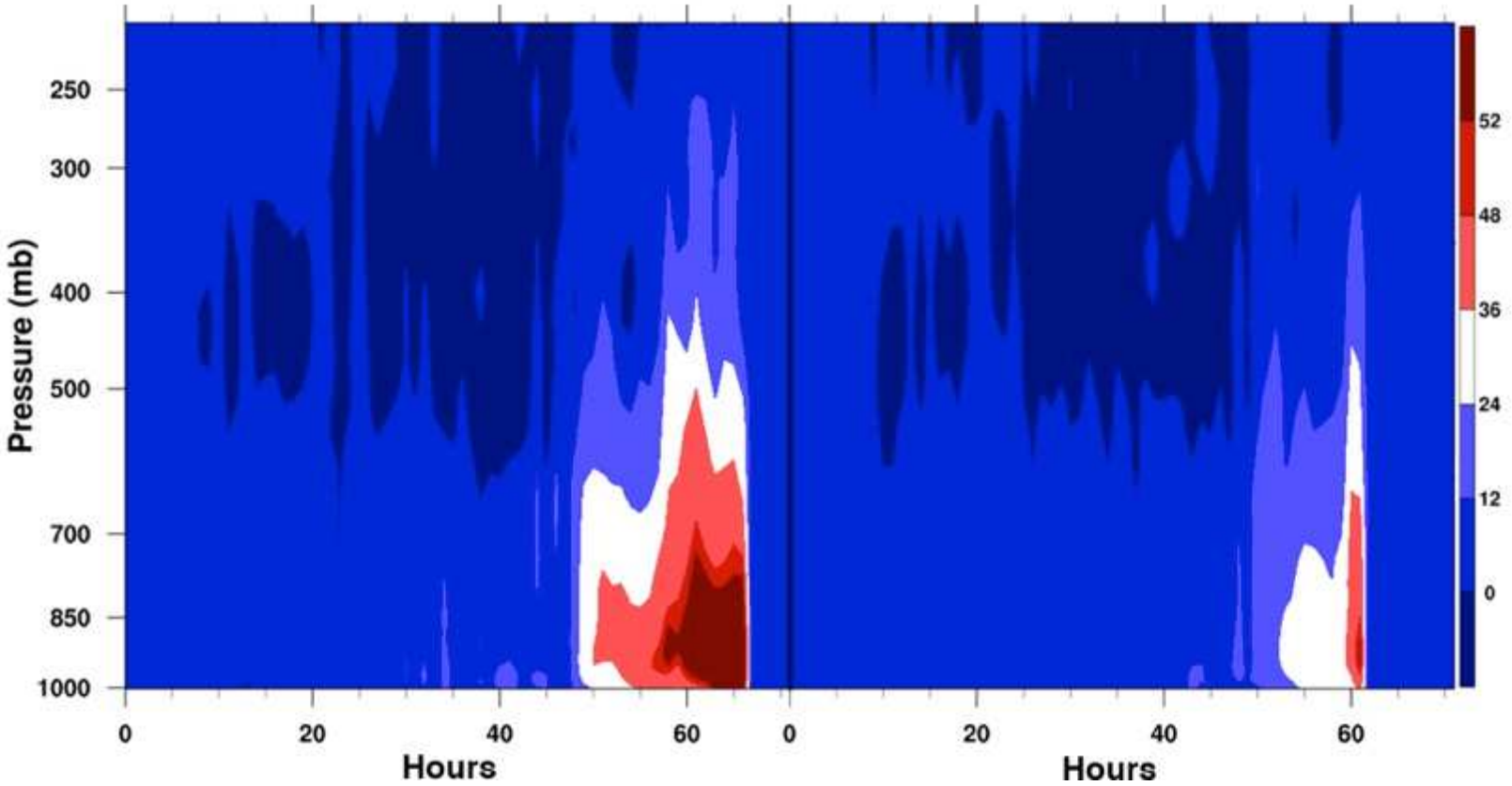

Figure 18. Vertical profile of core average relative vorticty minus the environment by hour over the control and no-terrain simulations, left and right, respectively.

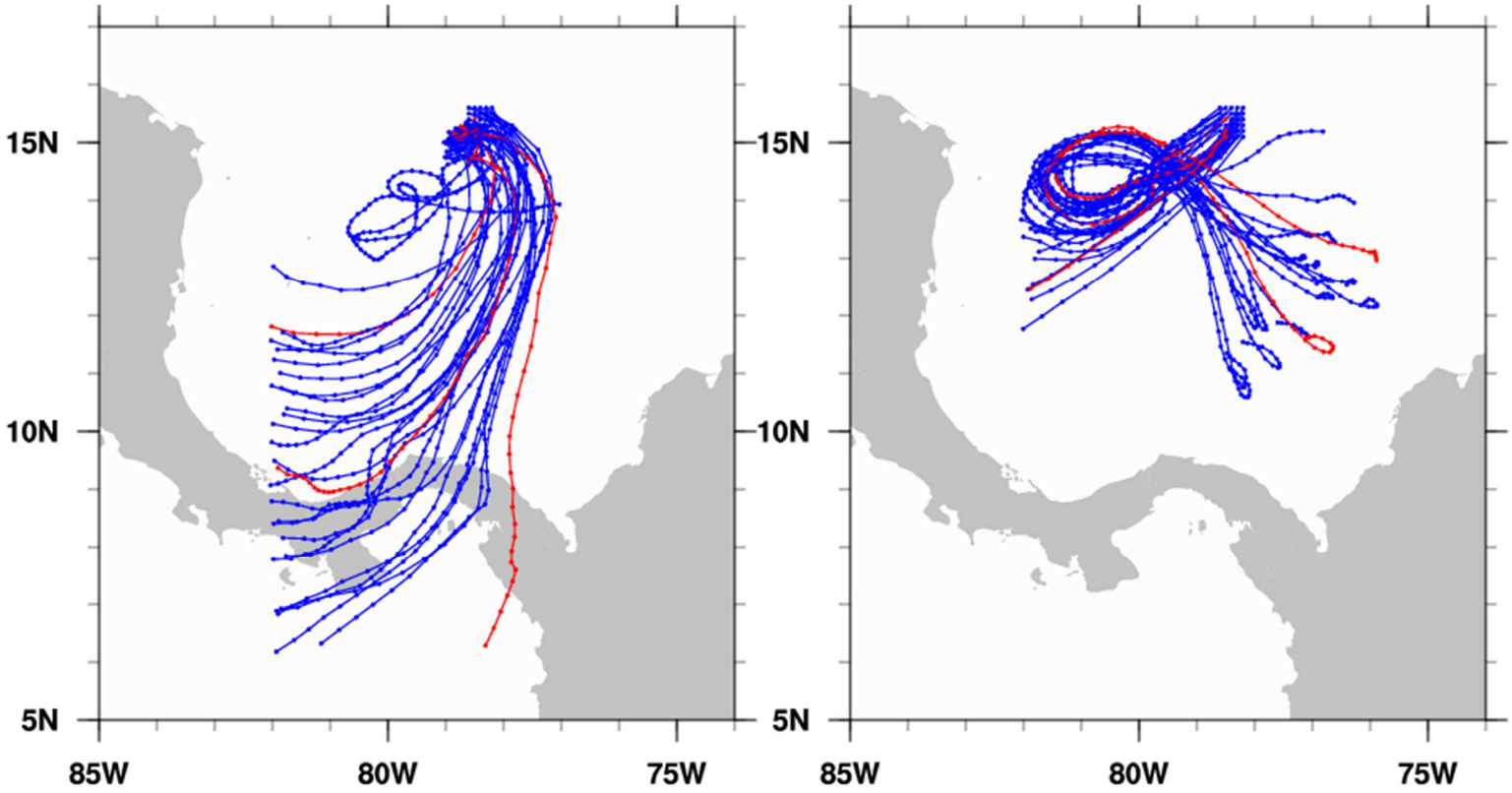

Figure 19. Illustration of the horizontal pathways taken by air parcel trajectories initiated from the vortex core for the control and no-terrain simulations, left and right map, respectively. Trajectories were initiated from 925 hPa from 24/06 UTC October back 54 hours to model initialization at 22/00 UTC October. Red lines indicate trajectories (depicted from northwest to southeast, left panel) in correspondence with westerly and southerly jets. The coincident no-terrain trajectories are also in red (right panel). Blue lines represent other attempts.

Summary and concluding remarks

This dissertation study examined the dynamics within the planetary boundary layer for tropical and extratropical environments as part of three research papers. Paper one evaluated the advantages and disadvantages boundary layer height methods for potential use in operational prediction over the continental United States. Paper two and three examined the precursor environment at the large scale and mesoscale, respectively, associated with Hurricane Sandy (2012). The major findings from each paper are summarized sequentially.

Paper one:

- Four methods examined: Holzworth, Stull, Richardson number, and the dissipation of TKE
- The dissipation of TKE was found to be the most robust PBL height method
- TKE disadvantage: requires a fine-resolution numerical model

Paper two:

- Examination period was October 1-22, 2012
- Formation and trajectory of incipient pre-Sandy wave was studied from east of South America westward across the Lesser Antilles
- Relevant patterns associated with changes in geopotential height were evaluated, including those for zonal height blocking, wind, north-south mass flux, vertical wind shear, and positive relative vorticity
- The daily temporal behavior of atmospheric modes such as the AOI, NAOI, and MJO

were studied at coincident periods and revealed corroborating evidence for the height patterns observed

- The behavior/contributions of the atmospheric modes and other influential measures as they occurred prior to and during the pre-Sandy disturbance are listed in Table 1 (paper two) and may be useful for forecasters evaluating the precursor hurricane environment
- Results show that meridional exchange (high/mid-latitude and subtropical/tropical interaction) occurs as way to restore imbalance in either zone. Reasons for the persistent equator-to-pole exchange initiation were evaluated against: 1) Cooling over continental high latitudes while persistent warming remains over the subtropics/tropics; 2) Persistent or above normal tropical convection and or storm activity; 3) Downward sinking from a sudden stratospheric warming event over the Arctic as an initiator of Arctic imbalance and a precursor of meridional exchange in the troposphere; 4) Sea surface temperature anomalies
- Results raise a fundamental question: *is it characteristic of late season tropical development to be a response to a period of higher-latitude excitation?* Or expressed in another manner: *can vigorous meridional exchange over an extended period produce a wake zone of minimal kinetic energy wherein residual mesoscale perturbations (and those generated locally) can organize, develop, and re-propagate back upscale*?

Paper three:

- Examination period was October 22-25, 2012
- The precursor mesoscale environment and the potential role of the terrain (and the associated dynamics) on vortex development and intensification were examined for Hurricane Sandy (2012)
- Two numerical simulations were performed, a control run and no-terrain experiment
- Several mesoscale features were detected in the mass field of the control simulation and examined across the southwestern Caribbean Sea including 1) transient low-level mass perturbations that propagated southward in response to an upstream mid-latitude jetlet; 2) a nocturnal jet along the Costa Rica mountains/shoreline; 3) the mountain-plains solenoid circulation along the northeastern mountain slopes of Costa Rica, Panama and Colombia; and 4) broad areas of convection south of Panama/Costa Rica and west of Colombia. Each feature in connection with the nearby complex terrain was shown to be influential in initiating flow curvature and vorticity
- Two distinct, curved jet features were also identified in the precursor environment; a westerly and southerly surge. Both jets were critical vorticity generators in association with the landmass/terrain and converged just south of the vortex inflow region (southeast side of the storm)
- The role of the Caribbean terrain in association with the aforementioned mesoscale features was shown to be instrumental on the vortex development. Comparisons of a no-terrain numerical simulation against the control run revealed distinct developmental differences in vortex geometry, size, and tilt over the spin-up time period

- Given the influential nature of the terrain on the Hurricane Sandy's development, as shown in this study, one has to wonder how this result translates to other tropical cyclones. Is some degree of continental proximity a requirement (or at least a key ingredient) for tropical cyclone development in combination with other well documented environmental factors (e.g., low vertical wind shear; a warm sea surface, a deep moist column etc..)? The primary role of the continent in this case appears to rest on the surrounding mass field organization, specifically the curvature of it, and the resultant production of environmental vorticity. This question may be important toward addressing why some tropical cyclones develop and others do not despite the presence of similar environmental conditions. Examination of several other storm scenarios is necessary to fully evaluate these questions, although if some degree of continental proximity proves to be a consistent influential factor, the implications may prove to be invaluable for hurricane prediction